

5-1-2019

Using internal state variables to model shear influenced plasticity and damage effects of high velocity impact of ductile materials

Luke Andrew Peterson

Follow this and additional works at: <https://scholarsjunction.msstate.edu/td>

Recommended Citation

Peterson, Luke Andrew, "Using internal state variables to model shear influenced plasticity and damage effects of high velocity impact of ductile materials" (2019). *Theses and Dissertations*. 4894.
<https://scholarsjunction.msstate.edu/td/4894>

This Dissertation - Open Access is brought to you for free and open access by the Theses and Dissertations at Scholars Junction. It has been accepted for inclusion in Theses and Dissertations by an authorized administrator of Scholars Junction. For more information, please contact scholcomm@msstate.libanswers.com.

Using internal state variables to model shear influenced plasticity and damage effects of
high velocity impact of ductile materials

By

Luke Andrew Peterson

A Dissertation
Submitted to the Faculty of
Mississippi State University
In Partial Fulfillment of the Requirements
For the Degree of Doctor of Philosophy
in Aerospace Engineering
in the Bagley College of Engineering

Mississippi State, Mississippi

May 2019

Copyright by
Luke Andrew Peterson
2019

Using internal state variables to model shear influenced plasticity and damage effects of
high velocity impact of ductile materials

By

Luke Andrew Peterson

Approved:

Manav Bhatia
(Major Professor)

Thomas E. Lacy
(Co-Research Director)

Mark F. Horstemeyer
(Co-Research Director)

Robert D. Moser
(Committee Member)

James C. Newman, Jr
(Committee Member)

Haitham El Kadiri
(Committee Member)

Matthew W. Priddy
(Committee Member)

David S. Thompson
(Graduate Coordinator)

Jason M. Keith
Dean
Bagley College of Engineering

Name: Luke Andrew Peterson

Date of Degree: May 3, 2019

Institution: Mississippi State University

Major Field: Aerospace Engineering

Major Professor: Manav Bhatia

Title of Study: Using internal state variables to model shear influenced plasticity and damage effects of high velocity impact of ductile materials

Pages in Study: 191

Candidate for Degree of Doctor of Philosophy

A physically motivated Internal State Variable (ISV) constitutive model is extended to account for shear influenced void evolution for predicting damage behavior in ductile solids. The revised ISV model is calibrated for an aluminum 7085-T711 alloy using a series of microstructure and mechanical property quantification experiments. The calibrated ISV model for the aluminum alloy is implemented in an implicit finite-element code (Abaqus) to simulate the deformation of notch Bridgman tension specimens at a variety of stress states and temperatures. The model revisions and calibrated aluminum ISV model are validated through successful prediction of mechanical and microstructure evolution for structures subjected to a variety of complex stress state conditions.

The extended ISV model framework is used to study shear influenced plasticity and damage mechanisms resulting from ballistic impact of metals. A Rolled Homogeneous Armor (RHA) steel alloy is selected for the impact model due to wide availability of documented penetration characteristics and ballistic performance data of RHA steel.

Finite Element Analysis (FEA) simulations of ballistic impact of RHA steel projectiles against RHA steel plates are performed using a calibrated ISV constitutive model for RHA steel. An FEA simulation based parametric study is performed to assess the effect of a variety of microstructure and mechanical properties on the ballistic performance of RHA steel targets. FEA simulations are used to predict a transition in ballistic perforation mechanisms for high hardness steel alloys by accounting for variations in microstructure properties qualitatively documented in the literature.

DEDICATION

This work is dedicated to the memory of my father, Harold “Pete” Peterson, whom I dearly miss. I think of our conversations often and am grateful for his example of patience and compassion.

I would also like to dedicate this work to my wife and love, Sarah. You bring joy to life and make me aspire to be a better person than I ever thought I could be. Your presence is reassurance in times of doubt and your love sustains me. I love you, now and always.

Finally, I wish to dedicate this to my mother, Maria Peterson. Thank you for your love and, with Dad, support of my curiosities and interests. Thank you for teaching me the value of learning and for being a living example of inner strength and love for family.

ACKNOWLEDGEMENTS

I wish to express my deepest gratitude to my dissertation research directors Dr. Thomas Lacy and Dr. Mark Horstemeyer for guiding this work and their contributions to my academic, professional, and personal growth during my time at Mississippi State University. I sincerely appreciate their patience, passion for working with students, and eagerness to advocate on our behalf. I am forever grateful for the tremendous opportunities their teaching, commitment, and tireless dedication have afforded me.

I wish to thank the members of my dissertation committee, Dr. Manav Bhatia, Dr. Robert Moser, Dr. Haithem El Kadiri, Dr. James Newman, and Dr. Matthew Priddy for their guidance, support, and insights. Our shared discussions, collaborations, and classes have stoked my interest in material science and computational solid mechanics and have made this research possible. I also wish to thank the Engineer Research and Development Center (ERDC), Center for Advanced Vehicular Systems (CAVS), the Mississippi State Aerospace Engineering Department, and the Bagley College of Engineering for financially supporting this work.

I want to personally thank Rose Mary Dill in selflessly helping myself and all the other CAVS students. Your dedication is inspiring to everyone who meets you and words cannot express how thankful I am for all that you do. I sincerely appreciate Stephen

Horstemeyer, Melissa Mott, and Robert Malley for their patience in teaching and assisting in the use of the CAVS machining and experimental equipment. I love working in the lab, even through the difficult times, and it was all made possible through your help. I wish to thank Dr. Youssef Hammi for his guidance, direction, and solution finding in finite element modeling. Our discussions have tremendously aided my growth and understanding as a modeler and helped me to overcome seemingly insurmountable challenges over the course of this work. I also want to thank Dr. Jeffrey Lloyd for our correspondence on impact modeling which led to ideas for fascinating research opportunities.

Finally, I wish to thank my fellow students for their support and friendship over the years. I especially want to thank Dr. Shane Brauer and Dr. Imran Aslam for sharing ideas and contributing to much of my early development. Thanks for showing me the ropes on so many things. The ICME class (despite its difficulty) and book chapter were some of the best times I had in school. I would also like to thank Brad Huddleston and Andrew Bowman for our numerous discussions on model theory. I learn something new every time we talk. Finally, I wish to thank all my other fellow students. I treasure our interactions and will carry the memory of our time shared here together for the rest of my life.

TABLE OF CONTENTS

DEDICATION	ii
ACKNOWLEDGEMENTS	iii
LIST OF TABLES	viii
LIST OF FIGURES	ix
CHAPTER	
I. INTRODUCTION	1
1.1 Motivation.....	1
1.2 Current State of the Literature	3
1.2.1 Impact Mechanics	3
1.2.1.1 Wave Mechanics	3
1.2.1.2 Energy Absorption	5
1.2.2 Damage Modeling History.....	6
1.2.3 Shearing	8
1.2.3.1 Shearing Experiments	8
1.2.3.2 Shearing in Plasticity and Damage Modeling.....	10
1.2.3.3 Nonlocal Methods for Constitutive Modeling of Damage	12
1.2.4 Materials of Interest	12
1.2.4.1 Rolled Homogeneous Armor Steel	12
1.2.4.2 Aluminum 7085	14
1.3 Dissertation Structure.....	15
II. AN INTERNAL STATE VARIABLE PLASTICITY DAMAGE MODEL OF AN ALUMINUM 7085-T711 ALLOY UNDER LARGE DEFORMATIONS AT VARIOUS STRAIN RATES, STRESS STATES, AND TEMPERATURES	17
2.1 Introduction.....	17
2.1.1 Aluminum 7085 Alloy	17
2.1.2 Internal State Variable Approach to Constitutive modeling.....	18
2.2 Experimental Procedure.....	25

2.2.1	Microstructure Characterization	25
2.2.2	Mechanical Testing	27
2.2.3	Fractographic Analysis	28
2.2.4	Constitutive Modeling	28
2.2.5	Uncertainty Quantification of Experimentally Measured Data	31
2.3	Results and Discussion	32
2.3.1	Al 7085 Chemical Composition and Microstructure Properties.....	32
2.3.2	Mechanical Testing, Fractography, and ISV Model Calibration.....	43
2.3.3	ISV Model Validation.....	56
2.4	Conclusions.....	67
III. A PHYSICALLY MOTIVATED INTERNAL STATE VARIABLE MODEL FOR DUCTILE DAMAGE EVOLUTION DUE TO SHEAR		71
3.1	Introduction.....	71
3.1.1	Damage Modeling History.....	71
3.2	Internal State Variable Constitutive Model	74
3.2.1	Kinematics	74
3.2.2	Thermodynamics.....	81
3.2.3	Kinetics: Plasticity	86
3.2.4	Kinetics: Damage.....	89
3.3	Implementation	97
3.3.1	Void Growth	97
3.3.2	Void Coalescence.....	99
3.3.3	ISV Model Damage Validation	101
3.3.4	Bridgman Notch Tensions Specimen Modeling.....	106
3.3.5	Notch Tension Specimen Damage Evolution for a Heterogeneous Microstructure.....	111
3.4	Conclusions.....	116
IV. USING AN INTERNAL STATE VARIABLE MODEL FRAMEWORK TO INVESTIGATE MICROSTRUCTURE AND MECHANICAL PROPERTY INFLUENCE ON BALLISTIC PERFORMANCE OF STEEL ALLOYS.....		118
4.1	Introduction.....	118
4.1.1	Ballistic Impact Experiments and Modeling.....	118
4.1.2	Material Selection for Ballistic Impact Study.....	120
4.1.3	Internal State Variable Constitutive Model	121
4.2	Methods.....	123
4.2.1	Part I: Ballistic Impact of Rolled Homogeneous Armor Steel Plates by spherical projectiles	123
4.2.2	Finite Element Model Framework	123
4.2.3	Internal State Variable Constitutive Model	127
4.2.4	Part II: Parameter Sensitivity Study.....	133
4.2.4.1	Second Phase Particle Number Density and Size	133

4.2.4.2	Grain Size.....	135
4.2.4.3	Initial Void Volume Fraction.....	136
4.2.4.4	Lattice Hydrogen Concentration.....	137
4.2.4.5	Material Hardness	138
4.2.4.6	Design of Experiments.....	139
4.2.5	Part III: Modeling the Microstructurally Driven Transition in Penetration modes for Varying Target Hardness.....	143
4.3	Results and Discussion	149
4.3.1	Part I: Validation of the Internal State Variable Model Finite Element Framework	149
4.3.2	Part II: Parameter Sensitivity Study.....	150
4.3.3	Part III: Modeling the Microstructurally Driven Transition in Penetration modes for Varying Target Hardness.....	154
4.4	Conclusions.....	158
V. SUMMARY AND FUTURE WORK		160
REFERENCES		164
APPENDIX		
A	INTERNAL STATE VARIABLE MODEL COEFFICIENTS FOR ALUMINUM 7085-T711 ALLOY	187
B	INTERNAL STATE VARIABLE (ISV) MODEL COEFFICIENTS USED IN FINITE ELEMENT SIMULATIONS OF BALLISTIC IMPACT OF STEEL ALLOYS IN CHAPTER IV	189

LIST OF TABLES

2.1	Element weight percent distribution in aluminum 7085-T711 material... 26
2.2	Test matrix for notch Bridgman tension testing used for Internal State Variable (ISV) plasticity-damage model validation.29
2.3	Initial CuFe secondary phase particle property distributions in an aluminum 7085-T711 alloy.....35
2.4	Initial porosity distributions in an aluminum 7085-T711 alloy35
2.5	Grain structure properties of an aluminum 7085-T711 alloy38
2.6	Internal state variable model coefficients for (a) plasticity and (b) damage46
2.7	Void characteristics at fracture for varying strain rate, stress state, and temperature49
3.1	List of stresses and velocity gradients in the various material configurations.80
4.1	Geometric properties of quarter symmetry projectiles and targets used in Abaqus-Explicit finite element analysis simulations.....124
4.2	Second phase particle property distributions in high strength steels from literature sources135
4.3	Mechanical properties and model coefficients for steel alloys of varying Brinell Hardness (BHN).139
4.4	Levels for microstructure and material properties used in parametric sensitivity study.142
4.5	Select test parameter levels and resultant residual velocity values from parameter sensitivity study154
A.1	Internal State Variable (ISV) model coefficients for Aluminum 7085-T711 alloy.....188
B.1	ISV Model Coefficients for 250 BHN RHA steel alloy used in <i>Part I</i> . ..190
B.2	ISV Model coefficients for varying hardness RHA steel alloys used in <i>Part III</i> of Chapter IV.191

LIST OF FIGURES

2.1	Specimen schematics for notch Bridgman tension specimens.	30
2.2	Finite element simulation geometry of Bridgman notched tension specimen.	31
2.3	Elemental distribution mappings acquired from an Energy Dispersive x-ray Spectroscopy (EDS) scan of the Normal Direction (ND).....	33
2.4	Micrographs of FeCu secondary phase particle clusters.....	36
2.5	Micrographs of aluminum 7085-T711 grain structure.....	39
2.6	Inverse pole figures for the RD planar surface of a rolled aluminum 7085-T711 alloy.	41
2.7	Pole figures of grain orientation distributions for an Al 7085-T711 alloy.	42
2.8	Comparison of compressive mechanical responses (generated: Bhattacharrya <i>et al.</i> 2017) of Normal Direction (ND), Rolling Direction (RD), and Transverse Direction (TD).	44
2.9	Calibration of Al 7085-T711 ISV plasticity model for varying strain rate, stress state, and temperature.	47
2.10	Electron micrographs of fracture surface of uniaxial tension specimen deformed at 0.001 s^{-1} and 25°C	50
2.11	Torsional fracture specimen deformed at 0.001s^{-1} strain-rate and 25°C temperature.	51
2.12	The Internal State Variable (ISV) damage model calibration for Al 7085-T711 for varying strain rates, stress states, and temperatures.....	53
2.13	Mesh convergence study for R100 Bridgman notch tension specimen.....	57

2.14	FEA Predicted stress triaxiality evolution for notch Bridgman tension specimens deformed varying temperatures.....	59
2.15	Comparison of experimental and numerical load-displacement data for Bridgman notched tension specimens deformed at varying stress state and temperature.	60
2.16	Electron micrograph of the fracture surface of R100 specimen deformed at 25°C.	63
2.17	Electron micrograph of the fracture surface of R100 specimen deformed at 200°C.	64
2.18	Comparison of experimental and ISV model predicted void property evolution for varying stress state and temperature deformation.	65
3.1	Multiplicative decomposition of the deformation gradient into elastic (F_e) and inelastic (F_d , F_v , and F_θ) components.	74
3.2	Effect of void number density on Nearest Neighbor Distance (NND) and Intervoid Ligament Distance (ILD).	95
3.3	Shear sensitivity parameter effects on ISV model predicted void growth rates.	98
3.4	ISV model predicted Intervoid Ligament Distance (ILD) based void coalescence characteristics.....	100
3.5	Schematic of Dog Bone Shear Concentration (DBSC) specimen used for validation of shear stress dependent void growth model.	101
3.6	Comparison of predicted and observed load-extension behavior for Dog Bone Shear Concentration (DBSC) specimens.....	103
3.7	Electron micrographs of Dog Bone Shear Concentration (DBSC) fracture surface.	104
3.8	Comparison of predicted and observed void evolution characteristics for fractured Dog Bone Shear Concentration (DBSC) specimens.	105
3.9	Comparison of predicted and observed void property evolution for Bridgman notched tension specimens deformed at varying stress states and temperatures.....	107
3.10	Comparison of Finite Element Analysis (FEA) predicted damage evolution and electron micrographs of experimental fracture surfaces for varying notch radii.	110

3.11	Finite element predicted damage evolution in Bridgman notch tension specimens.....	111
3.12	Heterogeneous initial particle number density distribution in an Al 7085-T711 notch tension specimen.....	113
3.13	Heterogeneous distribution of initial void radii in an Al 7085-T711 notch tension specimen.	114
3.14	Comparison of model prediction and observed fracture surface morphology of 2.54 mm notch root radius Bridgman specimen fracture surface.	115
4.1	Abaqus Explicit finite element simulation for ballistic impact of square targets by cylindrical and spherical projectiles.	125
4.2	Mesh convergence study for RHA steel cylinder impacting RHA steel plate at 950 m/s	127
4.3	ISV model mechanical and fracture toughness properties of varying Brinell hardness rolled 4340 Steel alloys.	144
4.4	Microstructure properties at varying hardness levels of RHA steel alloy.	146
4.5	Comparison of experimental and finite element model predicted normalized residual velocities for RHA steel spheres impacting RHA steel plates.	150
4.6	Residual velocity results of 25 impact simulations used to populate array {R} in parametric sensitivity study.	151
4.7	Comparison of residual velocity sensitivity to six parameters for an RHA steel cylinder impacting of 6.35 mm thick RHA steel target.....	151
4.8	Plastic equivalent strain contours for impact perforation of varying Brinell hardness (BHN) rolled homogenous armor steel (RHA) steel plates.	156
4.9	Comparison of Ballistic Merit for varying hardness experimentally impacted 4340 steel alloys (Mescall and Rogers, 1989) and simulated RHA steel.....	158

CHAPTER I

INTRODUCTION

1.1 Motivation

The proliferation of mechanized warfare during World War II gave rise to a natural competition between kinetic penetrator and protective armor systems. The developmental competition between the two systems created the necessity for enhanced predictive based solutions to engineering design problems. As the sophistication of each respective system increased, the existing paradigm of trial-and-error-based design became antiquated and gave way to the fields of computational solid and fluid mechanics as the predictive tools necessary to intelligently guide system designs. The innovation in computational technology during and after the second World War was instrumental to the implementation of constitutive modeling to structural scale complex deformation problems.

In the 1950's and 1960's, Finite-Element Analysis (FEA) methods were developed and implemented in computational codes to address complex engineering problems. Since then, Lagrangian FEA codes including Abaqus Explicit (Dassault, 2014), LS-Dyna (LSCT, 2007), and others have been used to simulate deformation of solid materials for a diverse variety of boundary conditions. Hydrodynamic codes including Epic (Johnson and Stryk, 1987) and CTH (Schumacher and Key, 2009) have also demonstrated the ability to

accurately model high strain-rate, large deformation impact events. Both Lagrangian and hydrodynamic FEA frameworks have been used in conjunction with a wide variety of constitutive models including the Gurson (1977), Johnson-Cook (1983), and equation of state (Hugoniot, 1887; Gruneisen, 1912) models to simulate impact deformation. However, these constitutive models are often unable to accurately capture all deformation characteristics because they generally do not account for the effect of a material's dissipative thermomechanical history on future deformation behavior.

Over the past 30 years, a constitutive model based upon internal state variable (ISV) theory has been developed by Bammann (1984) and refined by Horstemeyer *et al.* (2000A) for use as a tool for predicting deformation. The model uses ISV's to account for the dissipative thermomechanical plasticity and damage evolution of a material subjected to deformation. The ISV model has been applied to several crystalline materials including steel (Horstemeyer and Ramaswamy, 2000; Horstemeyer *et al.* 2000B; Whittington *et al.* 2014;), aluminum (Horstemeyer *et al.* 2000A; Hostemeyer and Ramaswamy, 2000; Agarwal *et al.* 2003; Horstemeyer *et al.* 2003B; Jordon, 2007; Tucker *et al.* 2010), magnesium (Walton *et al.* 2014; Horstemeyer and Chaudhuri, 2015) and has been extended to polymer materials (Bouvard, 2013; Francis 2014). A wide range of deformations have been successfully modeled including forming processes (Bammann *et al.* 1996; Horstemeyer, 2000; Cho *et al.* 2015), high strain rate deformation (Whittington *et al.* 2014), and structural crashworthiness (Bammann *et al.* 1993). The intent of this study is to extend the ISV model's predictive capability with the goal of implementing the model to accurately simulate the ballistic impact of a metallic structure. The study's hypothesis

is that if the structure-property mechanisms of plasticity and damage evolution under shearing can be quantified, then the dynamic impact of ductile metal structures can be modeled accurately.

1.2 Current State of the Literature

1.2.1 Impact Mechanics

1.2.1.1 Wave Mechanics

High velocity ballistic impact of crystalline materials involves significant inelastic deformation at high strain rates. Much of the plasticity and damage associated with impact events occurs due to behavior of stress waves (often referred to as pressure or shock waves) within the target and impactor materials. Following the second World War, emphasis was placed upon understanding the mechanics of waves in solids to improve weapons and protective systems designs.

The basis for the standard methodology for performing high strain rate experiments of solid materials and interpreting experimental data was established by Kolsky (1949). Kolsky's work yielded the compressive pressure bar apparatus, commonly referred to as a Kolsky or split-Hopkinson bar based upon the experimental work of Hopkinson (1914). From 1950-1990, a vast amount of research efforts focused on both the effects of elastic and inelastic stress wave behavior in solids subjected to high strain rates including the works of von Karman and Duwez (1950), Davies (1956), Davies and Hunter (1963), Bjork (1963), Yang (1966), Wood and Phillips (1967), Hill (1969), Fowles and Williams (1970), Dunn and Davern (1986), Koller and Kolsky (1987), and Mead (1996). These works

investigated dynamic impact stress-strain distributions (von Karman and Duwez, 1950), dynamic testing procedures (Davies, 1956; Davies and Hunter, 1963), transverse shear waves (Yang, 1963), phased dynamic stress-strain relationship (Hill, 1969; Fowles and Williams, 1970), interfacial impedance effects (Dann and Davern, 1986) and dynamic wave to free surface interaction (Koller and Kolsky, 1987).

Drop weight testing has been employed in addition to Kolsky bar testing for experimental observation of dynamic deformation. Drop weight testing experiments have been established for composite materials (Winkel and Adams, 1985), concrete (Banthia *et al.* 1989), steel (Sreenivasan *et al.* 1992), and cross-ply laminates (Hsiao *et al.* 1998).

Interest has been given to addressing strain localization for high strain rate deformation. Investigations into the thermal diffusion, microstructure evolution, and grain structure effects on dynamic shear band formation during high strain rate deformation have been performed by Clifton *et al.* (1984), Nasser *et al.* (1989) and Meyers *et al.* (1995).

The damage mechanisms associated with impact, particularly ballistic impacts, have been rigorously investigated. Corbett *et al.* (1996) provided a comprehensive review on experimental and modeling efforts pertaining to ballistic penetration. Backman and Goldsmith (1978) reviewed much of the fundamental early literature pertaining to ballistic impact and penetration. They describe plate impact damage mechanisms: (1) fracture due to stress waves (Tsai and Kolsky, 1967; Bowden and Field, 1964; Camacho and Ortiz, 1996), (2) radial fracture behind a stress wave (Evans *et al.* 1978, Johnson, 1981; Camacho and Ortiz, 1996), (3) spallation (Curran *et al.* 1977; Johnson, 1981; Meyers, 1983; Curran *et al.* 1987; Grady, 1988), (4) shear plugging (Ipson, 1963; Awebuch and Bodner, 1974;

Curran *et al.* 1977, Goldsmith and Finnegan, 1986; Børvik *et al.* 1999), (5) petaling (Goldsmith *et al.* 1965; Awerbuch and Bodner, 1974; Levy and Goldsmith, 1984; Hou and Goldsmith, 1996), (6) fragmentation (Johnson, 1981; Grady, 1982; Grady and Kipp, 1985; Glenn and Chudnovsky, 1986), and (7) ductile hole enlargement (Thomson, 1955).

1.2.1.2 Energy Absorption

The energy absorption capacity and the associated mechanisms of absorption are intrinsic to a material's ability to resist failure during impact loads. Much of the literature associated with dynamic energy absorptive mechanisms centers around energy absorbed due to inelastic deformation and energy dissipated by the stress waves generated by the impact. An early study by Raman (1920) used the elastic collision theory developed by Hertz (1896) to formulate the kinetic and potential energy of flexural waves generated during elastic impact. Zener (1941) performed one of the earliest investigations into the effects of inelasticity during the impact of solids materials and observed the relationship between inelastic deformation and force impulse amplitude and duration. Tillett (1954) showed an inverse relationship between anelastic relaxation and the coefficient of restitution of impacting bodies.

Since the 1950's, a volume of research has correlated the energy dissipation during impact due to wave propagation including the works of Hunter (1957), Hutchings (1979), Reed (1985), Tasdermirci and Hall (2007), Hui *et al.* (2011), and Krijt *et al.* (2013). Hunter (1957) calculated the energy absorption due to elastic waves during impact using a Fourier force-time approximation of the Hertz (1896) displacement-time framework. Later,

Hunter's model was reformulated by Reed (1985) to more closely match Hertzian theory, which resulted in greater predicted dissipation due to elastic waves. Hutchings (1979) showed the energy dissipation of elastic waves in descending order of contribution was due to Rayleigh (surface), transverse shear, and longitudinal compression waves but plastic deformation was shown to be more effective in dissipating energy in accordance with Uetz and Gommel (1966). Krijit *et al.* (2013) coupled the effects of adhesion, viscoelasticity, and plastic deformation to accurately predict energy dissipation during impact. The effects of multi-layered and functionally graded materials are discussed by Tasdemirci and Hall (2007) and Hui and Dutta (2011), respectively.

1.2.2 Damage Modeling History

Modeling damage evolution is essential to the accurate prediction of inelastic deformation behavior of materials. The early foundations of damage mechanics were established in the works of Griffith (1921) and later refined by the linear elastic fracture mechanics (LEFM) paradigm established by Irwin (1948; 1957). Even with Irwin's contributions, the capability of the fracture model was limited to linear-elastic solids like glass or brittle crystalline materials.

The modeling of damage began to develop in sophistication in the 1950's due to the consideration of microstructural damage evolution. Kachanov (1957) conceived the notion of microvoid-based damage evolution due to creep conditions. Rabotnov (1963) built upon Kachanov's concept by deriving void growth rate equations for materials undergoing creep. In 1967, Coleman and Gurtin introduced a model framework that

proposed the use of ISVs through the Clausius-Duhem thermodynamic inequality (1911) for the description of dissipative mechanisms associated with inelastic material deformation. The ISV framework offered a novel approach to the description of microstructural to macrostructural damage evolution's effect on the kinetics of most materials, transcending the linear elastic limitations of the early fracture mechanics paradigm. Soon thereafter, McClintock (1968), Rice and Tracey (1969), and Gurson (1977) proposed models for the growth of voids during deformation with particular emphasis placed upon the effects of stress state triaxiality on damage evolution. These early models accomplished considerable advancement in the ability to predict the deformation of elasto-viscoplastic materials, however, none made explicit use of the ISV's potential within the Coleman and Gurtin thermodynamic framework to capture the path dependent energy history of material deformation.

Similar works ensued building off the early void growth theories. In 1979, Bourcier and Koss investigated the orientation effects of neighboring voids in aluminum, thus establishing the paradigm for void interaction and coalescence. Budiansky *et al.* (1982) established a relationship between void growth and the material hardening rate and the effect of stress state on void shape. They showed that triaxial stress states tended to grow spherical voids at exponential rates, but other stress states could produce asymmetric voids. In 1982, Cocks and Ashby developed a model that coupled the effects of grain-boundary diffusion, void surface diffusion, and creep for predicting void growth.

An ISV framework was employed to model damage evolution in a ductile metal material by Bammann, Chiesa, and Johnson (BCJ model) (1996) using a void growth

parameter motivated by the Cocks-Ashby growth model. A study performed by Marin and McDowell (1996) investigated the effects of associative, partially associative, and non-associativity of an earlier iteration of the BCJ model framework (1993) and demonstrated the effectiveness of a fully associative flow rule at capturing post necking behavior, which is dominated by damage evolution. In 1999, Horstemeyer and Gokahle revised the BCJ model to consider the effects of a coupled void nucleation, growth, and coalescence regime using ISVs to represent each individual mechanisms' evolution during deformation.

1.2.3 Shearing

1.2.3.1 Shearing Experiments

A wide range of experimental methods exist to observe shear deformation mechanisms under a variety of stress states, strain rates, and temperatures. Many standard testing methods are detailed in Kuhn (2000) and Gilat (2000). Kuhn (2000) details experimental procedures for in plane shear testing via short beam, blanking-shear, double notched shear, rail shear, double V-notch, 45° tensile, biaxial shear, and torsion at elevated temperature. A torsion experimental procedure using the twisting of thin walled tubes is discussed in Semiatin (1985). Multiaxial beam and plate experimental procedures are described by Dieter (1976) for narrow beams and Shewchuk (1968) and Ziebs (1996) for rhombic and elliptical plates. Taylor (1988) describes the procedures for hydraulic bulge and spherical punch testing. Multiaxial experiments for thin-walled tubes have been described for quasi-static (Fernando *et al.* 1990) and creep (Browne *et al.* 1991) conditions. Biaxial mechanical testing of cruciform sheets by load application via chains, pulleys, and

levers (Mukai *et al.* 1996), motors (Boehler *et al.* 1994), and hydraulic cylinders (Phaal *et al.* 1995) has been described.

A research focus into the high strain-rate behavior of materials developed over the latter half of the 20th century. Emphasis was placed upon the effects of torsion at high strain-rates, especially with regards to strain localization and damage evolution. Gilat (2000) provides a comprehensive review of high rate torsional experimentation using modified Kolsky bar schemes. Baker and Yew (1966) developed an early modification of the Kolsky (1949) compression bar apparatus for torsional experimentation. Yew and Richardson (1966) investigated the torsional plastic behavior of metal tubes using a torsional Kolsky bar, however, the strain rates were limited to 500 s⁻¹ for their experiments.

The experimental study of strain localization and shear band formation is thoroughly documented in the literature. Zener and Hollomon (1944) observed the strain localization associated with plastic deformation of tensile specimens tested at a variety of temperatures and strain rates. Marchand and Duffy (1988) and later Ramesh (1994) observed strain localization and shear band formation in thin walled tubes tested on a torsional Kolsky bar apparatus. Novel procedures for studying shear band development due to torsion and a near simple shear stress state have been developed by Deltort (1994) and Meyers *et al.* (1994), respectively. Zhou (1996) and later Guduru *et al.* (2001) observed shear band propagation in metal plates under asymmetric, dynamic, mode II shear loading. Da Silva and Ramesh (1997) investigated shear localization in solid and porous Ti-6Al-4V using servo-hydraulic machines and torsional Kolsky bars for quasistatic and high strain rates, respectively. Chichilli *et al.* (2004) employed a torsional Kolsky bar

sample recovery technique (developed in Chichili, 1999) to study the dynamic shear band formation in the absence of fracture. Rittel *et al.* (2002) developed a novel cylindrical specimen for static or dynamic compression testing that produced a shear dominated gauge section stress state. Shear band formation due to implosion loading of thin-walled tubes (Xue *et al.* 2002) and ballistic loading of steel plates (Duan *et al.* 2003) has been documented.

1.2.3.2 Shearing in Plasticity and Damage Modeling

The evolution of the field of macroscale plasticity modeling is intrinsic to the modeling of shear deformation mechanisms. Some of the earliest works in modeling plastic deformation date back to the piecewise yield criterion established by Tresca (1864). Saint-Venant (1870) and Levy (1870) applied the Tresca yield criterion to plasticity problems. Von Mises (1913, 1928) extended Tresca's yield criterion to form a continuous yield function that would better suit subsequent plasticity models. Prager (1945) developed a plasticity model that accounted for strain hardening effects via stress invariant theory. Drucker (1951, 1957) established a yield surface convexity requirement for stable inelastic deformation, resulting in the favorability of the von Mises yield criterion in future plasticity models. Green and Naghdi (1965) established one of the earliest elasto-plasticity models to be posed in a continuum kinematic and thermodynamic framework. Coleman and Gurtin (1967) and Kestin and Rice (1969) proposed the use of ISVs within a thermodynamic framework to account for energy dissipation associated with inelastic deformation. In 1971, Rice formulated the relationship between internal variables and inelastic flow

through kinematic and thermodynamic developments. Bammann (1984) established an ISV based model for visco-plasticity. Bammann and Johnson (1987) refined the Bammann ISV model for inelastic deformation and implemented a novel approach to the multiplicative decomposition of fundamental kinematic tensors. Bammann (1990) extended the ISV plasticity model framework to account for the effects of temperature and strain rate on inelastic deformation.

The specific application of macroscale plasticity and damage modeling focuses on addressing shear band plasticity due to strain localization and shear-based damage evolution and fracture. The early macroscale plasticity constitutive models for the evolution of shear bands, strain localization, and necking, are developed in the works of Stören and Rice (1975), Rudnicki and Rice (1975), Rice (1976; 1980), Asaro and Rice (1977), Needleman and Rice (1978), Hutchinson (1981; 1983), Tvergaard and Needleman (1984), Mear and Hutchinson (1985), and Anderson *et al.* (1990). The application of fracture mechanics principles for macroscale crack evolution under shear deformation modes is presented in Hutchinson (1990), Huang 1999, Kim *et al.* (2002), Park *et al.* (2009), and Sharanaprabhu and Kudari (2010). The use J_3 deviatoric stress invariant theory for predicting rupture of materials under shear and strain localization effects has been primarily advanced by the research collaborations of Tomasz Wierzbicki. The team's works include publications from Bao and Wierzbicki (2004A; 2004B), Teng and Wierzbicki (2006; 2007), Xue (2007; 2008A; 2008B), Bai (2008A; 2008B; 2010). Other publications reviewing or applying J_3 theory to shear related failure include Nashon and Hutchinson (2008), Dunand and Mohr (2011) and Giglio *et al.* 2012.

1.2.3.3 Nonlocal Methods for Constitutive Modeling of Damage Evolution

Damage evolution in ductile metals is inherently subject to nonlocal influences. For example, Bourcier and Koss (1979) demonstrated that void coalescence mechanisms are influenced by neighbor distances and orientation. Many efforts have focused on development of nonlocal plasticity and damage models to capture nonlocal phenomenological effects and reduce numerical instabilities in FEA models. Beran and McCoy (1970) used strain gradient theory to develop a solution of a homogeneous bulk material with local heterogeneities. Eringen developed elastic models with nonlocal body forces (1972) to compute finite crack tip stresses (1974; 1977). Studies have proposed the use of spatially averaged higher order damage formulation for accurate modeling of strain softening regimes (Pijaudier-Cabot and Bazant, 1987; Lasry and Belytschko, 1987; Aifantis, 1992; Zbib and Aifantis, 1992). Fleck and Hutchinson (1993) proposed a phenomenologically based model with higher order spatial gradient formulation for plastic strain as a solution to mesh sensitivity. Recently gradient dependent models for plastic strain and damage have been successfully implemented within user material subroutine constitutive models for Abaqus FEA software (Al-Rub and Voyiadjis, 2005; Al-Rub and Darabi, 2010).

1.2.4 Materials of Interest

1.2.4.1 Rolled Homogeneous Armor Steel

Rolled homogeneous armor (RHA) steels is a class of materials that feature high yield, ultimate strength, hardness, and strain hardenability to resist high strain rate

deformation associated with ballistic impact. The chemical composition restrictions and mechanical property requirements for RHA steels are described in a publicly available material specifications document from the U.S. Department of Defense (U.S. 1984). The RHA class of steels typically feature a martensitic (Prifti *et al.* 1997) or bainitic (Moss and Seaman, 1980) grain structure to achieve the desired strength properties. The elastic moduli and mechanical strength of RHA class steels have been experimentally observed at quasi-static strain-rates (Benk, 1976; Benk and Robitaille, 1977). Fracture in RHA steels has been shown to initiate, grow, and coalesce from microstructural inclusion particles and other defects during deformation (Moss and Seaman, 1980). A comprehensive study on the microstructural void evolution characteristics of RHA steel tested under a wide range of strain rates and temperatures for various stress states has been performed by Whittington *et al.* (2014).

The high strain-rate deformation characteristics of RHA steels are usually of interest due to the material's intended application of dynamic mechanical deformation resistance. Studies have been performed for RHA subjected to high strain rates at elevated temperatures (Gray *et al.* 1994), ballistic impact conditions (Gupta and Madhu, 1997), varying material hardness (Weerasooriya and Moy, 2004), and various stress states and temperatures (Whittington, 2014). Often, RHA plates are used as a basis for comparison for other ballistic impact mitigation materials or for impactor study (Magness, 1994). Attempts have been made to improve previously validated classes of RHA steel through chemistry control and optimized heat treatments (Prifti *et al.* 1997) and recasting and hot working processes (Hu *et al.* 2002).

1.2.4.2. Aluminum 7085

Aluminum 7085 is a relatively recent permutation of the 7075 alloy with an Al-Zn-Mg-Cu chemical composition developed by ALCOA in 2003. Due to the relatively recent development of the material, literature pertaining to its mechanical and microstructural properties is not as abundant as for other class 7XXX aluminums. Jabra *et al.* (2006) observed the deleterious effect of elevated temperature exposure to die-cast and plate Al 7085 alloys. Luong and Hill (2008) noted that surface plasticity induced by laser peening and anodization processing markedly improved the fatigue life of an Al 7085 alloy material. In 2009, Shuey *et al.* and Karabin *et al.* determined the fracture toughness of an aged Al 7085-T7XX alloy using experimentation and finite element analysis, respectively. He *et al.* (2012) determined the thermomechanical effects of exposure to a large magnetic field to various constituent phases of 7085 aluminum. The effects of post mechanical processing homogenization and solution-hardening heat treatments have been investigated by Chen *et al.* (2012A; 2012B; 2013A; 2013B). Chen *et al.* (2013B) demonstrated an Al 7085 microstructural and mechanical property dependence on processing strain rates and temperatures. Recently, Bhattacharyya *et al.* (2017) used a viscoplastic self-consistent (VPSC) model to model strain rate and grain orientation effects on the plasticity of an anisotropic Al 7085-T711 temper material. Bhattacharyya *et al.* (2018) modeled the plasticity characteristics of a variety of Al 7085 tempers using an elastoplastic self-consistent (EPSC) model.

1.3 Dissertation Structure

Chapter I presents a broad overview of the motivation for the dissertation research and a brief review of the literature pertaining to impact mechanics, damage modeling, experiments and models related to shear, and alloy materials examined in this research.

Chapter II presents the material characterization and structure-property quantification of an Al 7085-T711 alloy. The strain rate, stress state, and temperature dependent mechanical behavior of a hot rolled aluminum 7085-T711 alloy is experimentally observed and subsequently modeled using a continuum Internal State Variable (ISV) plasticity-damage constitutive model. Structure-property relationships for the alloy are quantified using a series of microstructural analyses and mechanical property experiments. The calibrated ISV model for the Al 7085-T711 alloy is implemented in an implicit finite element code (Abaqus) to simulate the deformation of notch Bridgman tension specimens at a variety of stress states and temperatures. The ISV model accurately captures the material's elastoplastic behavior by predicting the stress state difference between tension, compression, and torsion and temperature dependent microstructure evolution under large deformations.

Chapter III discusses the use of J_3 deviatoric stress invariant theory to model shear influenced void growth in an ISV model framework. Additionally, void coalescence is cast as a function of a nearest neighbor distance term that evolves with void nucleation and growth and, thus incorporates the fulfillment of J_3 shearing. The ISV model reformulation is validated using FEA simulation-based prediction of mechanical and microstructure evolution of a variety of aluminum 7085 structures under mechanical deformation.

Chapter IV details the use of an ISV based constitutive model for RHA steel within a Lagrangian FEA framework to simulate ballistic impact of monolithic steel plates by cylindrical and spherical projectiles. The simulation framework is validated through accurate prediction of experimental impact of RHA steel targets of varying thickness by RHA steel spheres. A simulation based parametric sensitivity study was performed to determine the influence of a variety of microstructure and mechanical properties on ballistic performance. Finite element simulations show that variation of microstructure properties could explain the reduced ballistic performance of high hardness materials previously documented in the literature. Chapter V summarizes the work in Chapters II-IV and discusses future research opportunities related those studies.

CHAPTER II
AN INTERNAL STATE VARIABLE PLASTICITY-DAMAGE MODEL OF AN
ALUMINUM 7085-T711 ALLOY UNDER LARGE DEFORMATIONS
AT VARIOUS STRAIN RATES, STRESS STATES
AND TEMPERATURES

2.1 Introduction

2.1.1 Aluminum 7085 Alloy

Aluminum 7085 is a relatively high strength, aerospace grade alloy developed by Alcoa in 2002 for application in the aerospace, automobile, and defense industries. As with other types of 7XXX series aluminum, the primary alloying elements consist of Zn and Mg, which are used to strengthen the material by facilitating precipitation hardening mechanisms. While abundant literature pertaining to the 7xxx series aluminum exists, little literature exists specifically addressing the structure-property relationships of Al 7085. Much of the current literature related to Al 7085 focuses on thermomechanical processing effects on the material microstructure and mechanical properties. In 2006, Jabra *et al.* observed the deleterious effect of elevated temperature and deformation to die-cast and plate Al 7085 alloys. Chen *et al.* (2012A, B; 2013A, B) showed that solution-hardening heat treatments produced smaller grain and precipitate structures than homogenization

treatments which resulted in higher flow stresses for solution-hardened materials at comparable test conditions. Within the literature, relatively few studies have modeled the deformation characteristics of Al 7085. However, Karabin *et al.* (2009) simulated the fracture characteristics of the alloy using experimental fracture data generated by Shuey *et al.* (2009). Recently, Bhattacharyya *et al.* (2017) used a viscoplastic self-consistent approach to model strain rate and grain orientation effects on anisotropic plasticity of an Al 7085-T711 temper material. Later, Bhattacharyya *et al.* (2018) modeled the plasticity characteristics of a variety of Al 7085 tempers.

2.1.2 Internal State Variable Based Approach to Constitutive Modeling

The purpose of the current study is to quantify the structure-property relationships of a hot rolled, solution hardened Al 7085-T711 alloy for implementation in an Internal State Variable (ISV) based constitutive model within a predictive Finite Element Analysis (FEA) framework. A physics-based viscoplasticity model was developed by Bammann (1984) within an ISV thermodynamic framework established by Coleman and Gurtin (1967). Bammann's ISV plasticity model was revised to account for damage in the form of void volume fraction (Bammann and Aifantis, 1989) and later refined to consider damage evolution stemming from the nucleation (Horstemeyer and Gokhale, 1999; Horstemeyer *et al.* 2003), growth, and coalescence of voids (Horstemeyer *et al.* 2000A). The model implements McClintock's (1968) void growth rule for voids growing from secondary phase particles and Cocks and Ashby's (1982) unified growth mechanism model for pre-existing voids. The ISV plasticity-damage model has been used to characterize the

structure-property relationships for aluminum (Horstemeyer *et al.* 2000A; Jordon, 2007; Tucker *et al.* 2010), steel (Horstemeyer *et al.* 2000B; Horstemeyer and Ramaswamy, 2000; Guo *et al.* 2005; Anurag *et al.* 2009; Whittington *et al.* 2014), copper (Crapps *et al.* 2010), titanium (Guo *et al.* 2005), and magnesium (Lugo *et al.* 2011; Walton *et al.* 2014; Lugo *et al.* 2018) alloys. The constitutive model has been used within an FEA framework to successfully simulate a variety of thermomechanical deformations including forming processes (Bammann *et al.* 1996; Horstemeyer and Ramaswamy, 2000; Crapps *et al.* 2010; Cho *et al.* 2015; Cho *et al.* 2018), high velocity impacts (Whittington *et al.* 2014), and structural crashworthiness (Bammann *et al.* 1993; Horstemeyer *et al.* 2005; Horstemeyer *et al.* 2009).

A theory for ISV plasticity and damage modeling has been thoroughly developed by Bammann (1984; 1989; 1996) and Horstemeyer (1999; 2000A; 2001; 2003A). A key aspect of the theory is to characterize a material's history of internal dissipative mechanisms and the relationship between load history effects to predict the future constitutive behavior. The material history is strongly influenced by the plasticity-based hardening and porosity-based softening mechanisms, although the selection and implementation of appropriate ISVs may be somewhat subjective. Horstemeyer *et al.* (2003B) noted that the ISV plasticity-damage model incorporates deviatoric inelastic deformation resulting from the presence of dislocations in crystallographic materials, dilatational deformation, and ensuing failure from damage progression. Here damage was noted to reduce material strength, increase inelastic flow rate, and increase compliance.

A summary of the ISV plasticity-damage model relations is provided in the following section. A standard tensorial notation is employed. Assume a nominal parameter, (A) . Bold symbols denote second rank tensors (A) . Rate functions are denoted by a dot accent (\dot{A}) . Frame indifferent second rank tensors are denoted by an overbar and dot accent $(\overline{\dot{A}})$.

The kinetic constitutive relationship between stress and strain is observed to be strain rate, stress state, and temperature dependent in nature for many ductile materials. Microstructural characteristics such as the presence of dislocations, secondary phase particles, and voids are known to influence the mechanical behavior of materials. The following kinetic and kinematic constitutive relations describe the frame indifferent stress rate, elastic rate of deformation, and inelastic flow, respectively:

$$\overline{\dot{\sigma}} = \dot{\sigma} - W_e \sigma + \sigma W_e = \lambda(1 - \phi) + 2\mu(1 - \phi)D_e - \frac{\phi}{1 - \phi} \sigma \quad (2.1)$$

$$D_e = D - D_{in}, \quad (2.2)$$

$$D_{in} = \sqrt{\frac{3}{2}} f(T) \left[\frac{\left[\frac{\sqrt{3}}{2} \left\| \sigma' - \sqrt{\frac{2}{3}} \alpha \right\| - (R + Y(T))(1 - \phi) \right]}{V(T)(1 - \phi)} \right] \cdot \frac{\sigma' - \sqrt{\frac{2}{3}} \alpha}{\left\| \sigma' - \sqrt{\frac{2}{3}} \alpha \right\|} \quad (2.3)$$

Here, an objective (frame indifferent) Jaumann stress rate, $\overline{\dot{\sigma}}$, is assumed such that the total spin tensor is equivalent to the elastic spin tensor, W_e (*i.e.*, the inelastic spin is negligible). σ describes the Cauchy stress tensor in the current configuration, and λ and μ are Lamé elastic constants. D , D_e , and D_{in} are the total, elastic, and inelastic rate of deformation tensors, respectively. The void volume fraction, ϕ , is used to define the extent of damage.

In Eq. (2.3), creep and plasticity are accounted for through specification of the inelastic rate of deformation, \mathbf{D}_{in} , as a function of temperature (T), deviatoric stress tensor ($\boldsymbol{\sigma}'$), kinematic hardening ISV ($\boldsymbol{\alpha}$), isotropic hardening ISV (R), void volume fraction (ϕ), and yield related functions $Y(T)$, $f(T)$, and $V(T)$. The functions $Y(T)$, $f(T)$, and $V(T)$ have an Arrhenius-type temperature dependence as described in Bammann *et al.* (1993). In general, $Y(T)$, $f(T)$, and $V(T)$ are used to characterize the rate independent yield stress, threshold for strain rate dependent yielding, and influence of loading rate on yielding, respectively. Monotonic compression, tension, and torsion tests at different temperatures and strain rates are used to determine the functions $f(T)$, $V(T)$, and $Y(T)$. Equations (2.1) and (2.3) reflect the tendency for damage, ϕ , to increase compliance and increase inelastic flow rate (leading to strain localization), respectively.

ISVs that account for dislocation density effects control the plasticity evolution of the constitutive model. Kinematic and isotropic hardening ISVs ($\boldsymbol{\alpha}$ and R) are used to represent the effects of geometrically necessary and statistically stored dislocation densities, respectively. The frame indifferent kinematic hardening rate, $\dot{\bar{\boldsymbol{\alpha}}}$, and isotropic hardening rate, \dot{R} , are described in Jordon be described as

$$\dot{\bar{\boldsymbol{\alpha}}} = \dot{\boldsymbol{\alpha}} - \mathbf{W}_e \boldsymbol{\alpha} + \boldsymbol{\alpha} \mathbf{W}_e = \left(h(T) \mathbf{D}_{in} - \left[\sqrt{\frac{2}{3}} r_d(T) + r_s(T) \right] \|\boldsymbol{\alpha}\| \boldsymbol{\alpha} \right) \left(\frac{G_{S0}}{G_S} \right)^Z, \quad (2.4)$$

where $h(T)$ represents the kinematic hardening modulus, and $r_s(T)$ and $r_d(T)$ are scalar functions describing the static and dynamic recovery for kinematic hardening, respectively.

Similarly, the frame indifferent isotropic hardening rate, \dot{R} , may be expressed as

$$\dot{R} = \left(H(T) \sqrt{2/3} \mathbf{D}_{in} - \left[\sqrt{2/3} R_d(T) \|\mathbf{D}_{in}\| + R_s(T) \right] R^2 \right) \left(\frac{GS0}{GS} \right)^Z. \quad (2.5)$$

where $H(T)$ characterizes the isotropic hardening modulus, and $R_s(T)$ and $R_d(T)$ account for the static and dynamic recoveries for isotropic hardening. Equations (2.4) and (2.5) each account for grain growth dependence (where $GS0$ and GS represent the initial and final grain sizes, respectively) and strain-rate dependence.

Within ductile materials, damage primarily consists of microstructural porosity. Significant levels of damage cause an increase in compliance and contribute to strain localization. Damage evolution in ductile materials arises due to the nucleation, growth, and coalescence of voids (*cf.* Horstemeyer *et al.* 2000A) from microstructural heterogeneities during deformation. Additionally, pre-existing voids (pores) due to processing defects may grow and coalesce during deformation. The total porosity evolution equation (*cf.* Jordon *et al.* 2007) is may be expressed as:

$$\dot{\phi} = [\dot{\phi}_{particles} + \dot{\phi}_{pores}]C + [\phi_{particles} + \phi_{pores}]\dot{C}, \quad (2.6)$$

where C is a coalescence parameter, \dot{C} is the rate of void coalescence, $\phi_{particles}$ is the *current* volume fraction of voids nucleated from particles during deformation, and ϕ_{pores} is the *current* volume fraction of pre-existing voids. The rate of change in volume fraction of nucleated and pre-existing voids may be written as (*cf.* Jordon *et al.* 2007):

$$\dot{\phi}_{particles} = \dot{\eta}\nu + \eta\dot{\nu}, \quad (2.7)$$

and

$$\dot{\phi}_{pores} = \left[\frac{1}{(1-\phi_{pore})^m} - (1 - \phi_{pore}) \right] \sinh \left[\frac{(2V(T)/Y(T))-1}{(2V(T)/Y(T))+1} \cdot \frac{I_1}{3\sqrt{J_2}} \right] \|\mathbf{D}_{in}\|. \quad (2.8)$$

In Eq. (2.7), $\dot{\phi}_{particles}$ is a function of the average void number density (η), average void volume (v), void nucleation rate ($\dot{\eta}$), and void growth rate (\dot{v}). The expression for $\dot{\phi}_{pores}$ in Eq. (2.8) was formulated using the Cocks-Ashby (1982) damage evolution framework to account for stress triaxiality and strain-rate effects for pre-existing pores: m is the Cocks-Ashby calibration coefficient; the ratio $V(T)/Y(T)$ accounts for strain rate sensitivity; and the first stress invariant (I_1) and second deviatoric stress invariant (J_2) account for the effect of stress triaxiality on pore growth rates.

Horstemeyer (1999; 2000A, 2003A) employed ISVs to represent the effects of void nucleation from second phase particles, their associated growth and coalescence on the total void volume fraction (damage) within ductile materials. Void nucleation, growth, and coalescence rates exhibit material dependent strain rate, stress state, and thermal sensitivities. Horstemeyer and Gokhale (1999) posed the void nucleation rate as,

$$\dot{\eta} = \frac{d^{1/2}}{K_{IC} f^{1/3}} \eta \cdot \left(a \left[\frac{4}{27} - \frac{J_3^2}{J_2^3} \right] + b \frac{J_3}{J_2^{3/2}} + c \left\| \frac{I_1}{\sqrt{J_2}} \right\| \right) \|\mathbf{D}_{in}\| \exp \left(C_{\eta T} / T \right), \quad (2.9)$$

Here, K_{IC} is the fracture toughness, d is the secondary phase particle size, f is secondary phase particle volume fraction, and J_3 is the third deviatoric stress invariant. The stress state sensitivity is modeled using the invariants I_1 , J_2 and J_3 . The calibration parameters a , b , and c control the shear sensitivity, distinguish between tension and compression, and capture the stress triaxiality sensitivity, respectively. Consistent with Dighe *et al.* (1998),

the void nucleation rate ($\dot{\eta}$) is dependent on temperature (T) and the calibration constant ($C_{\eta T}$) is used to control the magnitude of temperature dependence.

McClintock (1968) developed a void growth framework that captures the effects of thermal and stress state dependence on void growth mechanisms. Using this framework, a void growth evolution equation may be expressed as (Peterson *et al.* 2019)

$$\dot{v} = \frac{\pi}{6} \left(\left\{ A_{void} D_0 \left[1 - \left(\frac{27J_3}{2(3J_2)^{3/2}} \right)^2 \right] \frac{D_{ij}^d : \sigma'_{ij}}{\sqrt{3}J_2} + B_{void} D_0 \frac{J_3}{J_2^2} \|\underline{D}^{in}\| + \frac{\sqrt{3}D_0}{2(1-n)} \left[\sinh \left(\sqrt{3}(1-n) \frac{\sqrt{2}I_1}{3\sqrt{J_2}} \right) \right] \|\underline{D}^{in}\| \right\} \exp(C_{Tv} \cdot T) \right)^3 \quad (2.10)$$

where D_0 is the average initial diameter of voids in the material. Similar to the relation for void nucleation rate (Eq. 9), the void growth rate relation (\dot{v}) employs stress invariant ratios to account for stress state effects. Parameters A_{void} , B_{void} , and n control the shear sensitivity, distinguish between tension and compression, and the stress triaxiality sensitivity of the void growth rate, respectively. Additionally, the calibration constant C_{Tv} controls the void growth ISV's temperature dependence. Analogously, an expression for void coalescence rate (\dot{C}) was developed that accounts for the effects of void nucleation and coalescence (Horstemeyer *et al.* 2000A), grain size (Jordon *et al.* 2007) and void nearest neighbor distance effects (Allison, 2009),

$$\dot{C} = \left[\left(\frac{4D_0}{NND} \right)^\zeta + cd_2 [\dot{\eta}v + \dot{v}\eta] \right] \exp(C_{CT}T) \left(\frac{GS_0}{GS} \right)^z. \quad (2.11)$$

where D_0 is the average initial void diameter, v is the average void volume, η is the average void number density, NND is the average nearest neighbor distance between voids, ζ is a

dimensionless length scale calibration parameter, GS_0 represents the initial grain size, and GS accounts for grain growth due to recrystallization.

2.2 Experimental Procedure

2.2.1 Microstructural Characterization

Quantitative microstructural analysis of an Al 7085-T711 alloy was performed to calibrate physically motivated ISV model material property constants. Bulk chemical analysis of the alloy was performed using mass spectrometry. The major element constituent distribution is given by Table 2.1. Specimens were prepared with microstructures aligned in the, Normal Direction (ND), Rolling Direction (RD), and Transverse Direction (TD) material directions to assess potential anisotropy of the microstructure. These specimens were polished using increasingly fine grit silicon carbide paper. The final polish was achieved using an OP-S 0.04 μm colloidal silica suspension on a Struers TegraPol 21 machine. Specimens selected for grain analysis were then etched using a modification of Weck's (1986) technique developed by Zwiig (2001) for etching wrought aluminum alloys. As an aside, the K-MnO₃ etchant used to delineate grain boundaries attacks secondary phase particles, making Optical Microscopy (OM) unsuitable for characterization of particle properties.

Table 2.1 Element weight percent distribution in aluminum 7085-T711 material.

	Al	Zn	Cu	Mg	Zr	Si	Ti	Fe	Ni
Nominal	88.85	7.40	1.725	1.5	0.125	0.0408	0.0378	0.0365	0.0237
	± 0.2380	± 0.1359	± 0.0238	± 0.0316	± 0.0048	± 0.0361	± 0.0271	± 0.0049	± 0.0240

Scanning Electron Microscopy (SEM) techniques were performed on polished material specimens for quantitative analysis of microstructural heterogeneities. A Carl-Ziess SEM with a SUPRA-40 field emission gun (FEG) source was used to record micrographs of secondary phase particles and voids in the undeformed material. An EDAX Energy Dispersive x-ray Spectroscopy (EDS) attachment was used to investigate the chemical composition of secondary phase particles. Electron BackScatter Diffraction (EBSD) was performed to investigate the grain orientation distribution for the ND, RD, and TD material directions. MTEX, a Matlab-based microstructural analysis toolbox, was used to process raw grain orientation data and produce pole figures for visualization of grain orientation distributions. Optical micrographs of the etched material samples were generated using a Carl-Ziess Axiovert-200 microscope for grain size analysis. Digital image correlation software, ImageJ (Abramoff *et al.* 2004), was used to quantify characteristics of interest for microstructural heterogeneities and grains from electron and optical micrographs, respectively.

2.2.2 Mechanical Testing

Mechanical deformation experiments were performed to determine the Al 7085-T711 alloy's performance under a variety of strain rates, stress states, and temperatures for a thorough calibration of the ISV plasticity-damage model. Quasi-static tension and compression experiments were performed using cylindrical specimens in an Instron 5882 frame with a 100kN load cell controlled by an Instron 25 mm extensometer. Low strain rate torsion experiments were performed using Lindholm (1967) thin-walled specimens in conjunction with a servo-hydraulic MTS 858 frame with a 25 N·m load cell. Quasi-static, elevated-temperature tension and compression tests were performed using an Instron environmental chamber in conjunction with the Instron 5882 frame and 25 mm extensometer. High strain rate Kolsky (1949) bar compression experiments were performed using cylindrical samples.

Quasi-static tension testing for model validation was performed by deforming a variety of notch Bridgman (1944) tension specimen geometries at 25 and 200°C. The samples were tested using an Instron 5882 frame with a 100 kN load cell. Elevated temperature experiments were performed at 200°C within an Instron environmental chamber. The gage section displacements were controlled and recorded using an Instron 25 mm extensometer. Each specimen was deformed at a nominal rate of 0.005 mm/s until fracture. The purpose of the notch Bridgman tension tests was to observe complex stress state deformation under a variety of environmental conditions to gauge the fidelity of the calibrated ISV plasticity-damage model for Al 7085-T711.

2.2.3 Fractographic Analysis

Fractographic analysis techniques were employed to characterize the Al 7085-T711 alloy failure modes and quantify the microstructural characteristics of the mechanically deformed specimens. Void morphology data from electron micrographs of fractured tension and torsional specimens was used to calibrate ISV parameters describing void nucleation, growth, and coalescence for the material. The fracture surfaces of the notched tension specimens were studied to assess the ability of the constitutive model to predict microstructural evolution during deformation.

2.2.4 Constitutive Modeling

An ISV model based upon the ISV plasticity-damage model (Bammann *et al.* 1993; Bammann *et al.* 1996) with the addition of ISVs to describe void nucleation, growth, and coalescence (Horstemeyer and Ghokale, 1999) was used describe the constitutive response of Al 7085-T711. The plasticity and damage parameters were calibrated using a material point simulator, DMGfit, and 1 mm³ Representative Volume Element (RVE) and material subroutine in Abaqus (Simulia, 2010), respectively. The ISV plasticity-damage model allows for the strain rate, stress state, and thermal dependence for isotropic and kinematic hardening plasticity mechanisms and void nucleation, growth, and coalescence-based damage evolution.

Validation of the ISV plasticity-damage model was performed via comparison of complex stress state deformation to experimental results. Notch Bridgman tensile

specimens of varying notch radii were deformed to fracture at a range of temperatures to validate the calibrated Al 7085-T711 ISV plasticity-damage model. A tabulation of the specimen geometries and testing conditions is given in Table 2.2. Varying notch root radii of 0.05 in. (1.27 mm), 0.10 in. (2.54 mm), and 0.15 in. (3.81 mm) (designated R50, R100, and R150, respectively) were tested to investigate triaxiality effects on damage evolution and failure. The R50, R100, and R150 notch root radii specimens correspond to notch root ratios (defined as the ratio of material cross section radius to notch radii, a/r) of 2.0, 1.0 and 0.67, respectively.

Table 2.2 Test matrix for notch Bridgman tension testing used for Internal State Variable (ISV) plasticity-damage model validation.

Specimen Type	Applied Velocity (mm/s)	Temperature (°C)	No. Experiments
R50	0.005	25	3
R50	0.005	200	3
R100	0.005	25	3
R100	0.005	200	3
R150	0.005	25	3
R150	0.005	200	3

Simulations of the specimen geometries and deformation conditions were performed using the Abaqus-Standard implicit solver (Simulia, 2010) in conjunction with the calibrated ISV plasticity-damage model user material subroutine. Part geometries were generated in accordance to the notch Bridgman tension specimen schematics shown in Fig. 2.1 and subsequently meshed in Abaqus CAE software using linear hexagonal, reduced integration (C3D8R) elements. The simulations feature quarter symmetry notched tension specimens subjected to an applied velocity on the specimen grip of 0.005 mm/s as shown in Fig. 2.2.

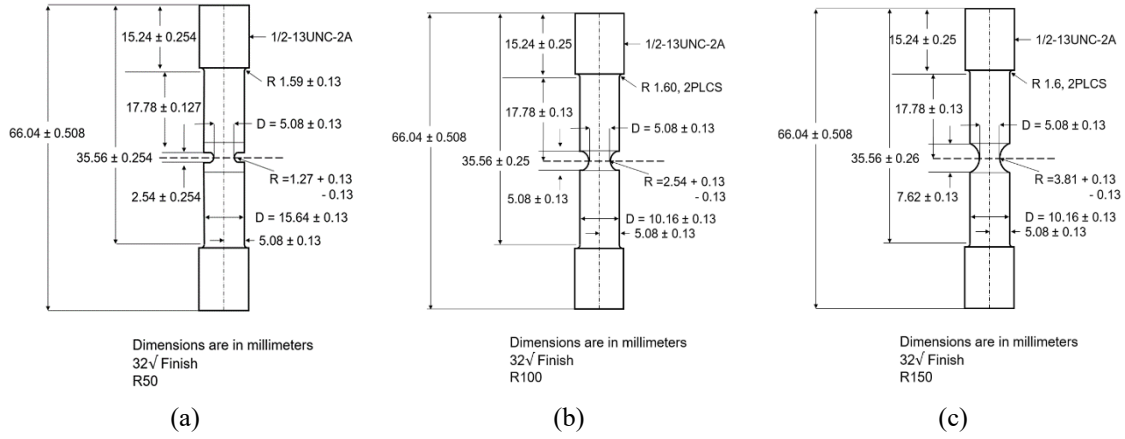


Figure 2.1 Specimen schematics for notch Bridgman tension specimens.

(a) R50, (b) R100, and (c) R150 specimens.

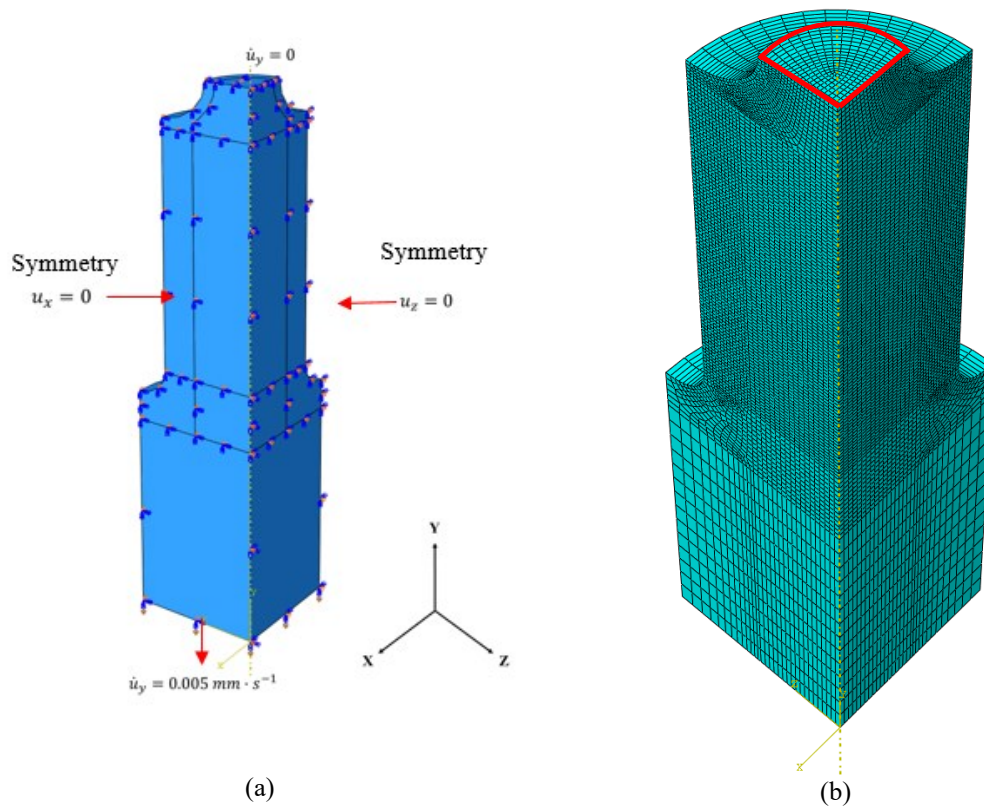


Figure 2.2 Finite element simulation geometry of Bridgman notched tension specimen.

- (a) Finite element simulation boundary conditions.
- (b) Finite element simulation mesh.

2.2.5 Uncertainty Quantification of Experimentally Measured Data

Experimental investigations are inherently fraught with systematic and random sources of error that contribute to uncertainty in the measurements of quantities of interest. This study accounted for uncertainty by proper identification of the type of distribution of experimental datasets (microstructure properties and stress-strain data) and calculation of the 95% confidence intervals about mean values for experimental data using methods described by Coleman and Steele (2009).

2.3 Results and Discussion

2.3.1 Al 7085-T711 Chemical and Microstructural Properties

Initial microstructural analysis efforts sought to identify bulk and site-specific material chemistries, to quantify microstructural heterogeneity characteristics, and to quantify grain size and orientation distributions. The bulk chemical composition shown in Table 2.1 revealed significant quantities of alloying elements Zn, Mg, and Cu, consistent with 7XXX class aluminum alloys. EDS techniques were employed to identify chemistries of microstructural heterogeneities. Figure 2.3 shows the elemental distributions around a cluster of secondary phase particles (Fig 2.3-A). Figures 2.3B-C demonstrate a lack of the primary alloying elements (Al, Zn, Mg) at the secondary phase particle sites. The secondary phase particles have been identified as intermetallic Cu-Fe compositions (Fig. 2.3E-F).

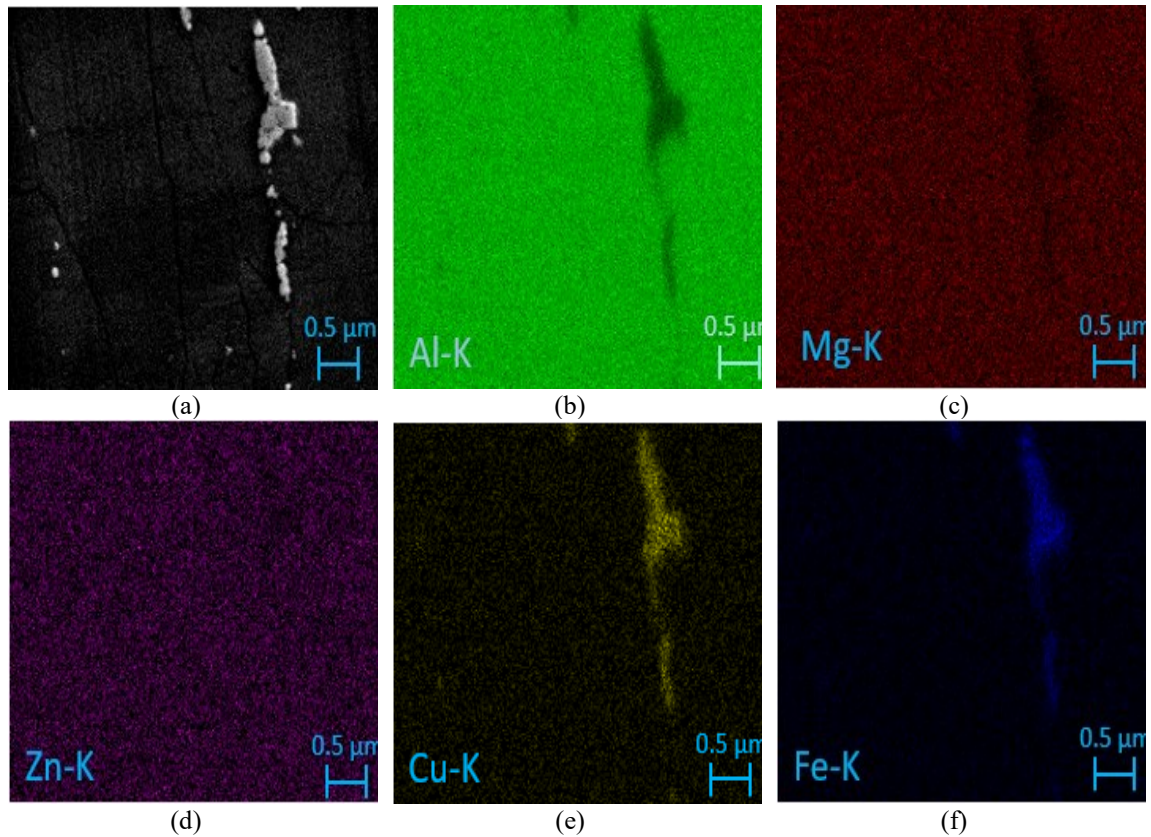


Figure 2.3 Elemental distribution mappings acquired from an Energy Dispersive x-ray Spectroscopy (EDS) scan of the Normal Direction (ND).

- (a) Electron micrograph of particle cluster region.
- (b) EDS map of aluminum distribution.
- (c) EDS map of magnesium distribution.
- (d) EDS map of zinc distribution.
- (e) EDS map of copper distribution.
- (f) EDS map of iron distribution.

The presence of microscopic voids and secondary phase particles was of interest in this study because of their propensity to cause localized stress concentrations and thus serve as nucleation sites for damage within the material. Additionally, secondary phase particles may produce dislocation pileups and contribute to the material's work hardening. In general, voids were detected near clusters of FeCu secondary phase particles, as

demonstrated in Fig. 2.4. The presence of voids could be a result of particle-matrix decohesion during the rolling process. ImageJ software was used to quantify the mean void and particle diameter (assumed to be spherical), number density, and area fraction from electron micrographs. The ninety-five percent confidence interval (CI_{95}) about mean property values was determined using methods described by Coleman and Steele (2009). The results of the quantification are included in Tables 2.3-4. The pre-existing voids appeared on average smaller and more numerous in the RD plane ($1.1 \mu\text{m}$ and 800 voids/mm^2) compared to the ND ($1.5 \mu\text{m}$ and 110 voids/mm^2) and TD planes ($1.2 \mu\text{m}^2$ and 120 voids/mm^2). The differences could be attributed to the smaller grain sizes measured in the RD plane relative to the ND and TD planes (discussed in the following section), whereby a greater number density of grain boundaries exist for potential void nucleation sites. Particles in the as-received material appeared smaller in the ND plane ($1.2 \mu\text{m}^2$) compared to those observed in the RD and TD planes (1.6 and $1.4 \mu\text{m}^2$, respectively). Conversely, the particle number density was significantly greater in the ND plane ($1930 \text{ particles/mm}^2$) relative to the RD and TD planes (1050 and $1110 \text{ particles/mm}^2$, respectively). The total area fraction of particles in each plane was similar (0.20 , 0.23 and 0.23% for particles observed in the ND, RD, and TD planes). The anisotropy in particle size and number density distribution is likely attributable to the rolling process, which causes expansion of grains in the RD and TD direction. The expansion of grains limits the potential for elongation of particles in the RD and TD directions (ND plane) but provides long grain boundaries (potential precipitation sites), hence the greater number density.

Table 2.3 Initial CuFe secondary phase particle property distributions in an aluminum 7085-T711 alloy.

Plane	Particle Diameter (μm)		NND (μm)		Area Fraction (%)		Number Density ($1/\text{mm}^2$)	
	Mean	CI ₉₅	Mean	CI ₉₅	Mean	CI ₉₅	Mean	CI ₉₅
ND	1.165	-0.108 +0.121	3.935	-0.192 +0.213	0.196	± 0.0832	1933.514	± 363.241
TD	1.632	-0.549 +0.612	12.544	-1.027 +1.228	0.233	± 0.03	1115.896	± 90.656
RD	1.373	-0.141 +0.162	6.628	-0.427 +0.490	0.231	± 0.0652	1053.247	± 246.935
Average	1.390	± 0.298	7.702	± 0.644	0.220	± 0.0595	1367.552	± 233.612

Table 2.4 Initial porosity property distributions in an aluminum 7085-T711 alloy.

Plane	Pore Diameter (μm)		NND (μm)		Area Fraction (%)		Number Density ($1/\text{mm}^2$)	
	Mean	CI ₉₅	Mean	CI ₉₅	Mean	CI ₉₅	Mean	CI ₉₅
ND	1.519	-0.230 +0.308	37.595	-4.758 +6.370	0.020	± 0.00351	113.177	± 17.673
RD	1.107	-0.084 +0.101	12.679	-1.047 +1.254	0.073	± 0.0272	803.553	± 256.917
TD	1.216	-0.161 +0.222	45.264	-6.244 +8.624	0.031	± 0.00276	118.107	± 21.422
Average	1.279	± 0.093	24.386	± 1.807	0.033	± 0.00811	269.264	± 66.397

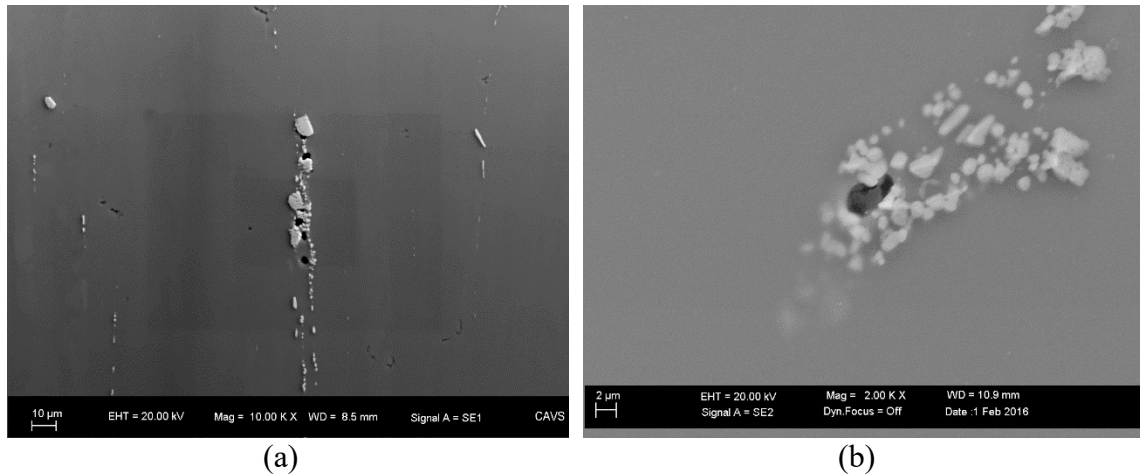


Figure 2.4 Micrographs of FeCu secondary phase particle clusters.

- (a) Transverse Direction (TD) material plane.
- (b) Normal Direction (ND) material plane.

Secondary phase particle size and volume fraction characteristics have been shown to influence the rate of void nucleation (Gangulee and Gurland, 1967) and are accounted for in the particle size, d , and particle volume fraction, f , material property parameters within the void nucleation rate equation shown in Eq. (2.9). Similarly, McClintock (1968) and Cocks and Ashby (1982) demonstrate the influence of void size and volume fraction on void growth rates. These phenomena are considered in the pore and void growth rates (Eqs. 2.8 and 2.10, respectively) through the initial void radius R_0 and the initial pore volume fraction ϕ_{pore} terms, respectively. Experimental studies (Brown and Embury, 1973; Goods and Brown, 1979) have demonstrated that sufficiently closely spaced voids can interact and coalesce by sheeting and impingement mechanisms. Therefore, the pre-existing pore and secondary phase particle nearest neighbor distances are quantified for use

in the calibration of the void coalescence parameter, NND , shown in Eq. (2.11). The average secondary phase particle and pre-existing void properties are used for model material constants because the ISV model assumes ideal spherical shapes for heterogeneities.

Grain size data for the Aluminum 7085-T711 material was obtained via an Axiovert 200M Optical Microscope. Figures 2.5A-D demonstrate the dimensional anisotropy of the grains in the ND, RD, and TD planes. Grains imaged in the ND material plane appear qualitatively larger than the size of grains imaged in RD and TD planes. The rolling process elongates grains (especially in the RD direction) and flattens grains in the ND direction. ImageJ software was used to quantify the average grain area for each material direction. The average grain area for the aggregate material was calculated in accordance with ASTM standard E 1382-97 (ASTM, 1997):

$$\bar{A} = (A_{ND}A_{RD}A_{TD})^{1/3}, \quad (2.12)$$

where A_{ND} , A_{RD} , and A_{TD} are the average grain areas in the ND, RD, and TD planes, respectively. The average grain area calculated from Eq. (2.12) were used to determine the grain size parameter,

$$G = -3.3223 \log \bar{A} - 2.955. \quad (2.13)$$

In Eq. (2.13), GS is the grain size parameter computed in accordance with ASTM standard E 1382-97 (ASTM,1997). The mean grain area (A_{ND} , A_{RD} , and A_{TD}), geometric mean of the grain area (\bar{A}), and size parameter (GS) values are included in Table 2.5. In general, the average grain area in the ND plane ($530 \mu\text{m}^2$) was twice the average grain

areas in the RD and TD planes (230 and 180 μm^2 , respectively). The rolling process induced expansion of the grain dimensions in the ND plane (RD and TD directions) and compression in the ND direction.

Table 2.5 Grain structure properties of an aluminum 7085-T711 alloy.

Plane	Grain Area (μm^2)		Grain Diameter (μm)		ASTM Grain Size Parameter	
	Mean	CI ₉₅	Mean	CI ₉₅	Mean	CI ₉₅
ND	526.682	-26.066 +28.930	22.950	-1.136 +1.261		
TD	231.911	-16.017 +18.583	15.229	-1.052 +1.220		
RD	182.395	-13.410 +15.722	13.505	-0.993 +1.164		
Average	281.381	± 20.370	16.774	± 1.214	8.842	± 0.101

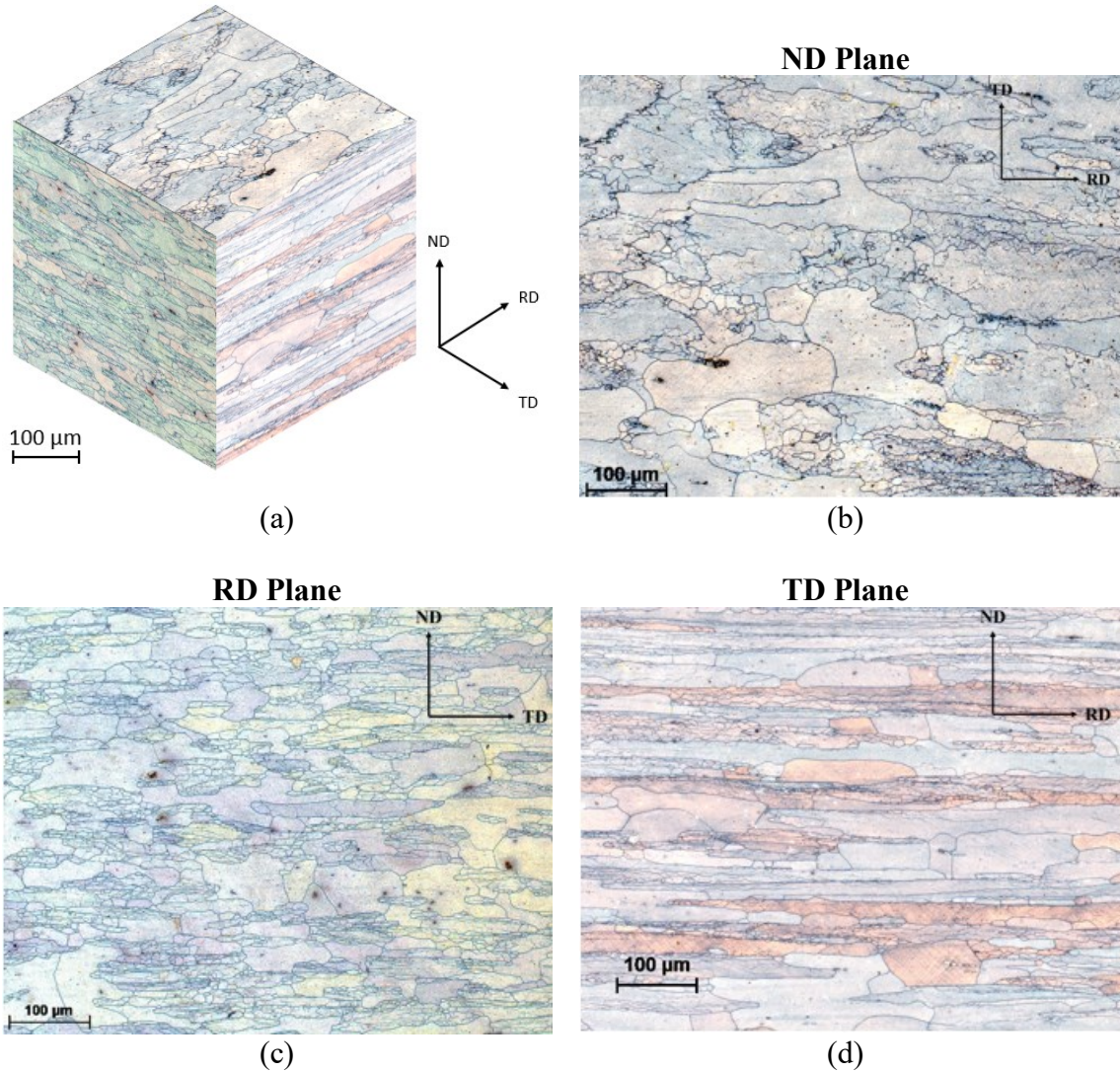


Figure 2.5 Micrographs of aluminum 7085-T711 grain structure.

- (a) Stereographic projection of grain structure.
- (b) Normal Direction (ND) material plane.
- (c) Rolled Direction (RD) material plane.
- (d) Transverse Direction (TD) material plane.

EBSD was performed on ND, RD, and TD planar specimens of the face centered cubic (FCC) Aluminum 7085-T711 alloy to study the grain orientation anisotropy due to the material's rolling process history. A highly anisotropic (textured) distribution of grain orientations with respect the primary rolling directions (ND, RD, and TD) could cause the dominant slip system of the aggregate material to depend on the global loading direction and, thus, introduce directional dependence on the material's macroscale stress-strain response. In the case of a highly textured material, a single calibration of the ISV plasticity-damage model may be insufficient for accurate simulation of complex deformations. Alternate approaches include calibration of separate ISV models for the ND, RD, and TD directions (Jordon *et al.* 2009) or simulation of the processing of virgin material to develop ISV parameter histories (Cho, 2015).

Regional EBSD scans of the specimen surfaces were performed using a FEG-SEM in conjunction with OIM acquisition software. The inverse pole figure in Fig. 2.6 for the RD plane was generated using an OIM Analysis software suite. The inverse pole figure in Fig. 2.6 shows the directional orientation of the material's grains with respect to the primary cubic ([100], [110], and [111]) lattice directions. Inverse pole figure data in the RD planes in Fig. 2.6 appears to show a dominant distribution of grain orientations between the [001] and [111] directions (denoted by hues between red and blue).

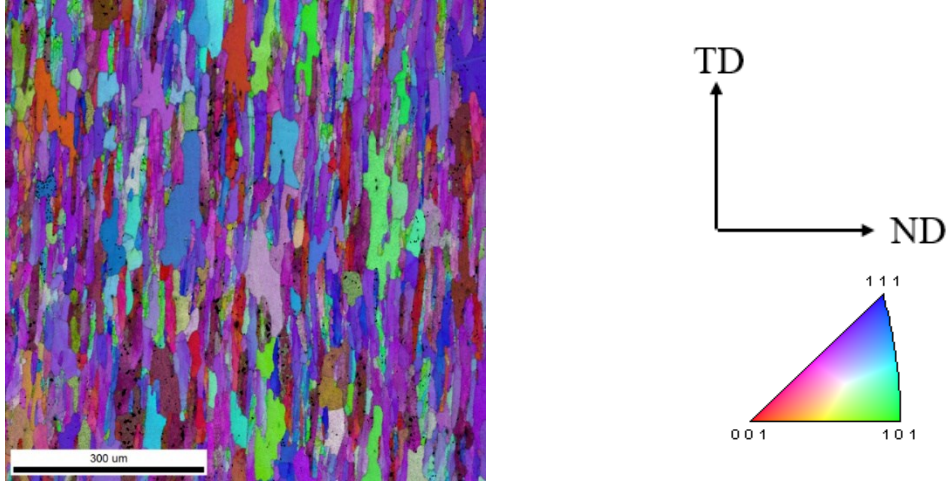


Figure 2.6 Inverse pole figures for the RD planar surface of a rolled aluminum 7085-T711 material.

Orientation distribution data from EBSD scans was imported into MTEX software to perform a quantitative assessment of the grain orientations in the RD plane of the rolled Aluminum 7085-T711 material. The pole figures shown in Fig. 2.7 show the relative statistical distribution of grain orientations with respect to cubic planes of interest by means of Multiples of Random Distribution (MRD) values. Red regions indicate relative high densities (poles) of a corresponding grain orientation, while white regions indicate an absence of orientations. The pole figures show symmetry in the grain orientation distributions about the [100], [110] and [111] cubic directions in the RD plane, indicative of an isotropic distribution of grain orientations. Additionally, a low magnitude pole (MRD of 2.4) was detected on the [211] direction. The magnitude of the observed MRD poles in this study (ranging from 2-4) are low relative to highly textured aluminum materials in the literature (e.g., MRD values of 10.0 reported in Lopes *et al.* 2003 and 9.0 in Bhattacharyya *et al.* 2017). Rolling processes can produce an acute degree of texturing. The 7085

material's solution hardening heat treatment (T711), however, like resulted in a non-preferential distribution of grain orientations. The essentially isotropic distribution of grain orientations is a factor contributing to the lack of directionally-based anisotropy in the mechanical response discussed in the following section.

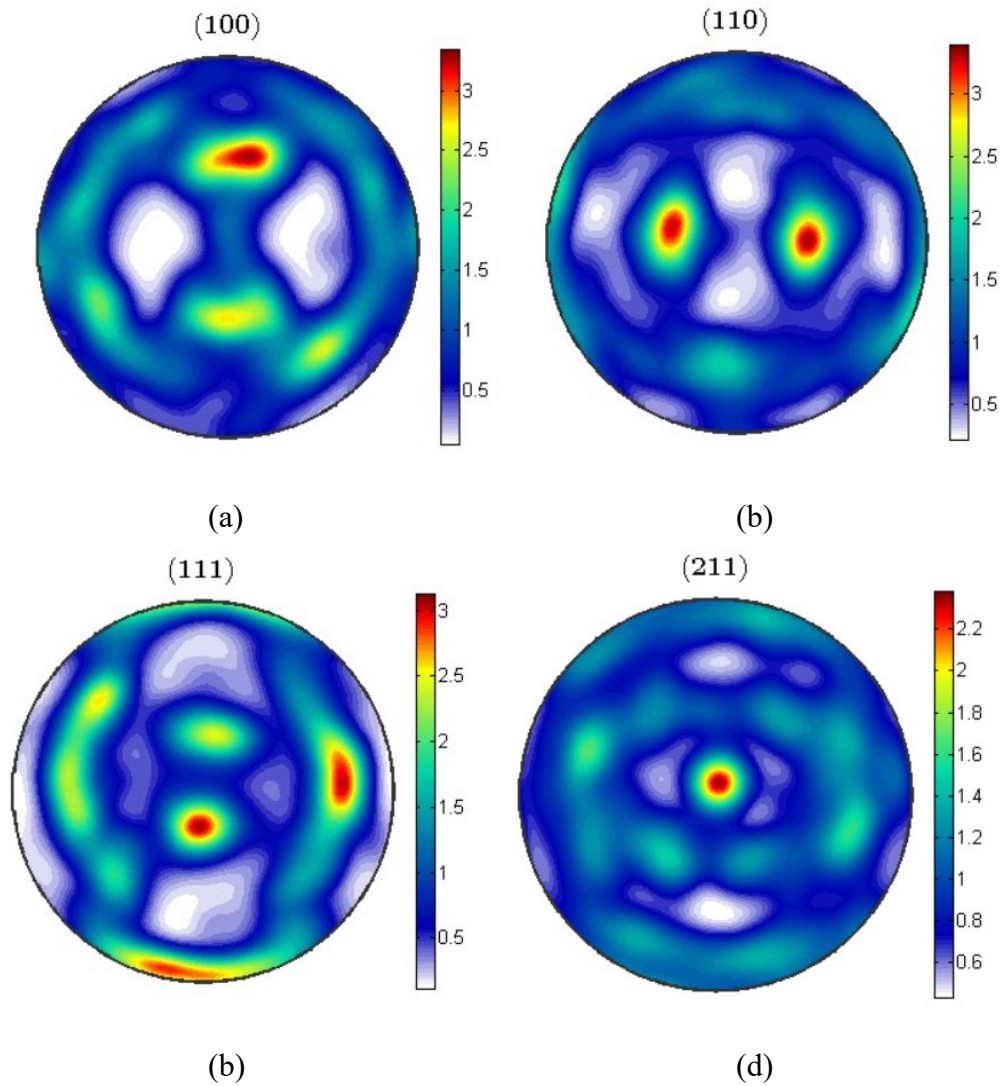
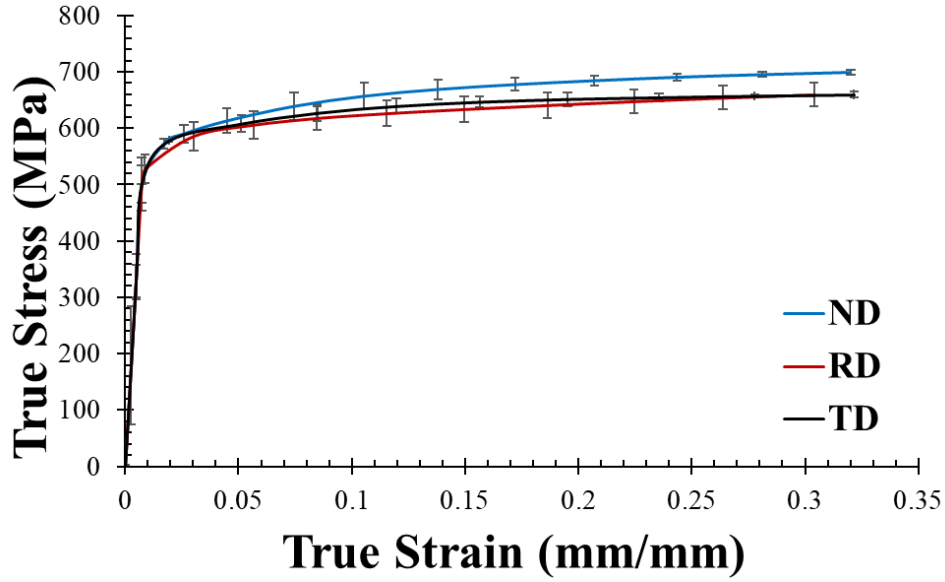


Figure 2.7 Pole figures of grain orientation distributions for an Al 7085-T711 alloy.

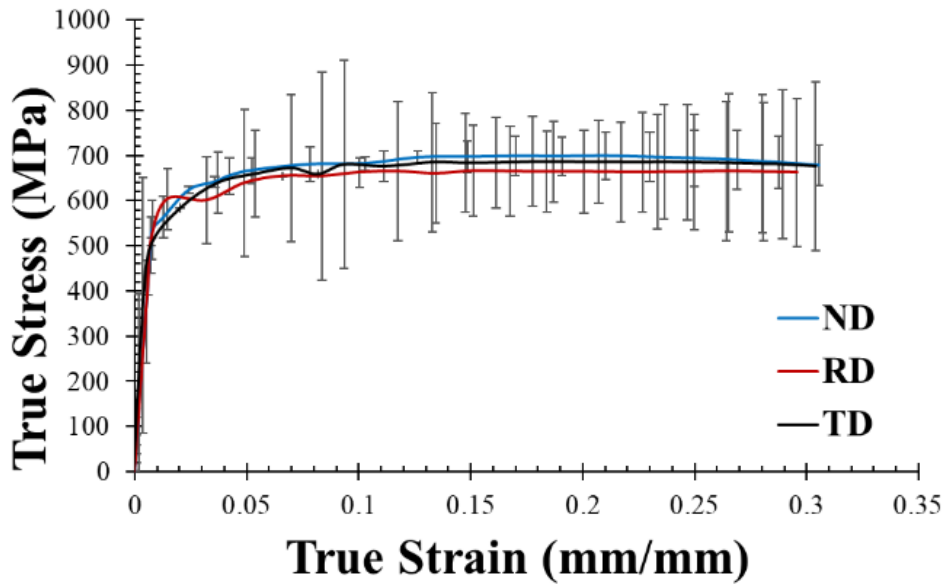
(a) (100) plane; (b) 110 plane; (c) (111) plane; (d) (211) plane.

2.3.2 Mechanical Testing, Fractography, and ISV Model Calibration

Simple compression, tension, and pure torsion tests were performed for ISV plasticity-damage model calibration. A minimum of three experiments were performed at each condition to compute mean stress values for each condition. The ninety-five percent confidence interval about the mean stress was determined using methods discussed in Coleman and Steele (2009). Ambient temperature compression experiments at 0.001 and 1,000 s⁻¹ for the primary material orientations show little directionally-based anisotropy of mechanical behavior in the material (Fig. 2.8). Because compression showed little deformation induced anisotropy, tensile and shearing deformations would also exhibit minimal mechanical anisotropy due to the lack of grain orientation anisotropy and symmetric nature of the FCC lattice. Therefore, all subsequent mechanical testing was performed in the RD direction. The mechanical performance of the alloy was assessed for a variety of stress states, strain rates, and temperatures.



(a)



(b)

Figure 2.8 Comparison of compressive mechanical responses (generated: Bhattacharyya *et al.* 2017) of Normal Direction (ND), Rolling Direction (RD), and Transverse Direction (TD).

(a) Applied strain rate of 0.001 s^{-1} .

(b) Applied strain rate of 1000 s^{-1} .

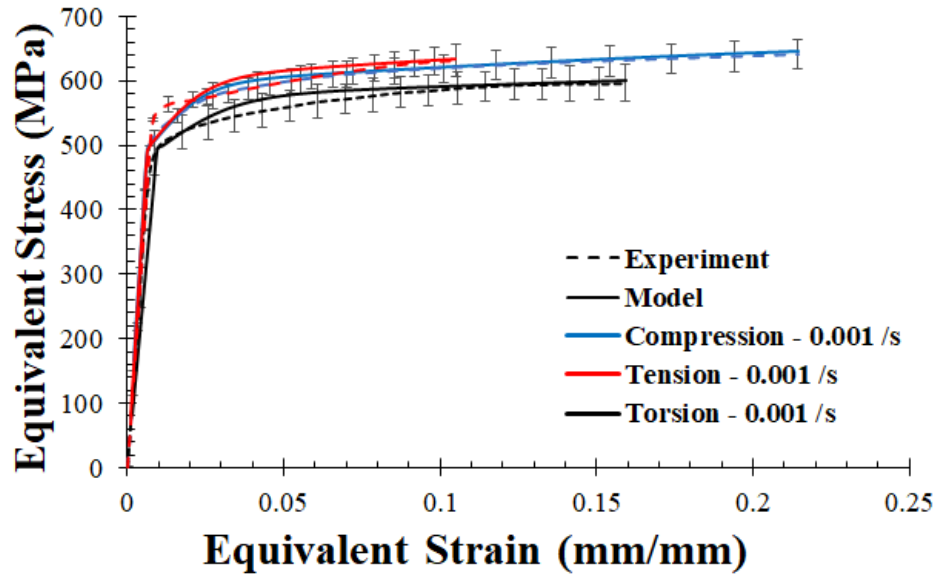
The plasticity and damage model evolution parameters were calibrated using a material point simulator model, DMGfit, and a Representative Volume Element (RVE) simulation in Abaqus (Simulia, 2010), respectively. The calibrated plasticity and damage model parameters are listed in Table 2.6. Figure 2.9 compares experimental and ISV model calibration stress-strain curves for a variety of strain rates, stress states, and temperatures. Quasi-static (0.001s^{-1}), ambient temperature tension tests show yield and ultimate strengths of approximately 500 MPa and 630 MPa, respectively. Ambient temperature stress state dependent tests performed at 0.001s^{-1} revealed minimal differences between tension and compression but showed torsional softening of the yield strength by roughly 30 MPa (6% lower). The Al 7085-T711 alloy exhibited a 50 MPa increase in yield strength as the strain rate increased from 0.001 s^{-1} to $1,000\text{ s}^{-1}$. However, there is negligible change to the material's hardening rate over the observed strain rate range. Quasi-static (0.001s^{-1}) compression tests performed at ambient, 100°C , and 200°C revealed significant thermal softening effects attributable to increased dislocation mobility at elevated temperatures. The alloy exhibits a nearly 150 MPa reduction in yield strength and reduction of the hardening rate as the temperature increased from ambient temperature to 200°C . Fig. 2.9 demonstrates that the calibrated ISV plasticity-damage model for Al 7085-T711 accurately captures the strain rate, stress state, and thermal characteristics of the alloy's mechanical behavior.

Table 2.6 Internal state variable model coefficients for (a) plasticity and (b) damage.

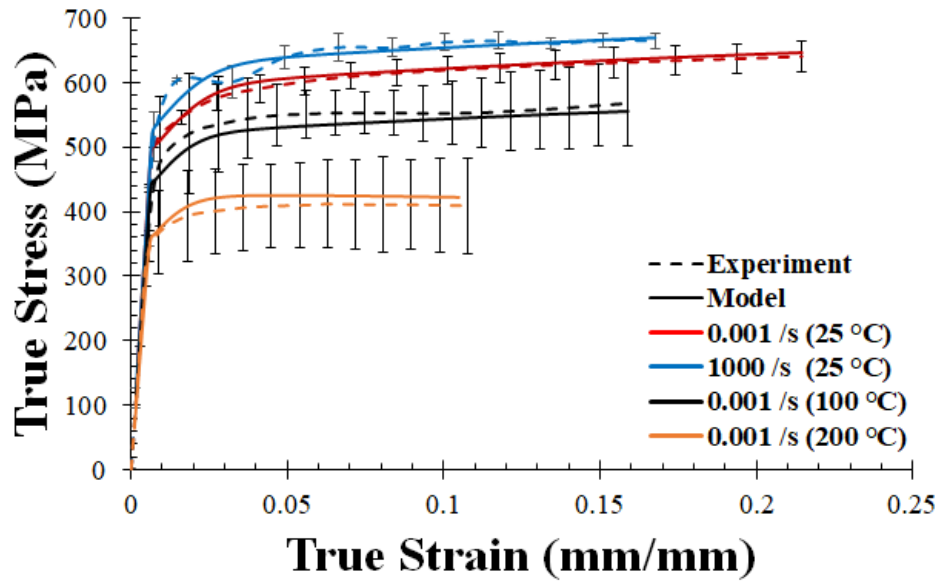
Aluminum 7085-T711	Constants	Values	Aluminum 7085-T711	Constants	Values
Elasticity constants	G (MPa)	26920	McClintock void growth	Void growth exp. (n)	-0.12
	a	0		Initial Rad (R ₀)	0.00055
	K (MPa)	58330		B _{void}	8.0
	b	0		K _{void}	26.0
	Melt temp (K)	900		a	5800
Strain rate and temperature dependent yield constants	C1 (MPa)	47.2167	Void nucleation	b	0
	C2 (K)	0		c	285
	C3 (MPa)	398.06		Nuc. Coef.	1300
	C4 (K)	62.7368		Fract. Toughness (MPa√mm)	790
	C5 (1/MPa)	1305.46		Part.size (mm)	0.0013
Kinematic hardening and recovery terms	C6(K)	0	Void Coalescence	Part .vol. fract	0.0022
	C7 (1/MPa)	0.0145		cd1	0.01
	C8 (K)	0		cd2	8.0
	C9 (MPa)	995.87		GS ₀ (mm)	0.01
	C10 (K)	1.256		GS (mm)	0.01
	C11 (s/MPa)	0		GS exp,Zz	1.0
Isotropic hardening and recovery terms	C12 (K)	0	Nearest neighbor dist. (mm)		0.01
	C13 (1/MPa)	4.61		Init. void vol. fract.	0.00033
	C14 (K)	564.436		NTD Nuc. Temp. depend.	-1050
	C15 (MPa)	4911.82		CTD Coal. Temp. depend.	0.0025
Long range temperature dependent yield	C16 (K)	0	McClintock Growth	CTv Growth Temp. depend.	-0.0013
	C17(s/MPa)	0			
Hardening and recovery	C18 (K)	0			
	C19 (K)	0.00999718			
Temperature	C20 (K)	526.755			
	Ca	-2.0			
	Cb	0.12			
	Init.temp (K)	293			
	Heat gen.coeff	0.34			

(a)

(b)



(a)



(b)

Figure 2.9 Calibration of Al 7085-T711 ISV plasticity model for varying strain rate, stress state, and temperature.

(a) Calibration of Al 7085-T711 ISV model for varying stress states.

(b) Calibration of Al 7085-T711 ISV model for varying strain rate and temperature.

Micrographs of fractured tension and torsion surfaces were acquired via SEM for quantification of void properties at rupture. Compression samples tested beyond 50% true strain did not fracture for a broad range of strain rates ($0.001\text{--}1000\text{s}^{-1}$) and temperatures ($25\text{--}200^\circ\text{C}$). Therefore, compression samples were omitted from fractographic investigations. Figures 2.10 and 2.11 show the fracture characteristics of Al 7085-T711 under tension and torsion at 0.001 s^{-1} strain rate. Tension specimens exhibited significant void evolution around the center of the specimen cross section (and corresponding flat fracture) where stress triaxiality was the greatest (Fig. 2.10-B). Many voids were shown to form around secondary phase particles. Slant fracture occurred near the specimen edges due to shear localization (Fig. 2.10-C). For torsional deformation, rupture was shown to initiate via void evolution before transitioning to a shear dominated cleavage fracture in the specimen's circumferential direction (Fig. 2.11). A table of the fracture characteristics of specimens deformed in tension and torsion at a variety of strain rates and temperatures is included in Table 2.7. Experimental fracture data was quantified using the average fracture strain and void properties (number density, size, and area fraction) for a minimum of three experiments per test condition.

Table 2.7 Void characteristics at fracture for strain rate, stress state, and temperature.

Temperature (°C)	Strain Rate (s ⁻¹)	Stress State	Void Radius (µm)		NND (µm)		Area Fraction (%)		Number Density (1/mm ²)	
			Mean	CI ₉₅	Mean	CI ₉₅	Mean	CI ₉₅	Mean	CI ₉₅
25	0.001	Tension	2.584	-0.463 +0.478	5.344	-0.161 +0.166	20.169	±2.738	9689.579	±1584.622
25	0.01	Tension	2.034	-0.340 +0.350	4.534	-0.067 +0.068	18.087	±2.031	13905.413	±1434.498
200	0.001	Tension	7.152	-0.977 +0.996	10.358	-0.127 +0.128	32.765	±3.471	2038.763	±236.218
25	0.001	Torsion	1.833	-0.306 +0.315	3.115	-0.058 +0.059	20.803	±2.802	19714.684	±3452.669

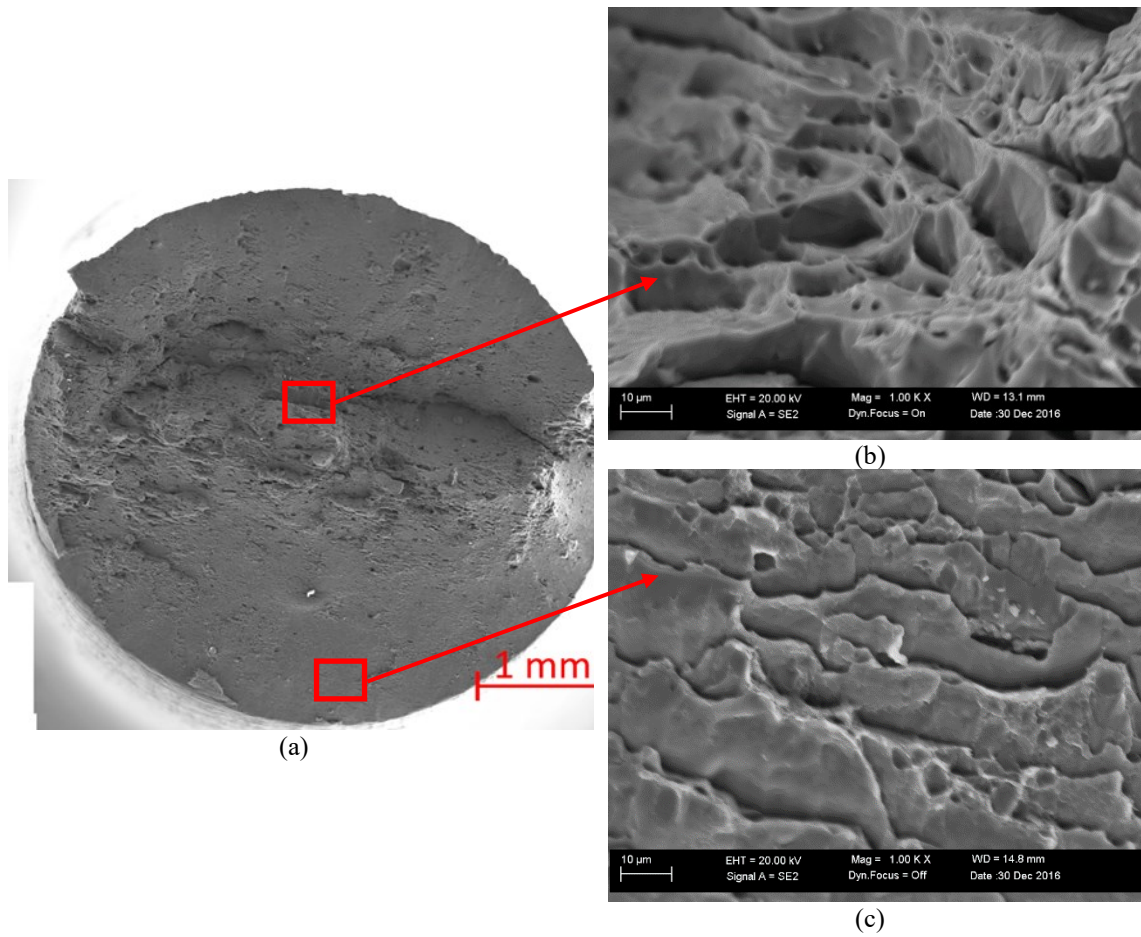


Figure 2.10 Electron micrographs of fracture surface of uniaxial tension specimen deformed at 0.001 s^{-1} and 25°C .

- (a) Fracture surface micrograph.
- (b) Central region exhibiting ellipsoidal voids due to triaxiality.
- (c) Edge regions exhibiting shear dominated fracture.

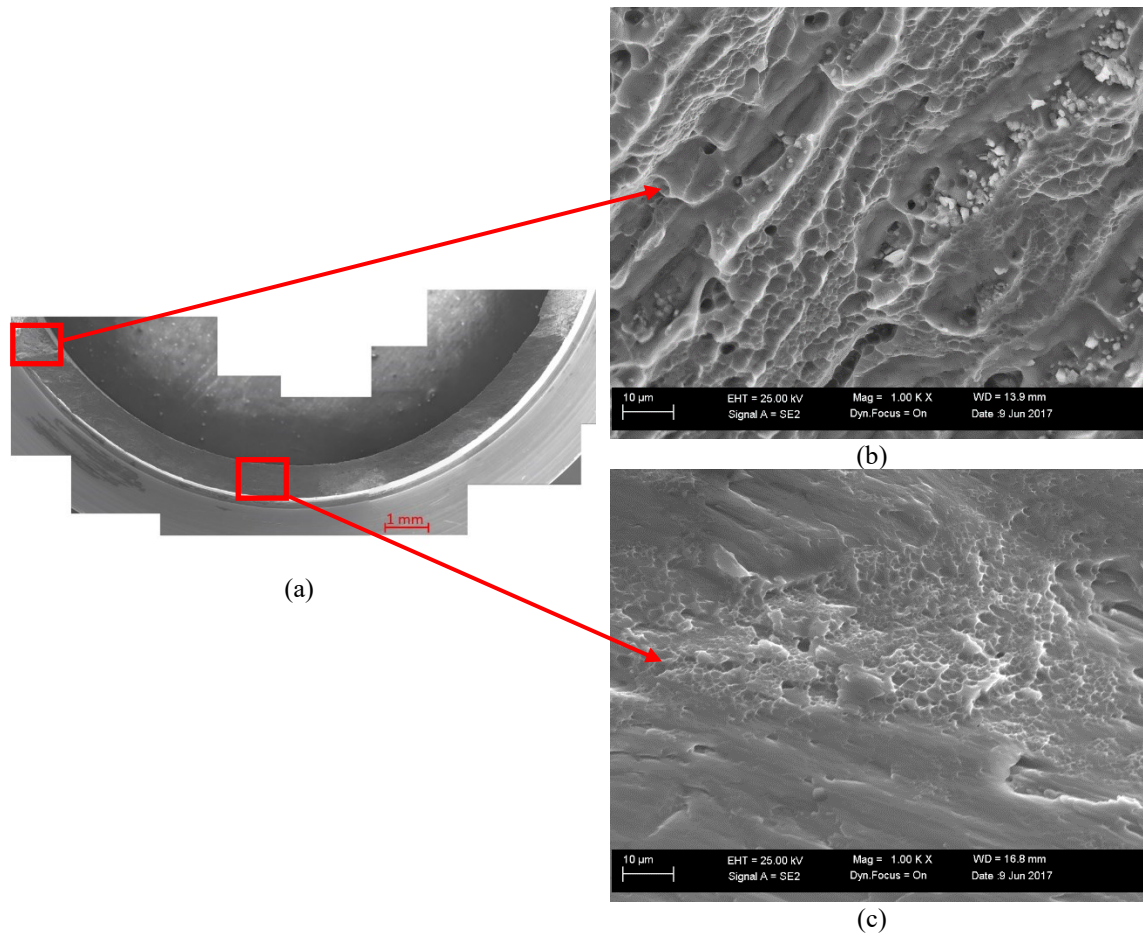


Figure 2.11 Torsional fracture specimen deformed at $0.001s^{-1}$ strain-rate and $25^{\circ}C$ temperature.

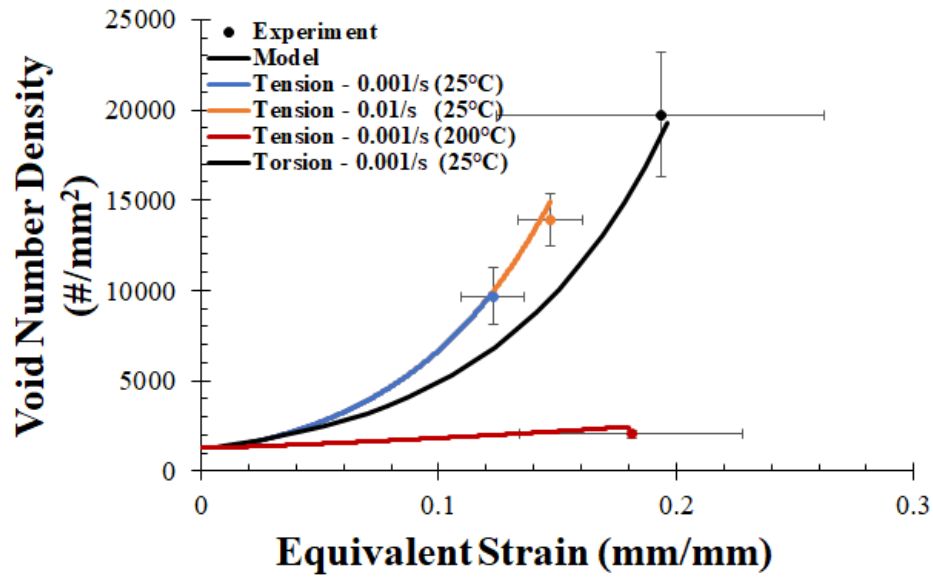
- (a) Fracture surface micrograph
- (b) Damage initiation region featuring significant void nucleation.
- (c) Damage propagation dominated by planar shear fracture.

Generally, voids nucleated in tension were larger than those nucleated in torsion due to higher stress triaxiality. Table 2.7 shows approximate average void areas of $21 \mu\text{m}^2$ to $11 \mu\text{m}^2$ for ambient temperature, quasi-static tests in tension and torsion, respectively. However, the average void number density on the torsional specimen fracture surfaces ($\sim 20,000$ voids/ mm^2) was nearly double that for tensile fracture surfaces ($\sim 10,000$ voids/ mm^2) for similar strain rates and temperatures. The average void area fractions measured from the tension (21%) and torsion (20%) samples were very similar.

A comparison of the data in Table 2.7 reveals significant differences in fracture characteristics for tension samples deformed at ambient and 200°C temperatures. In general, the average void size increased dramatically with increasing temperature. For example, the average void size at 200°C ($160 \mu\text{m}^2$) was nearly eightfold greater than for the material deformed ambient temperature ($21 \mu\text{m}^2$). However, the average void number density drastically decreased from $10,000$ voids/ mm^2 at ambient testing conditions to 2000 voids/ mm^2 at 200°C . The material exhibited significantly higher average void area fraction due to tension at 200°C (32%) versus ambient temperature (20%). This suggests that as temperature increases, void growth and coalescence modes become dominant, which is consistent with the findings of Horstemeyer and Ramaswamy (2000) that show a high correlation between increasing temperatures and void growth rates.

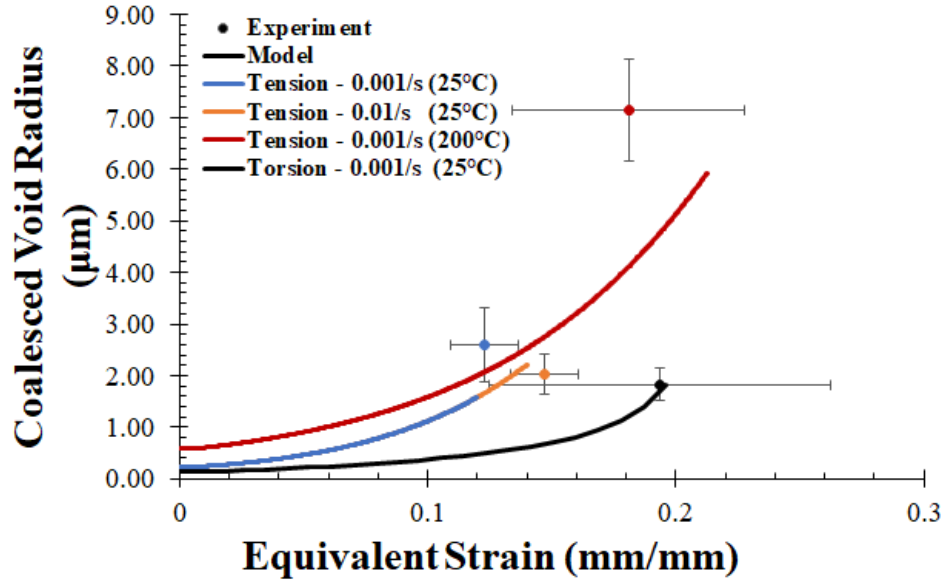
The damage ISVs were calibrated using a 1 mm^3 RVE simulation in Abaqus in conjunction with a ISV model user material subroutine. The void number density, size, and area fraction quantified from fracture surface micrographs were used for ISV damage model calibration. Figure 2.12 shows the predicted and measured void number density,

coalesced void radii, and void area fraction as a function of equivalent strain for tension and torsion experiments performed at two strain rates (0.001 and 0.01/s) and temperatures (25 and 200°C). The ISV model captured the drastic decrease in nucleation rate for increasing temperatures Fig. 2.12A in agreement with Dighe *et al.* (1998). Similarly, the model captured the decrease in nucleation rate from tension to torsion for similar magnitudes of equivalent strain.

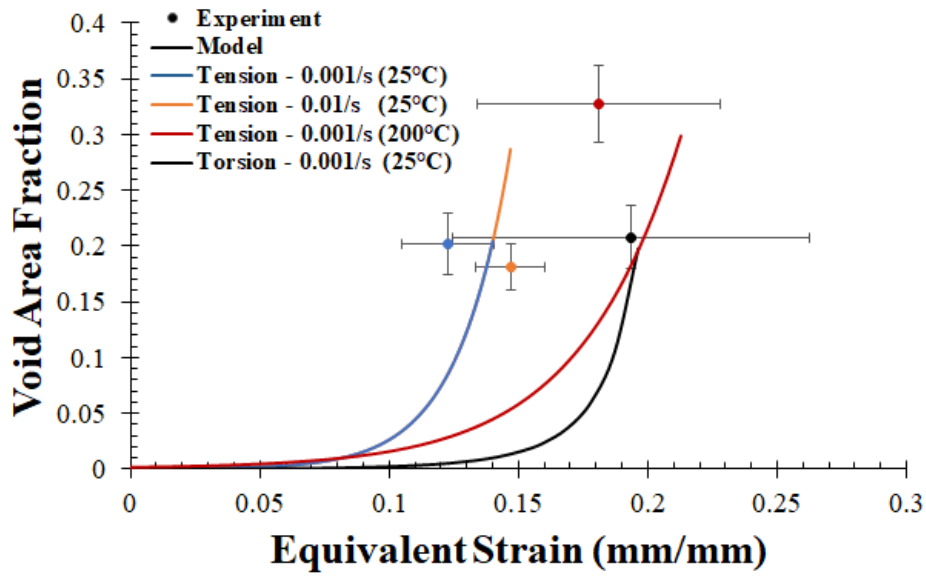


(a)

Figure 2.12 The Internal State Variable (ISV) damage model calibration for Al 7085-T711 for varying strain rates, stress states, and temperatures.



(b)



(c)

Figure 2.12 (continued)

- (a) Calibration of void nucleation.
- (b) Calibration of product of void growth and coalescence.
- (c) Comparison of experimental and model predicted void volume fraction evolution.

During the quantitative fractography process, coalesced voids can be indistinguishable from the original voids, therefore the coalesced void radius (the product of the void radius and the void coalescence) was used for damage model calibration (Horstemeyer *et al.* 2000A). The calibration results for the coalesced void radius are included in Fig 2.12-B. The ISV void growth model herein does not capture strain rate sensitivity as Fig. 2.12-B shows the model predicts the same void growth rate for tensile deformations at 0.001 and 0.01 s⁻¹. However, for each test condition, the model prediction for coalesced void radius evolution was bounded by the uncertainty bands associated with the respective condition's experimentally measured average size and fracture strain. The ISV model predicts the reduction in void growth rate due to torsion relative to tension for similar equivalent strains (Fig. 2.12-B). The calibrated ISV model tends to underpredict the void growth rate of the 200°C tension sample. Nevertheless, the resulting ISV model predictions for void area fraction (damage) evolution exhibited reasonable agreement with the respective experimental data (Fig. 2.12-C). The ISV model prediction for void area fraction evolution was bounded by the uncertainty bands for experimental final void area fraction and fracture strain for each test. Figure 2.12-C shows that the damage evolution was greatest in tension; this is attributable to the stress triaxiality (Waters *et al.* 2000). In contrast, measured and predicted porosity evolution was lowest for fractured torsion specimens. Increasing the deformation temperature reduced the rate of void area fraction evolution and caused the material to reach greater strains at failure. Increased dislocation mobility at greater temperatures likely allowed for increased rates of dislocation annihilation and vacancy occupation thus reducing the rate of void nucleation and growth.

At low temperatures, where void nucleation dominates, materials may experience more crack-like damage evolution than at elevated temperatures where void growth and coalescence are significant. Figure 2.12-C demonstrates that the increase in ductility with temperature allowed the material deformed at 200°C to develop nearly 50% greater void area fraction than the materials deformed at ambient temperatures (approximately 32% to 21% porosity at 200°C and 25°C, respectively).

2.3.3 ISV Model Validation

Abaqus FEA simulations of deformation of 0.05 in. (1.27 mm), 0.10 in. (2.54 mm), and 0.15 in. (3.81 mm) notch radius Bridgman tension specimens (R50, R100, and R150, respectively) were performed to validate the Al 7085-T711 ISV model. A mesh convergence study was performed using the R100 specimen geometry and peak load and extension to failure as convergence metrics for determining suitable mesh densities. Fig. 2.13 shows the convergence of both peak load and failure extension is achieved for meshes exceeding 50,000 linear hexahedral elements. Due to similarity in geometry, each specimen geometry (R50, R100, and R150) was meshed with at least 60,000 linear hexahedral elements to ensure solution convergence and minimize computational expense.

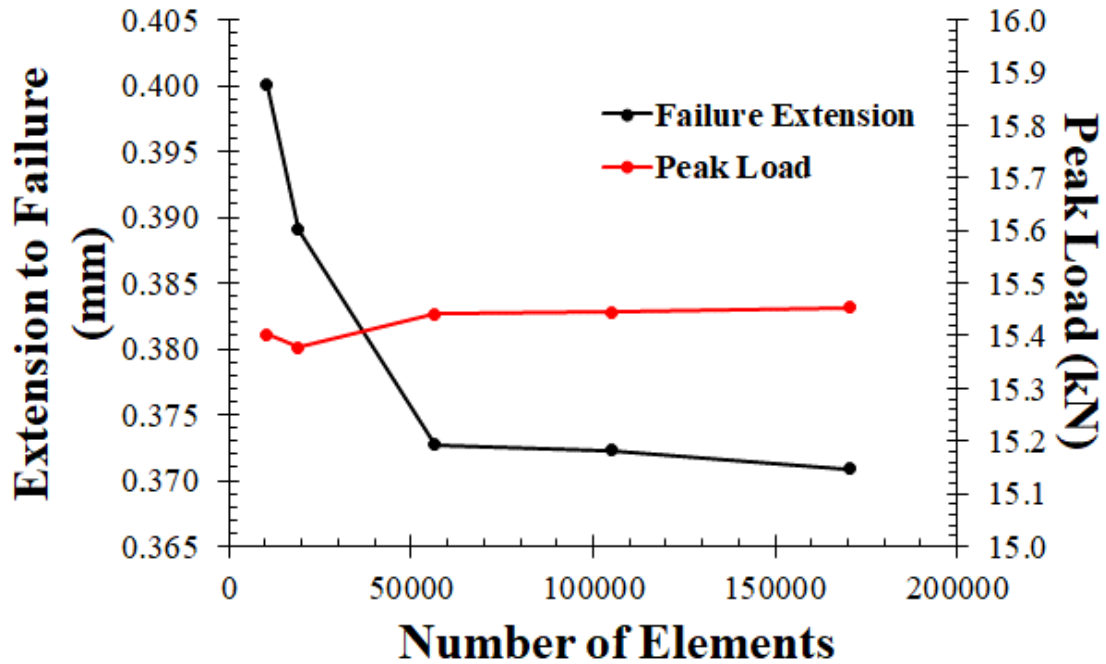


Figure 2.13. Mesh convergence study for R100 Bridgman notch tensions specimen.

Bridgman (1944) showed that stress triaxiality increases with increasing a/r ratio as the radius of curvature of the notch decreases (thus becoming more crack-like). Figure 2.14 shows the average stress triaxiality in elements on surface of the notch's cross section (highlighted red in Fig. 2.14-B). Figure 2.14 demonstrates that the average stress triaxiality increases with decreasing notch root radii (increasing a/r ratio) in agreement with the findings of Bridgman (1944). Each specimen geometry was simulated and tested at 25 and 200°C and a constant crosshead velocity of 0.005 mm/s. The two test temperatures (25 and 200°C) serve to validate the model's thermal sensitivity while the three notch radii of 0.05 in. (1.27 mm), 0.1 in. (2.54 mm), and 0.15 in. (3.81 mm) are used to validate model's stress state sensitivity. Figure 2.15 contains the experimental and model load

versus gage section extension data of the notched tension specimen tests. The load-extension data in Fig. 2.15 show that the model predictions fall within the experimental uncertainty ranges for most test conditions. However, the model tends to underpredict extension to failure for R150 specimens (Fig. 2.15-C). Distinct load reductions were observed in the model predicted load-extension behavior of R50 and R100 specimens deformed at 200°C (Fig. 2.15 B-C). The load reductions correspond to the points in the deformation where the central (high triaxiality) region of the notch midplane had accumulated significant damage while the edge (low triaxiality) regions were undamaged and continued to bear load. The predicted load reductions are also a product of the implicit Abaqus FEA scheme's need to retain finite stiffness in damaged elements to avoid singularities in the global stiffness matrix. The elastic modulus (originally 70 GPa) of elements exceeding 40% void area fraction (40% void area fraction was the approximate maximum value observed in experiments) was reduced to 10% of the original modulus (7 GPa) to avoid stiffness matrix singularities and continue the analysis beyond initial element failure. Thus, significantly damaged elements artificially continued to support relatively small loads. Both model and experiments demonstrate that the peak load decreases with decreasing notch root ratio (18, 16, and 14 kN for a/r values of 2.0, 1.0, and 0.67, respectively at ambient temperature) in agreement with the relationship between a/r and load described in Bridgman (1944) and the experimental observations of Hancock and Mackenzie (1976). However, extension to failure increases (0.28, 0.42, and 0.60 mm) for the range of decreasing a/r values due to decreasing magnitudes of triaxiality (shown Fig. 2.14). The observed increase in the rate of damage evolution with increasing triaxiality is

consistent with literature findings (McClintock, 1968; Rice and Tracey, 1969; Gurson, 1977).

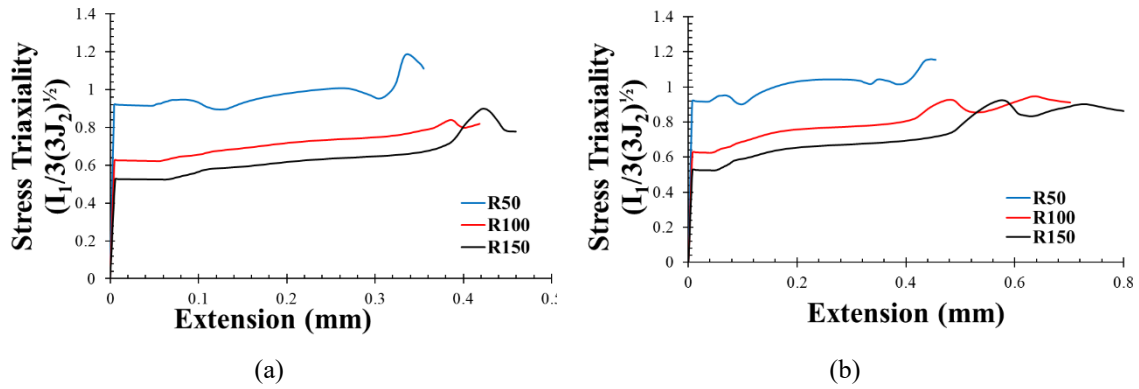
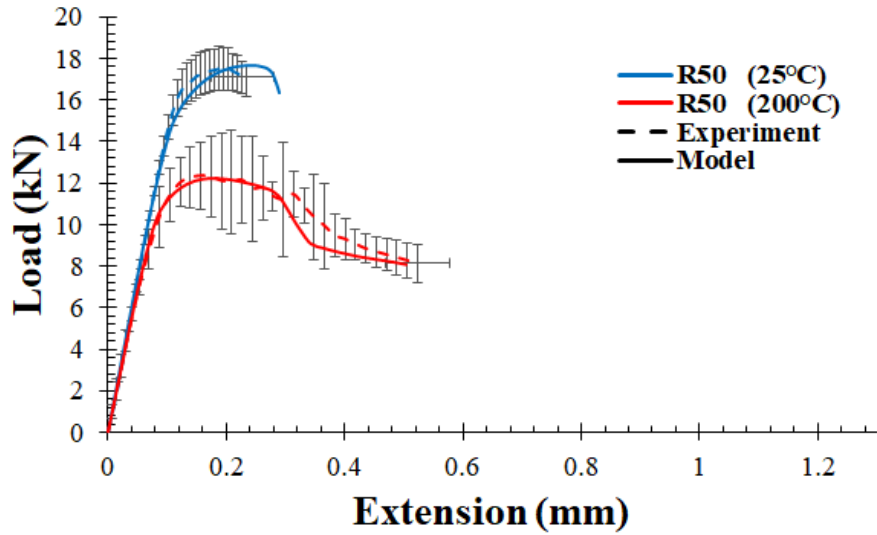
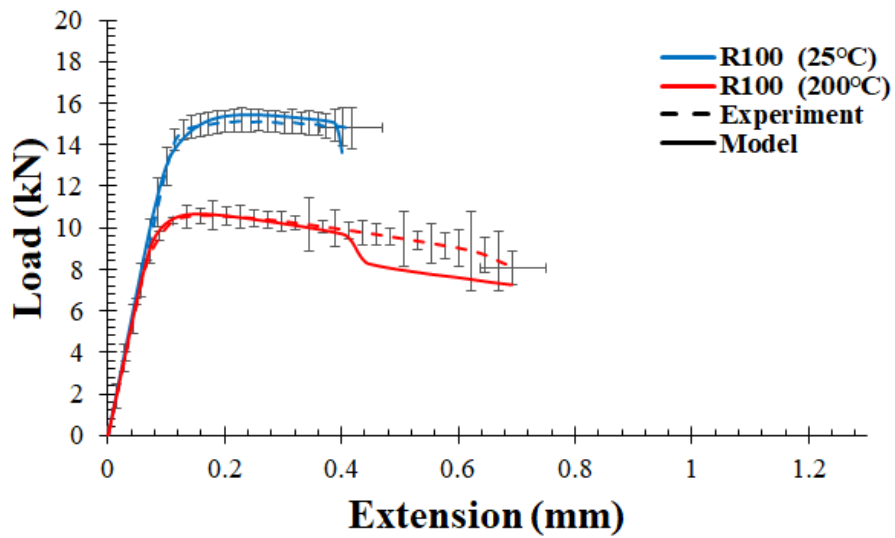


Figure 2.14 FEA Predicted stress triaxiality evolution for notch Bridgman tension specimens deformed varying temperatures.

- (a) Bridgman notched tension specimen stress triaxiality evolution at 25°C.
- (b) Bridgman notched tension specimen stress triaxiality evolution at 200°C.

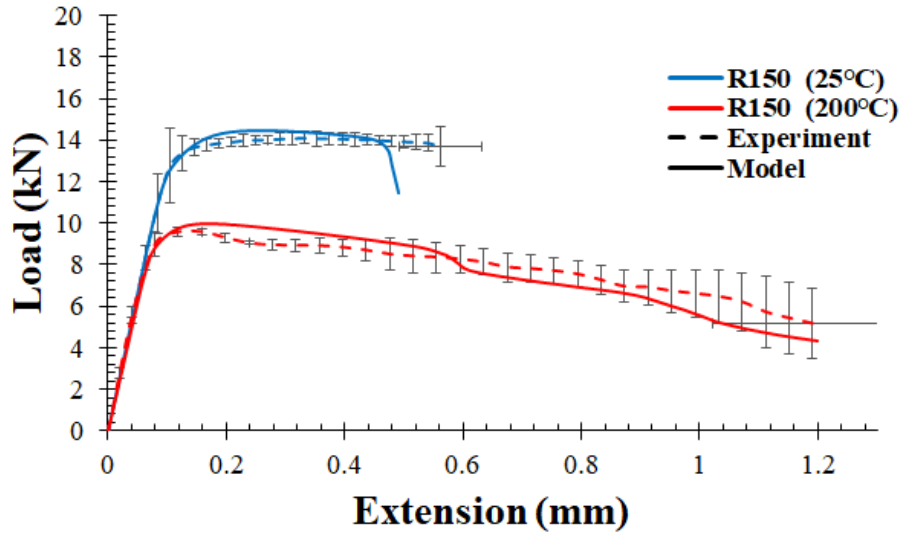


(a)



(b)

Figure 2.15 Comparison of experimental and numerical load-displacement data for Bridgman notched tension specimens deformed at varying stress state and temperature.



(c)

Figure 2.15 (continued)

- (a) R50 specimens deformed at 25 and 200°C.
- (b) R100 specimens deformed at 25 and 200°C.
- (c) R150 specimens deformed at 25 and 200°C.

SEM imaging of the notch Bridgman tension sample fracture surfaces was performed to assess the model's ability to predict microstructural evolution during deformation (Figs. 2.16 – 17). Figure 2.16 shows the void morphology for an R100 specimen deformed at 25°C. The central regions of the fracture surface (Fig. 2.16-B) features significant void nucleation, growth, and coalescence due to the relatively high triaxiality within the region during deformation. The void morphologies range from small spheres to large ellipsoidal shapes. The smaller spherical voids likely nucleated from secondary phase particles while the large voids could have resulted from decohesion of entire grains along grain boundaries. The edge regions of the specimen featured slanted, planar regions indicative of shear localization effects (Fig. 2.16-C). Figure 2.17 shows the

fracture surface morphology for an R100 specimen deformed at 200°C. The central regions of the specimen featured networks of large spherical voids with little distinguishable evidence of grain boundary decohesion (Fig. 2.17-B). The edge regions of the specimen deformed at 200°C featured more evidence of void dimpling than the edge regions of the sample tested at 25°C (Fig. 2.17-C). However, the slanted edge regions of the sample deformed at 200°C were mostly planar, which is indicative of unstable, shear-based cleavage after the onset of localization.

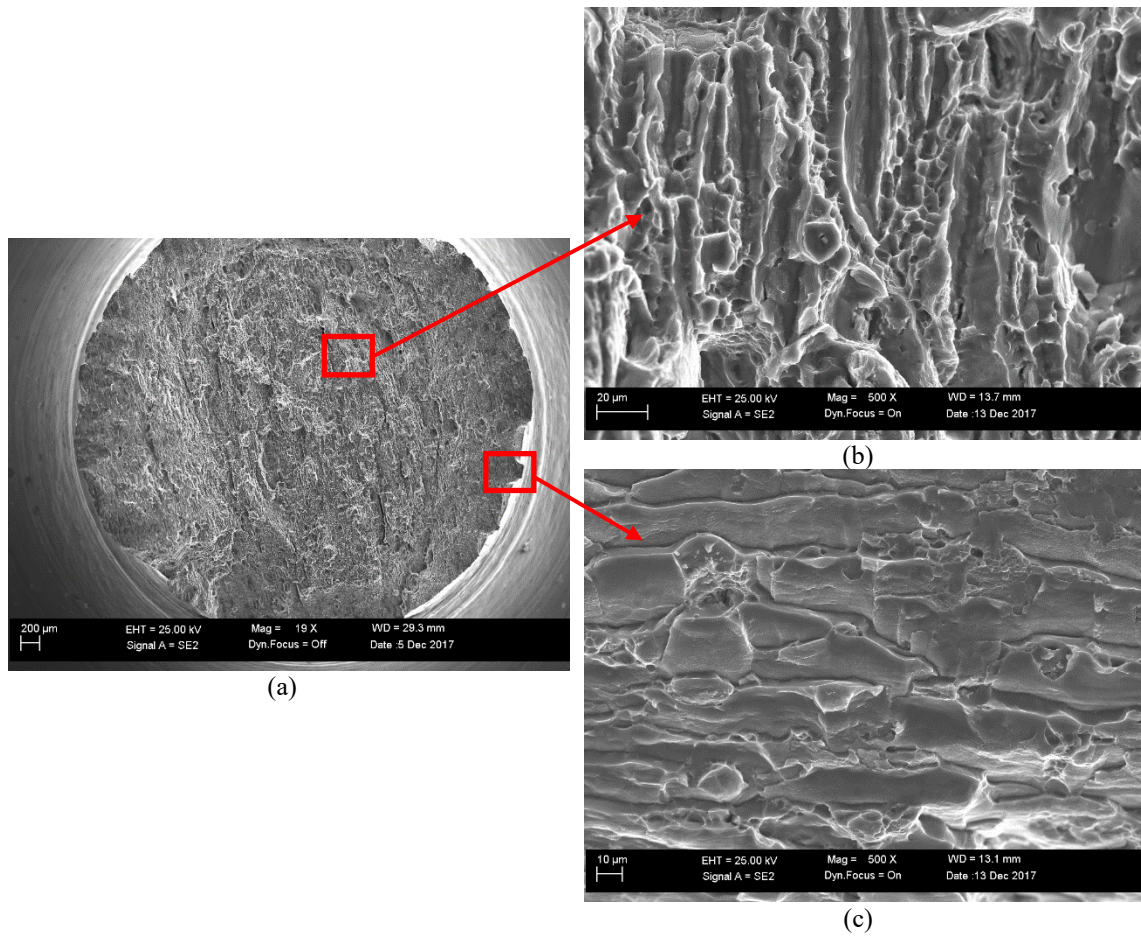


Figure 2.16 Electron micrograph of the fracture surface of R100 specimen deformed at 25°C.

- (a) Fracture surface micrograph.
- (b) Central region featuring triaxiality dominated dimple void evolution.
- (c) Edge region featuring shear dominated fracture.

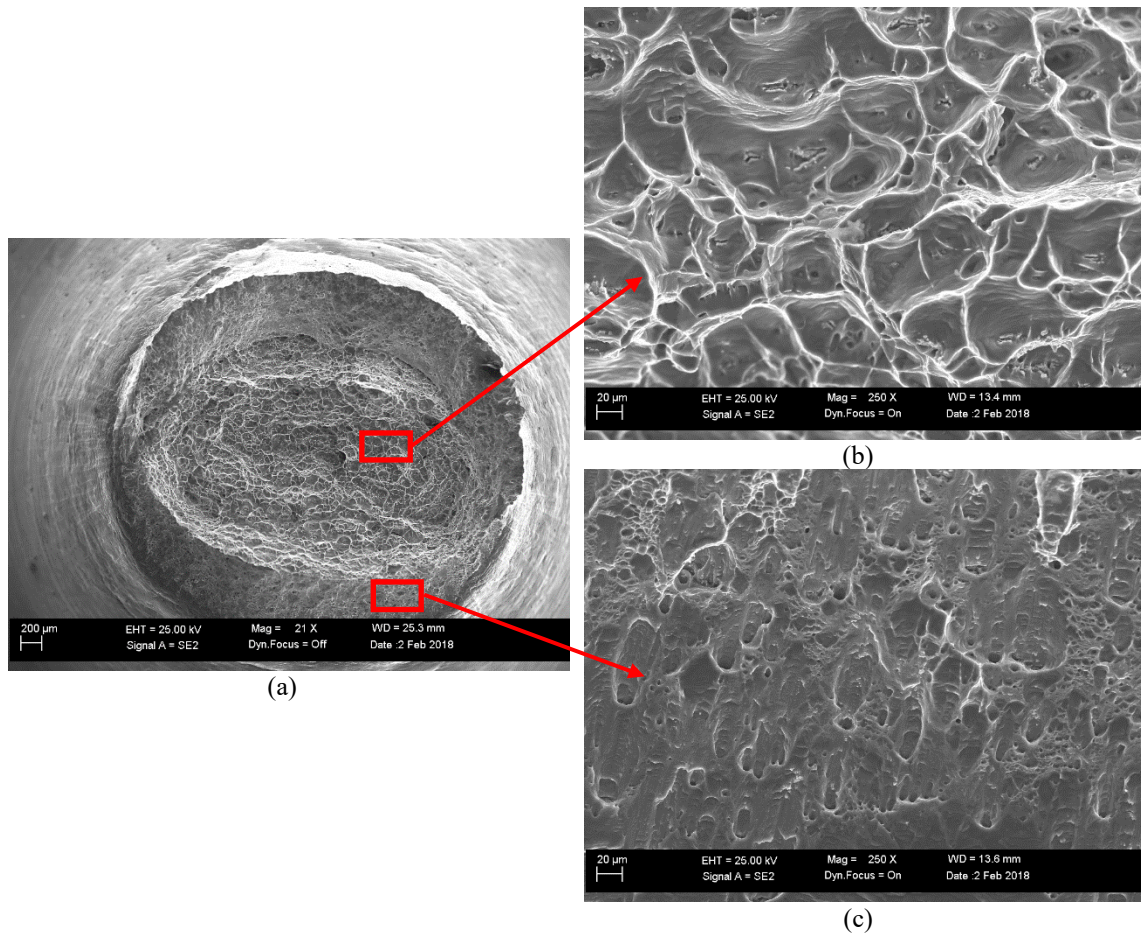
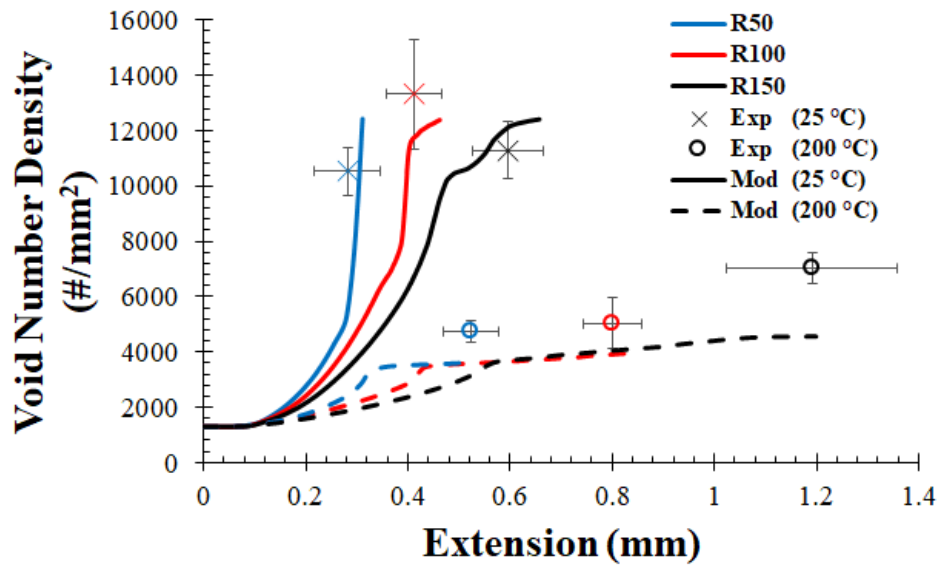


Figure 2.17 Electron micrograph of the fracture surface of R100 specimen deformed at 200°C.

- (a) Fracture surface micrograph.
- (b) Central region featuring large, equiaxed voids due to triaxiality.
- (c) Edge region featuring small dimples and shear dominated planar fracture.

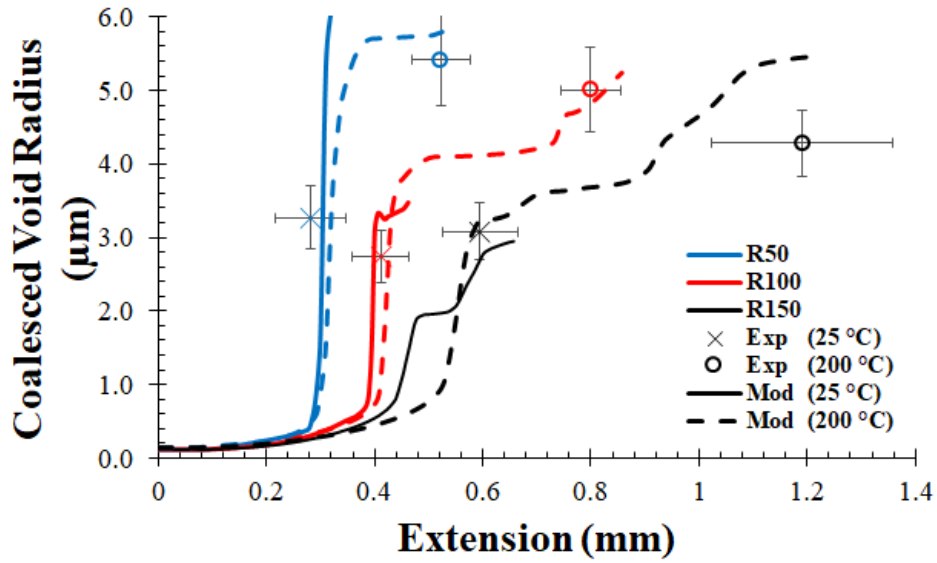
ImageJ software was used to quantify the average void number density, size, and area fraction from the micrographs of notch Bridgman tension specimen fracture surfaces. Microstructural evolution data from notch tension simulations was generated by averaging the void number density, coalesced void radius, and void area fraction values from all elements on the specimen notch cross sectional surface. Figure 2.18 contains experimental

and model predicted data for average void number density, radius, and area fraction versus specimen extension for ambient and 200C notched tension tests. The experimental and predicted data in Fig. 2.18 shows that the rates of void nucleation, growth, and damage evolution with specimen extension increase with increasing a/r ratio (decreasing notch radii) due to increasing triaxiality. The observed tendency of an increase in porosity accumulation rate with increasing triaxiality is concordant with literature findings (McClintock, 1968; Rice and Tracey, 1969; Gurson, 1977).

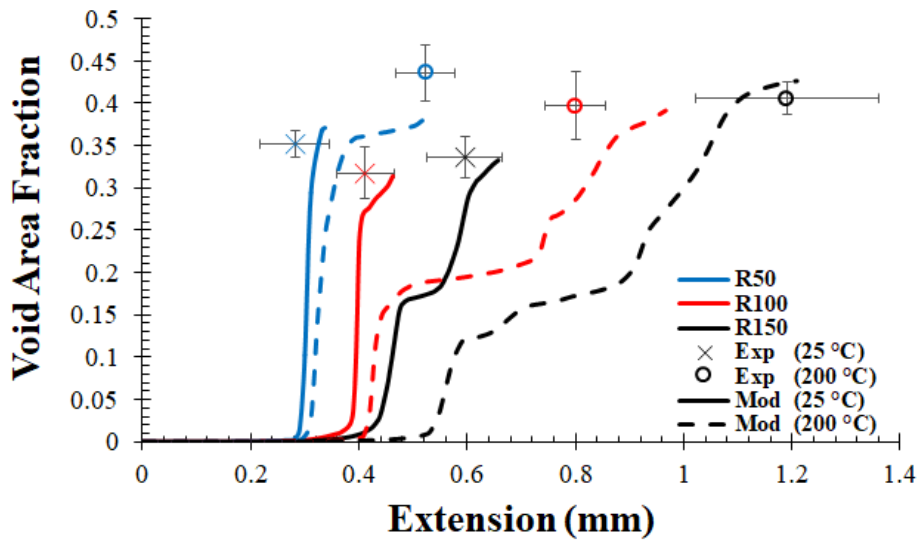


(a)

Figure 2.18 Comparison of experimental and ISV model predicted void property evolution for varying stress state and temperature deformation.



(b)



(c)

Figure 2.18 (continued)

- (a) Comparison of experimental and model predicted void nucleation.
- (b) Comparison of experimental and model predicted product of coalesced void growth.
- (c) Comparison of experimental and model predicted void volume fraction evolution.

In general, Fig. 2.18 shows decreases in the void nucleation and total damage evolution rates with increasing temperatures, which is consistent with the tendencies observed during the model calibration process (Fig. 2.12). The void nucleation rate appears to be particularly sensitive to temperature. R100 specimens deformed at 25°C reached final a final void number density (14,000 voids/mm²) nearly fivefold greater than specimens deformed at 200°C (3,000 voids/mm²). The predicted void growth rates with specimen extension somewhat decrease for increasing temperature (Fig. 2.18-B). However, the average void radius at fracture was larger for the R100 specimens tested at 200°C (5 μm) compared to those tested at 25°C (3 μm). Figure 2.18-C shows the rate of total void area fraction evolution was greatest in the specimens tested at 25°C due to the similarity in void growth rates coupled with the extreme difference in void nucleation rates for varying temperature. The difference in final void area fraction of nearly 10% between 25 and 200°C (Fig. 2.18-C) could be related to a percolation threshold which increases for as voids become more spherical (Xia and Thorpe, 1988; Garboczi and Thorpe, 1995).

2.4 Conclusions

An Internal State Variable (ISV) model has been calibrated and validated using large deformation mechanical experiments at varying strain rates, stress states, and temperatures. The calibrated ISV model was implemented within a predictive Finite Element Analysis (FEA) framework to simulate deformation of structures under complex loading conditions. Analysis of the as-received microstructure revealed the presence of Cu-Fe secondary phase particles within the primary Al-Zn-Mg material phase. These

microstructural heterogeneities could function both as inhibitors to dislocation motion, thus affecting yield and hardening characteristics, and as nucleation sites for void-based damage. Analysis of the grain texture in the ND, RD, and TD material directions showed minimal grain orientation anisotropy effects. Mechanical compression tests in the primary material directions at 0.001 and 1,000 s⁻¹ strain rates corroborate the lack of grain orientation anisotropy by exhibiting minimal directional dependence of the stress-strain response. Mechanical testing showed minimal differences between tension and compression, and minor torsional softening of specimens cut in the RD direction. Therefore, the bulk material should produce a relatively consistent mechanical (stress-strain) response to a given stimuli regardless of the stress state or loading orientation. However, further mechanical tests are necessary to assess the material's response to reverse loading conditions and fatigue. Additionally, the material exhibits minor strain rate dependence over a wide range of strain rates (0.001–1,000 s⁻¹) and significant thermal softening over a range of temperatures (25–200°C).

An ISV-based plasticity-damage model was used to quantify the structure-property relationships of the Al 7085-T711 alloy for application in FEA modeling. Experimental stress-strain data was used to calibrate ISV model equations governing yield and the plasticity evolution mechanisms of isotropic and kinematic hardening. The model calibration curves exhibit strong agreement with experimental stress-strain data. Microstructural data of the undeformed and fractured material was acquired and quantified using SEM and DIC techniques, respectively, for calibration of the void nucleation, growth, and coalescence ISVs for damage. The calibrated damage ISVs exhibit reasonable

agreement with experimental data for a variety of strain rates, temperatures and simple stress states. The calibrated ISV model tends to underpredict the void growth and coalescence rates for increasing temperature.

FEA simulations of the deformation of notch Bridgman tension specimens were performed to validate the Al 7085-T711 ISV plasticity-damage model. Specimens with different notch root radii were tested at 25 and 200°C to determine the model's efficacy at a variety of stress states and temperatures. Both model and experimental results for ambient temperature deformation shows 22% increase in peak load for a decrease in notch radius from 1.5 to 0.05 inches. The decrease in notch root radii also produced a 53% reduction in specimen extension to failure. The ISV model accurately captures the elastic, hardening, and softening regimes of the load-displacement behavior for each specimen type. Increasing the material's temperature caused a pronounced softening of the load-displacement behavior and increased the extension to failure.

Comparisons of experimental and numerical fracture characteristics were made for the variety of notch Bridgman tension test conditions to assess the model's ability to predict microstructural evolution due to deformation. Both experiments and numerical model show the rate of void nucleation and growth increase with increasing stress triaxiality. Elevated temperature testing of the notched tension specimens revealed that the void nucleation and porosity evolution rates significantly decreased with increasing temperatures while void growth rates decreased only slightly. Additionally, a difference in void morphology was noted between specimens tested at 25 and 200°C. For room temperature tests, voids on the fracture surface appear to have a higher average aspect ratio

than for specimens tested at 200°C. The difference in void aspect ratio and decrease in void nucleation rate with increasing temperature suggests a thermally driven transition in damage modes from a void nucleation and crack dominated regime (ambient) to a void growth and coalescence driven regime (200°C). The specimens tested at ambient temperature exhibit a lower final void area fraction (~32%) than the elevated temperature specimens (~41%). The difference in void area fraction at failure could be associated with a thermally induced transition from shear to triaxiality influenced damage evolution at elevated temperatures.

CHAPTER III
A PHYSICALLY-MOTIVATED INTERNAL STATE VARIABLE MODEL FOR
DUCTILE DAMAGE EVOLUTION DUE TO SHEAR

3.1 Introduction

3.1.1 Damage Modeling History

Modeling damage evolution is essential to accurately predict inelastic behavior of materials. The genesis of macroscale damage modeling can perhaps be traced to the Griffith (1921) fracture energy criterion and Linear Elastic Fracture Mechanics (LEFM) established by Irwin (1948; 1957). From the field of nonlinear fracture mechanics evolved the Crack Tip Opening Displacement (CTOD) criterion (Well, 1961; McMeeking, 1977; Rice and Sorenson, 1978; Shih *et al.* 1979; Kanninen *et al.* 1979), Crack Tip Opening Angle (CTOA) criterion (de Koning, 1975; Newman, 1984) and J-integral theory (Rice, 1968; Begley and Landes, 1972; Rice *et al.* 1973). These fracture modeling paradigms are viable for a wide range of materials and structural geometries; however, this study focuses on application of void-based damage concepts for predicting failure in visco-plastic alloys.

Modeling void-based damage evolution in materials began with Kachanov's (1958) study of micro-void-based damage evolution under creep conditions. Rabotnov (1963)

expanded the concept by deriving creep void growth rate equations. Soon thereafter, several micro-void growth models featuring hyperbolic correlations of stress triaxiality to growth rates were developed (McClintock, 1968; Rice and Tracey, 1969, Gurson, 1977; Cocks and Ashby, 1982). Gangulee and Gurland (1967) established an empirical relationship between second phase particle properties and void nucleation rates. Later, Bourcier and Koss (1979) investigated orientation effects of neighboring voids in aluminum, thus establishing a paradigm for void interaction and coalescence. Budiansky *et al.* (1982) established a relationship between void growth and material hardening rate and the effect of stress state on void shape. Cocks and Ashby (1982) developed a model that coupled grain-boundary diffusion, void surface diffusion, and creep effects for predicting void growth. A void volume fraction evolution model framework was developed by Tvergaard and Needleman by coupling Gurson (1977) void growth with void nucleation effects (Tvergaard, 1982A-B; Tvergaard and Needleman, 1984A-B; Needleman and Tvergaard, 1987; Needleman, 1987). The Gurson model has been modified to account for low stress triaxiality influenced void growth (Nashon and Hutchinson, 2008).

The Bammann-Chiesa-Johnson (BCJ) Internal State Variable (ISV) model for the prediction of plasticity and damage (Bammann 1984; Bammann 1990; Bammann *et al.* 1993; Bammann *et al.* 1996) was developed in the thermodynamically consistent framework established by Coleman and Gurtin (1967). This plasticity-damage model extended the Bammann (1984) ISV model for visco-plastic materials and features a Cocks-Ashby (1982) based void growth rule. Marin and McDowell (1996) demonstrated the ISV plasticity-damage model's (Bammann *et a.* 1993; 1996) viability in predicting the damage

evolution dominated post necking behavior of ductile materials. The BCJ model was extended by Horstemeyer and Gokhale (1999) and Horstemeyer *et al.* (2000A-C) to consider the effects of nucleation, growth, and coalescence of voids from microstructural heterogeneities. This ISV model framework (a.k.a., “MSU ISV Plasticity-Damage Model”) has been used to characterize structure-property relationships for aluminum (Horstemeyer *et al.* 2000A; Jordon 2007; Tucker *et al.* 2010), steel (Horstemeyer *et al.* 2000B; Horstemeyer and Ramaswamy, 2000; Guo *et al.* 2005; Anurag *et al.* 2009; Whittington *et al.* 2014), copper (Crapps *et al.* 2010), titanium (Guo *et al.* 2005), and magnesium (Lugo *et al.* 2011; Walton *et al.* 2014; Lugo *et al.* 2018) alloys. The constitutive model has been implemented in FEA to simulate a variety of thermomechanical deformations including forming processes (Bammann *et al.* 1996; Horstemeyer and Ramaswamy, 2000; Crapps *et al.* 2010; Cho *et al.* 2015; Cho *et al.* 2018), high velocity impacts (Bammann *et al.* 1993; Whittington *et al.* 2014) and structural crashworthiness (Bammann *et al.* 1993; Fang *et al.* 2005; Horstemeyer *et al.* 2009).

3.2 Internal State Variable Constitutive Model

3.2.1 Kinematics

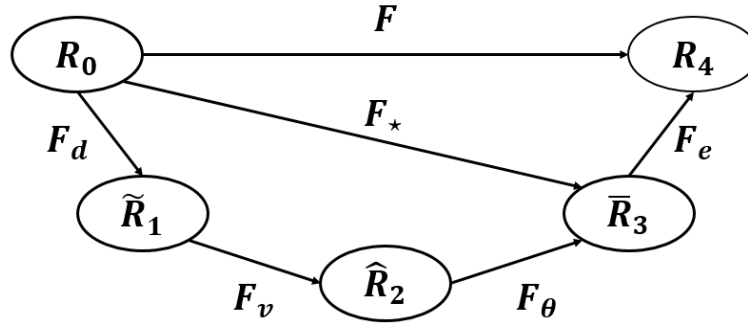


Figure 3.1 Multiplicative decomposition of the deformation gradient into elastic (F_e) and inelastic (F_d , F_v , and F_θ) components (cf. Bammann and Solanki, 2010).

Consider a three-dimensional continuous material subjected to a thermomechanical deformation. Let X denote the material coordinate points with respect to a reference configuration (\mathbf{R}_0), and let x represent the material points in the current configuration (\mathbf{R}_4). The deformation gradient that maps point X from \mathbf{R}_0 to x in \mathbf{R}_4 is as follows:

$$\mathbf{F} = \frac{\partial x}{\partial X}. \quad (3.1)$$

For large strains, the second-rank deformation gradient tensor, \mathbf{F} , can be multiplicatively decomposed into a product of the elastic and inelastic components of thermomechanical deformation (Lee and Liu, 1967) as shown in Fig. 3.1. The components of the total deformation gradient \mathbf{F} are as follows: F_d represents inelastic shape distorting deformation, F_v represents dissipative volumetric change, F_θ corresponds to expansion or contraction of the material due to thermal stimuli, and F_e represents the recoverable elastic deformation. The multiplicative decomposition of \mathbf{F} is given by:

$$\mathbf{F} = \mathbf{F}_e \mathbf{F}_\theta \mathbf{F}_v \mathbf{F}_d. \quad (3.2)$$

The decomposition may be further simplified to the product of the inelastic deformation gradient component, \mathbf{F}_\star , and its elastic counterpart, \mathbf{F}_e , where \mathbf{F}_\star is composed of the dissipative elements (Lee and Liu, 1967) from Eq. (3.2), i.e.,

$$\mathbf{F} = \mathbf{F}_e \mathbf{F}_\star, \quad (3.3)$$

$$\mathbf{F}_\star = \mathbf{F}_\theta \mathbf{F}_v \mathbf{F}_d. \quad (3.4)$$

The thermal deformation gradient, \mathbf{F}_θ , is formulated assuming a simple linear isotropic expansion,

$$\mathbf{F}_\theta = F_t \mathbf{I} = (1 + \alpha_{TH} \Delta\theta) \mathbf{I}, \quad (3.5)$$

where α_{TH} represents the material coefficient of thermal expansion, $\Delta\theta$ is the temperature gradient, and \mathbf{I} is the second rank identity tensor. The Jacobian of the volumetric component of the deformation gradient, \mathbf{F}_v , maps the volumetric change from \tilde{V} in \mathbf{R}_1 to \hat{V} in the \mathbf{R}_2 intermediate configuration:

$$\det \mathbf{F}_v = J_v = \frac{\hat{V}}{\tilde{V}}. \quad (3.6)$$

The volumetric change is caused by the evolution of void volume, V_v , in the material. The material volume in \mathbf{R}_2 , \hat{V} , is taken to be the sum of V_v and the material volume in \mathbf{R}_1 , \tilde{V} . The void volume fraction is therefore the quotient of the void volume, V_v , and total material volume in \mathbf{R}_2 , \hat{V} ,

$$\hat{V} = V_v + \tilde{V}, \quad (3.7)$$

where

$$\phi = \frac{V_v}{\bar{v}}. \quad (3.8)$$

The volumetric component of the deformation gradient can be formulated as a function of ϕ ,

$$J_v = \frac{1}{(1-\phi)}, \quad (3.10)$$

$$\mathbf{F}_v = \frac{1}{(1-\phi)^{1/3}} \mathbf{I}. \quad (3.11)$$

The total Jacobian which represents the total volumetric change from \mathbf{R}_θ to \mathbf{R}_d is

$$J = \det \mathbf{F} = \det \mathbf{F}_d \det \mathbf{F}_v \det \mathbf{F}_\theta \det \mathbf{F}_e, \quad (3.12)$$

where

$$\det \mathbf{F}_e = J_e > 0, \det \mathbf{F}_\theta = F_t^3 = (1 + \alpha_T \Delta \theta)^3, J_d = \det \mathbf{F}_d = 1,$$

and plastic incompressibility is assumed for the distortional Jacobian, J_d .

The second-rank Cauchy-Green deformation tensors are derived for each material configuration (\mathbf{R}_θ - \mathbf{R}_d) as functions of the deformation gradient tensors in (2):

$$\mathbf{C} = \mathbf{F}^T \mathbf{F}, \mathbf{C}_d = \mathbf{F}_d^T \mathbf{F}_d, \mathbf{C}_* = \mathbf{F}_*^T \mathbf{F}_*, \tilde{\mathbf{C}}_v = \mathbf{F}_v^T \mathbf{F}_v, \hat{\mathbf{C}}_\theta = \mathbf{F}_\theta^T \mathbf{F}_\theta, \bar{\mathbf{C}}_e = \mathbf{F}_e^T \mathbf{F}_e. \quad (3.13)$$

The corresponding Green-Lagrange strain tensors are given by,

$$\mathbf{E} = \frac{1}{2}(\mathbf{C} - \mathbf{I}), \mathbf{E}_d = \frac{1}{2}(\mathbf{C}_d - \mathbf{I}), \mathbf{E}_* = \frac{1}{2}(\mathbf{C}_* - \mathbf{I}), \quad (3.14)$$

$$\tilde{\mathbf{E}}_v = \frac{1}{2}(\tilde{\mathbf{C}}_v - \mathbf{I}), \hat{\mathbf{E}}_\theta = \frac{1}{2}(\hat{\mathbf{C}}_\theta - \mathbf{I}), \bar{\mathbf{E}}_e = \frac{1}{2}(\bar{\mathbf{C}}_e - \mathbf{I}).$$

The Cauchy-Green tensors in Eq. (13) can be subjected to a spectral decomposition,

$$\mathbf{C} = \sum_{i=1}^3 \lambda_i^2 \mathbf{n}_i \otimes \mathbf{n}_i, \quad (3.15)$$

where λ_i physically represents the stretch ratio formulated as the square root of the eigenvalues of \mathbf{C} corresponding to the orthonormal eigenvector, \mathbf{n}_i . The deformation gradient tensor for each configuration can be subjected to a polar decomposition of the form

$$\mathbf{F} = \mathbf{R} \cdot \mathbf{U}, \quad (3.16)$$

where \mathbf{R} is the rotation tensor, and \mathbf{U} is the right stretch tensor. The stretch tensor, \mathbf{U} , is related to the Cauchy-Green deformation tensor by

$$\mathbf{U} = \sqrt{\mathbf{C}} = \sum_{i=1}^3 \lambda_i n_i \otimes n_i. \quad (3.17)$$

The right stretch tensor associated with damage in the \mathbf{R}_1 and \mathbf{R}_3 intermediate configurations using the “push forward” operation described in Holzapfel (2000),

$$\begin{aligned} \tilde{\mathbf{U}}_v &= \tilde{\mathbf{C}}_v^{1/2} = (\mathbf{F}_v^T \mathbf{F}_v)^{1/2} = (1 - \phi)^{-1/3} \mathbf{I}, \\ \bar{\mathbf{U}}_v &= \mathbf{F}_\theta^T \mathbf{F}_v^T \tilde{\mathbf{U}}_v \mathbf{F}_v^{-1} \mathbf{F}_\theta^{-1}. \end{aligned} \quad (3.18)$$

The rate form of the volumetric right stretch tensor in the \mathbf{R}_3 configuration becomes

$$\dot{\bar{\mathbf{U}}}_v = - \frac{\dot{\phi}}{3F_\theta^2(1-\phi)^{2/3}} \mathbf{I} \quad (3.19)$$

A scalar form of the volumetric right stretch tensor for application in conjunction with a scalar internal variable in the thermodynamic relations is as follows,

$$\begin{aligned}\bar{l}_v &= \frac{1}{3} \text{tr}(\bar{\mathbf{U}}_v) = \frac{(1-\phi)^{1/3}}{F_\theta^2}, \\ \dot{\bar{l}}_v &= -\frac{\dot{\phi}}{3F_\theta^2(1-\phi)^{2/3}}.\end{aligned}\quad (3.20)$$

The total velocity gradient tensor, \mathbf{L} , in \mathbf{R}_4 and inelastic velocity gradient, \mathbf{L}_* , in \mathbf{R}_3 are formulated as:

$$\mathbf{L} = \dot{\mathbf{F}}\mathbf{F}^{-1} = \dot{\mathbf{F}}_e\mathbf{F}_e^{-1} + \mathbf{L}_e\mathbf{L}_*\mathbf{L}_e^{-1}, \quad (3.21)$$

$$\bar{\mathbf{L}}_* = \dot{\mathbf{F}}_\theta\mathbf{F}_\theta^{-1} + \mathbf{F}_\theta\dot{\mathbf{F}}_v\mathbf{F}_v^{-1}\mathbf{F}_\theta^{-1} + \mathbf{F}_\theta\mathbf{F}_v\dot{\mathbf{F}}_d\mathbf{F}_d^{-1}\mathbf{F}_v^{-1}\mathbf{F}_\theta^{-1}.$$

The thermal and volumetric components of the deformation gradient are assumed to be isotropic, therefore the corresponding velocity gradients become

$$\bar{\mathbf{L}}_\theta = \dot{\mathbf{F}}_\theta\mathbf{F}_\theta^{-1} = \dot{\mathbf{F}}_\theta\mathbf{F}_\theta^{-1}\mathbf{I} = \mathbf{F}_\theta^{-1}\frac{\partial F_\theta}{\partial \theta}\dot{\theta}\mathbf{I} = f_\theta\dot{\theta}\mathbf{I}, \quad (3.22)$$

$$\mathbf{l}_\theta = \mathbf{F}_e\mathbf{L}_\theta\mathbf{F}_e^{-1} = f_\theta\dot{\theta}\mathbf{I},$$

$$\hat{\mathbf{L}}_v = \dot{\mathbf{F}}_v\mathbf{F}_v^{-1} = \frac{\dot{\phi}}{3(1-\phi)}\hat{\mathbf{I}}, \quad \bar{\mathbf{L}}_v = \mathbf{F}_\theta\hat{\mathbf{L}}_v\mathbf{F}_\theta^{-1} = \frac{\dot{\phi}}{3(1-\phi)}\bar{\mathbf{I}}, \quad (3.23)$$

$$\mathbf{l}_v = \mathbf{F}_e\mathbf{L}_v\mathbf{F}_e^{-1} = \frac{\dot{\phi}}{3(1-\phi)}\bar{\mathbf{I}}.$$

Pulling back \mathbf{L} from the current configuration, \mathbf{R}_4 , to the intermediate configuration, \mathbf{R}_3 , yields

$$\bar{\mathbf{L}} = \mathbf{F}_e^{-1}\mathbf{L}\mathbf{F}_e^{-1} = \bar{\mathbf{L}}_e + \bar{\mathbf{L}}_*, \quad (3.24)$$

where the elastic velocity gradient tensor in \mathbf{R}_3 is

$$\bar{\mathbf{L}}_e = \mathbf{F}_e^{-1}\dot{\mathbf{F}}_e. \quad (3.25)$$

The rate of deformation, \mathbf{D} , and spin, \mathbf{W} , tensors in the current configuration, \mathbf{R}_4 , are formulated as the symmetric and asymmetric components of the velocity gradient, \mathbf{L} ,

$$\mathbf{L} = \mathbf{D} + \mathbf{W}, \quad (3.26)$$

$$\mathbf{D} = \text{Sym}(\mathbf{L}) = \frac{1}{2}(\mathbf{L} + \mathbf{L}^T), \quad (3.27)$$

$$\mathbf{W} = \text{Skew}(\mathbf{L}) = \frac{1}{2}(\mathbf{L} - \mathbf{L}^T). \quad (3.28)$$

Similarly, the rate of deformation and spin tensors in the intermediate, \mathbf{R}_3 configuration becomes

$$\bar{\mathbf{L}} = \bar{\mathbf{D}} + \bar{\mathbf{W}}, \quad (3.29)$$

$$\bar{\mathbf{D}} = \text{Sym}(\bar{\mathbf{L}}) = \frac{1}{2}(\bar{\mathbf{L}} + \bar{\mathbf{L}}^T), \quad (3.30)$$

$$\bar{\mathbf{W}} = \text{Skew}(\bar{\mathbf{L}}) = \frac{1}{2}(\bar{\mathbf{L}} - \bar{\mathbf{L}}^T). \quad (3.31)$$

The Green-Lagrange strain tensors pushed back to the intermediate configuration, \mathbf{R}_3 , and the reference configuration, \mathbf{R}_0 , become

$$\bar{\mathbf{E}} = \bar{\mathbf{E}}_e + \bar{\mathbf{E}}_* = \bar{\mathbf{E}}_e + \mathbf{F}_*^{-T} \mathbf{E}_* \mathbf{F}_*^{-1}, \quad (3.32)$$

$$\mathbf{E} = \mathbf{F}_*^T \bar{\mathbf{E}} \mathbf{F}_* + \mathbf{E}_*. \quad (3.33)$$

The material time derivative of the Green-Lagrange strain tensor in the intermediate configuration, \mathbf{R}_3 , is

$$\dot{\bar{\mathbf{E}}} = \mathbf{F}_e^T \mathbf{D} \mathbf{F}_e - (\bar{\mathbf{L}}^T - \bar{\mathbf{L}}_e^T) \bar{\mathbf{E}} - \bar{\mathbf{E}} (\bar{\mathbf{L}} - \bar{\mathbf{L}}_e). \quad (3.34)$$

where

$$\mathbf{F}_e^T \mathbf{D} \mathbf{F}_e = \mathbf{F}_e^T \mathbf{D}_e \mathbf{F}_e + \mathbf{F}_e^T \mathbf{D}_* \mathbf{F}_e,$$

$$\mathbf{F}_e^T \mathbf{D} \mathbf{F}_e = \bar{\mathbf{D}}_* + \bar{\mathbf{L}}_*^T \bar{\mathbf{E}}_e + \bar{\mathbf{E}}_e \bar{\mathbf{L}}_*,$$

$$\mathbf{F}_e^T \mathbf{D}_e \mathbf{F}_e = \dot{\bar{\mathbf{E}}}_e,$$

$$\dot{\bar{\mathbf{E}}}_* = \bar{\mathbf{D}}_* - \bar{\mathbf{L}}_*^T \bar{\mathbf{E}}_e - \bar{\mathbf{E}}_e \bar{\mathbf{L}}_*,$$

$$\dot{\bar{\mathbf{E}}}_e = \mathbf{F}_e^T \mathbf{D}_e \mathbf{F}_e = \mathbf{F}_e^T \mathbf{D} \mathbf{F}_e - \bar{\mathbf{D}}_* - (\bar{\mathbf{L}}^T - \bar{\mathbf{L}}_e^T) \bar{\mathbf{E}}_e - \bar{\mathbf{E}}_e (\bar{\mathbf{L}} - \bar{\mathbf{L}}_e).$$

A listing of the stress tensors and velocity gradient tensors associated with each material configuration (\mathbf{R}_1 - \mathbf{R}_4) is included in Table 3.1.

Table 3.1 List of stresses and velocity gradients in the various material configurations.

Configuration	Stress	Velocity Gradient
\mathbf{R}_4	$\boldsymbol{\sigma}$	$\mathbf{L} = \dot{\mathbf{F}} \mathbf{F}^{-1}$
$\bar{\mathbf{R}}_3$	$\bar{\mathbf{S}}_3 = J_e \mathbf{F}_e^{-1} \boldsymbol{\sigma} \mathbf{F}_e^{-T}$	$\bar{\mathbf{L}} = \mathbf{F}_e^T \mathbf{L}_e \mathbf{F}_e + \mathbf{F}_e^T \mathbf{L}_* \mathbf{F}_e$
$\hat{\mathbf{R}}_2$	$\hat{\mathbf{S}}_2 = J_\theta \mathbf{F}_\theta^{-1} \bar{\mathbf{S}}_3 \mathbf{F}_\theta^{-T}$	$\hat{\mathbf{L}} = \mathbf{F}_\theta^{-1} \bar{\mathbf{L}} \mathbf{F}_\theta$
$\tilde{\mathbf{R}}_1$	$\tilde{\mathbf{S}}_1 = J_v \mathbf{F}_v^{-1} \hat{\mathbf{S}}_2 \mathbf{F}_v^{-T}$	$\tilde{\mathbf{L}} = \mathbf{F}_v^{-1} \hat{\mathbf{L}} \mathbf{F}_v$
\mathbf{R}_0	$\mathbf{S}_0 = J_d \mathbf{F}_d^{-1} \tilde{\mathbf{S}}_1 \mathbf{F}_d^{-T}$	$\mathbf{L}_0 = \mathbf{F}_d^{-1} \tilde{\mathbf{L}} \mathbf{F}_d$

3.2.2 Thermodynamics

The thermodynamic framework in this work is consistent with that of Coleman and Gurtin (1967) who introduced ISVs into the thermodynamic laws to describe dissipative

processes associated with deformation. The first law of thermodynamics is presented in the current, \mathbf{R}_4 , configuration following Bouvard *et al.* (2013) and Francis *et al.* (2014) as:

$$\dot{e}_V + e_V \text{tr}(\bar{\mathbf{L}}_*) - \boldsymbol{\sigma} : \mathbf{D} - r_V + \nabla \cdot \mathbf{q} = 0, \quad (3.35)$$

where \dot{e}_V is the specific rate of change in internal energy, r_V is the heat source per unit volume, and \mathbf{q} is the thermal flux. The first law of thermodynamics in the \mathbf{R}_3 configuration is given as:

$$\dot{\bar{e}}_V + \bar{e}_V \text{tr}(\bar{\mathbf{L}}_*) - \left[\bar{\mathbf{S}}_3 : \dot{\bar{\mathbf{E}}}_e + \bar{\mathbf{M}} : \bar{\mathbf{D}}_d + \bar{\mathbf{M}} : \bar{\mathbf{D}}_v + \bar{\mathbf{M}} : \bar{\mathbf{D}}_\theta \right] + \bar{r}_V + \nabla \cdot \mathbf{q} = 0, \quad (3.36)$$

where $\bar{\mathbf{S}}_3$ is the second Piola-Kirchoff stress tensor, $\bar{\mathbf{M}} = \bar{\mathbf{C}}_e \bar{\mathbf{S}}_3$ is the Mandel stress tensor, and $\bar{\mathbf{C}}_e$ is the Cauchy-Green stretch tensor defined in Eq. (3.13). The second law of thermodynamics governing the direction of energy dissipation is posed in the \mathbf{R}_3 configuration as

$$\dot{\bar{s}}_V + s_V \text{tr}(\bar{\mathbf{L}}_*) - \theta^{-1} \bar{r}_V + \theta^{-2} \mathbf{q} \cdot \nabla \theta - \theta^{-1} \nabla \cdot \mathbf{q} \geq 0. \quad (3.37)$$

In Eq. (3.36) \bar{s}_V is the specific entropy. The first and second laws can be combined to correlate energy dissipation and applied mechanical energy as shown in Duhem (1911). The Clausius Duhem (C-D) inequality is formulated in the intermediate \mathbf{R}_3 configuration as

$$\begin{aligned} & \dot{\bar{s}}_V + \bar{s}_V \text{tr}(\bar{\mathbf{L}}_*) + \theta^{-2} \mathbf{q} \cdot \nabla \theta + \theta^{-1} \left[\bar{\mathbf{S}}_3 : \dot{\bar{\mathbf{E}}}_e + \bar{\mathbf{M}} : \bar{\mathbf{D}}_d + \bar{\mathbf{M}} : \bar{\mathbf{D}}_v + \bar{\mathbf{M}} : \bar{\mathbf{D}}_\theta \right] - \\ & \theta^{-1} \dot{\bar{e}}_V - \bar{e}_V \text{tr}(\bar{\mathbf{L}}_*) \geq 0. \end{aligned} \quad (3.38)$$

The term $\text{tr}(\bar{\mathbf{L}}_*)$ is expanded in Francis *et al.* (2013) as:

$$\text{tr}(\bar{\mathbf{L}}_*) = 3f_\theta \dot{\theta} + \frac{\dot{\phi}}{(1-\phi)} \quad (3.39)$$

The Helmholtz free energy and its associated rate form in the current \mathbf{R}_4 configuration are given as

$$\bar{\psi}_V = \bar{e}_V - \theta \bar{s}_V, \quad (3.40)$$

$$\dot{\bar{\psi}}_V = \dot{\bar{e}}_V - \dot{\theta} \bar{s}_V - \dot{s}_V \theta. \quad (3.41)$$

The internal energy rate can be isolated to bring the Helmholtz free energy into the C-D inequality

$$\dot{\bar{e}}_V = \dot{\bar{\psi}}_V + \dot{\theta} \bar{s}_V + \dot{s}_V \theta. \quad (3.42)$$

Substituting Eq. (3.41) into Eq. (3.37), the C-D in the intermediate \mathbf{R}_3 configuration becomes

$$-\dot{\bar{\psi}}_V - \bar{\psi}_V \text{tr}(\bar{\mathbf{L}}_*) + \left[\bar{\mathbf{S}}_3 : \dot{\bar{\mathbf{E}}}_e + \bar{\mathbf{M}} : \bar{\mathbf{D}}_d + \bar{\mathbf{M}} : \bar{\mathbf{D}}_v + \bar{\mathbf{M}} : \bar{\mathbf{D}}_\theta \right] - \dot{\theta} \bar{s}_V + \theta^{-1} \mathbf{q} \cdot \nabla \theta \geq 0, \quad (3.43)$$

Francis *et al.* (2014) assumed that the Helmholtz free energy is a function of the tensor product of elastic strain and volumetric stretch, temperature, and a set of internal state variables that are affected by damage:

$$\bar{\psi} = \hat{\psi}(\bar{\mathbf{E}}_e \bar{\mathbf{U}}_v, \theta, \bar{\nabla} \theta, \bar{\mathbf{A}}_i), \quad (3.44)$$

$$\bar{\mathbf{A}}_i = \mathbf{A}_i(\bar{\varepsilon}_s \bar{t}_v, \bar{\boldsymbol{\beta}} \bar{\mathbf{U}}_v, \theta, \bar{\nabla} \theta). \quad (3.45)$$

In Eq. (3.44)-(3.45), $\bar{\varepsilon}_s$ and $\bar{\boldsymbol{\beta}}$ are a strain scalar and tensors resulting from internal microstructural evolution related to Statistically Stored Dislocations (SSD) and

Geometrically Necessary Dislocations (GND), respectively. The scalar volumetric stretch related to the ISV representing SSDs is taken to be the trace of the volumetric stretch vector

$$\bar{t}_v = \frac{tr(\bar{U}_v)}{3}. \quad (3.46)$$

Therefore, the functional form of the Helmholtz free energy in the intermediate R_3 configuration becomes

$$\bar{\psi} = \hat{\psi}(\bar{E}_e \bar{U}_v, \theta, \bar{\nabla} \theta, \bar{\varepsilon}_s \bar{t}_v, \bar{\beta} \bar{U}_v). \quad (3.47)$$

In Eq. (3.47) $\bar{\varepsilon}_s$ and $\bar{\beta}$ represent strains from statistically stored and geometrically necessary dislocation densities, respectively (Solanki and Bammann, 2010). The material time derivative of the Helmholtz free energy can be evaluated to establish the thermodynamic work conjugate pairs described by Coleman and Gurtin (1967). The rate form of the Helmholtz free energy functional is formulated as

$$\begin{aligned} \dot{\bar{\psi}} = & \frac{\partial \bar{\psi}}{\partial (\bar{\varepsilon}_s \bar{t}_v)} \cdot \dot{\bar{\varepsilon}}_s \bar{t}_v + \frac{\partial \bar{\psi}}{\partial (\bar{\varepsilon}_s \bar{t}_v)} \cdot \bar{\varepsilon}_s \dot{\bar{t}}_v + \frac{\partial \bar{\psi}}{\partial (\bar{\beta} \bar{U}_v)} : \dot{\bar{\beta}} \bar{U}_v + \frac{\partial \bar{\psi}}{\partial (\bar{\beta} \bar{U}_v)} : \bar{\beta} \dot{\bar{U}}_v + \frac{\partial \bar{\psi}}{\partial \theta} \cdot \dot{\theta} + \\ & \frac{\partial \bar{\psi}}{\partial \bar{\nabla} \theta} \cdot \dot{\bar{\nabla}} \theta + \frac{\partial \bar{\psi}}{\partial \bar{E}_e \bar{U}_v} : \dot{\bar{E}}_e \bar{U}_v + \frac{\partial \bar{\psi}}{\partial \bar{E}_e \bar{U}_v} : \bar{E}_e \dot{\bar{U}}_v. \end{aligned} \quad (3.48)$$

Reintroducing Eq. (3.48) into Eq. (3.41) and organizing the terms, the C-D inequality in the R_3 intermediate configuration becomes

$$\begin{aligned} & \left[\bar{S}_3 - \frac{\partial \bar{\psi}_V}{\partial \bar{E}_e \bar{U}_v} \bar{U}_v^T \right] : \dot{\bar{E}}_e - \frac{\partial \bar{\psi}}{\partial \bar{E}_e \bar{U}_v} : \bar{E}_e \dot{\bar{U}}_v + \bar{M} : \bar{D}_d + \left[f_\theta \bar{M} : \mathbf{I} - \frac{\partial \bar{\psi}_V}{\partial \theta} - \bar{S}_v - 3f_\theta \psi_V \right] \cdot \\ & \dot{\theta} + \left[\frac{\partial \bar{\psi}}{\partial \bar{E}_e \bar{U}_v} : \bar{E}_e \bar{U}_v + \bar{M} : \mathbf{I} - \frac{\partial \bar{\psi}_V}{\partial (\bar{\varepsilon}_s \bar{t}_v)} \cdot \bar{\varepsilon}_s \bar{t}_v - \frac{\partial \bar{\psi}_V}{\partial (\bar{\beta} \bar{U}_v)} : \bar{\beta} \bar{U}_v - \frac{\phi}{3(1-\phi)} \bar{\psi}_V \right] - \\ & \frac{\partial \bar{\psi}_V}{\partial (\bar{\varepsilon}_s \bar{t}_v)} \cdot \dot{\bar{\varepsilon}}_s \bar{t}_v - \frac{\partial \bar{\psi}_V}{\partial (\bar{\beta} \bar{U}_v)} : \dot{\bar{\beta}} \bar{U}_v - \frac{\partial \bar{\psi}_V}{\partial \bar{\nabla} \theta} \cdot \dot{\bar{\nabla}} \theta - \theta^{-1} \mathbf{q} \cdot \nabla \theta \geq 0. \end{aligned} \quad (3.49)$$

Using the Coleman and Gurtin (1967) framework, the thermodynamic conjugates of the ISVs associated with SSD and GND in the intermediate \mathbf{R}_3 configuration become:

$$\bar{\kappa}_V = \frac{\partial \bar{\psi}}{\partial (\bar{\varepsilon}_s \bar{\varepsilon}_v)} \bar{\varepsilon}_v, \quad (3.50)$$

$$\bar{\alpha}_V = \frac{\partial \bar{\psi}}{\partial (\bar{\beta} \bar{U}_v)} \bar{U}_v^T, \quad (3.51)$$

From Kratochvil and Dillon (1969) and modified by Francis *et al* (2014), the Piola Kirchoff stress tensor, entropy, and free energy due to the temperature gradient in the intermediate \mathbf{R}_3 configuration are posed as

$$\bar{\mathbf{S}}_3 = \frac{\partial \bar{\psi}}{\partial (\bar{\mathbf{E}}_v \bar{U}_v)} \bar{U}_v^T, \quad (3.52)$$

$$\bar{S}_v = f_\theta \bar{\mathbf{M}} : \mathbf{I} - \frac{\partial \bar{\psi}_v}{\partial \theta} - 3f_\theta \bar{\psi}_v, \quad (3.53)$$

$$\frac{\partial \bar{\psi}}{\partial \bar{\nabla} \theta} = 0. \quad (3.54)$$

Incorporating Eqs. (3.50)-(3.54) into Eq. (3.49) in the intermediate configuration \mathbf{R}_3 yields:

$$\begin{aligned} & \bar{\mathbf{M}} : \bar{\mathbf{D}}_d - \bar{\kappa}_V \dot{\bar{\varepsilon}}_s - \bar{\alpha}_V \dot{\bar{\beta}} - \theta^{-1} \mathbf{q} \cdot \nabla \theta + \left[f_\theta \bar{\mathbf{M}} : \mathbf{I} - \frac{\partial \bar{\psi}_v}{\partial \theta} - \bar{S}_v - 3f_\theta \bar{\psi}_v \right] \cdot \dot{\theta} + \\ & \frac{\phi}{3(1-\phi)} \left[\bar{\mathbf{S}}_3 : \bar{\mathbf{E}}_e + \bar{\mathbf{M}} : \mathbf{I} - \bar{\kappa}_V \cdot \bar{\varepsilon}_s - \bar{\alpha}_V : \bar{\beta} - \bar{\psi}_v \right] \geq 0. \end{aligned} \quad (3.55)$$

In Eq. (3.55), the initial term represents the energy added to a material system that contributes to plastic deformation in \mathbf{R}_3 . The second and third terms represent energy dissipated by generation and motion of statistically stored and geometrically necessary dislocations, respectively. The fourth term represents energy dissipated as heat flux in the

system. The bracketed collection of terms associated with $\dot{\theta}$ represent the coupled relationship of mechanical deformation, entropy, and free energy to temperature changes. The final bracketed term shows the coupled relationship of the applied mechanical stresses, plasticity ISVs, and free energy to damage. The expression for the Helmholtz free energy rate term (Eq. 48) can be simplified to:

$$\begin{aligned} \dot{\psi} = & \bar{\mathbf{S}}_3 : \dot{\bar{\mathbf{E}}}_e + \frac{\dot{\phi}}{3(1-\phi)} [\bar{\mathbf{S}}_3 : \bar{\mathbf{E}}_e + \bar{\kappa}_V \cdot \bar{\varepsilon}_s + \bar{\alpha}_V : \bar{\boldsymbol{\beta}}] + [f_\theta \bar{\mathbf{M}} : \mathbf{I} - \bar{S}_v - 3f_\theta \bar{\psi}_V] \cdot \dot{\theta} + \\ & \bar{\kappa}_V \dot{\bar{\varepsilon}}_s + \bar{\alpha}_V : \dot{\bar{\boldsymbol{\beta}}}. \end{aligned} \quad (3.56)$$

Combining Eq. (3.56) and the internal energy rate definition, Eq. (3.42), into the energy balance relation, Eq. (3.36), leads to:

$$\begin{aligned} -\bar{\mathbf{M}} : \bar{\mathbf{D}}_d + \frac{\dot{\phi}}{3(1-\phi)} [\bar{\mathbf{S}}_3 : \bar{\mathbf{E}}_e + \bar{\kappa}_V \cdot \bar{\varepsilon}_s + \bar{\alpha}_V : \bar{\boldsymbol{\beta}} + 3e_V - \bar{\mathbf{M}} : \mathbf{I}] + \dot{\theta} \cdot [3f_\theta \bar{e}_V - \\ 3f_\theta \bar{\psi}_V] + \bar{\kappa}_V \dot{\bar{\varepsilon}}_s + \bar{\alpha}_V : \dot{\bar{\boldsymbol{\beta}}} - \bar{r}_V + \nabla \cdot \mathbf{q} + \dot{s}_V \theta = 0. \end{aligned} \quad (3.57)$$

The time rate of change of temperature can be derived by isolating $\dot{\theta}$ in Eq. (3.58):

$$\begin{aligned} \dot{\theta} = \frac{1}{(3f_\theta \bar{e}_V - 3f_\theta \bar{\psi}_V)} \cdot \left(\bar{\mathbf{M}} : \bar{\mathbf{D}}_d - \frac{\dot{\phi}}{3(1-\phi)} [\bar{\mathbf{S}}_3 : \bar{\mathbf{E}}_e + \bar{\kappa}_V \cdot \bar{\varepsilon}_s + \bar{\alpha}_V : \bar{\boldsymbol{\beta}} + 3e_V - \bar{\mathbf{M}} : \mathbf{I}] - \right. \\ \left. \bar{\kappa}_V \dot{\bar{\varepsilon}}_s - \bar{\alpha}_V : \dot{\bar{\boldsymbol{\beta}}} + \bar{r}_V - \nabla \cdot \mathbf{q} - \dot{s}_V \theta \right). \end{aligned} \quad (3.58)$$

3.2.3 Kinetics: Plasticity

The constitutive relationship between stress and strain is posed as a function of strain rate stress state, and temperature for ductile materials in Horstemeyer and Gokhale (1999). The frame indifferent elastic stress rate was initially developed by Bammann (1990) as a function of kinematic tensors and elastic properties. This relation was extended by Horstemeyer and Ghokhale (1999) to capture the degradation of a material's effective stiffness by damage and is given in the R_d configuration as:

$$\underline{\dot{\sigma}} = \dot{\sigma} - W_e \sigma + \sigma W_e = \lambda(1 - \phi) \text{tr}(\mathbf{D}_e) \mathbf{I} + 2\mu(1 - \phi) \mathbf{D}_e - \frac{\dot{\phi}}{1 - \phi} \sigma. \quad (3.59)$$

where ϕ is the total damage, μ is the shear modulus, λ is Lamé's constant related to the bulk modulus and \mathbf{D}_e is the elastic rate of deformation. The elastic rate of deformation tensor, \mathbf{D}_e , is formulated as the difference between the total rate of deformation and the deviatoric, volumetric, and thermal rates of deformation tensors (\mathbf{D}_d , \mathbf{D}_v , and \mathbf{D}_θ),

$$\mathbf{D}_e = \mathbf{D} - \mathbf{D}_d - \mathbf{D}_v - \mathbf{D}_\theta. \quad (3.60)$$

The elastic spin tensor is formulated similarly to the elastic rate of deformation, however, due to the assumptions of isotropic damage, isotropic thermal deformation, and a Jaumann type spin ($\mathbf{W}_d = 0$), the elastic spin tensor becomes:

$$\mathbf{W}_e = \mathbf{W} - \mathbf{W}_d - \mathbf{W}_v - \mathbf{W}_\theta = \mathbf{W}, \quad (3.61)$$

An inelastic flow rule was initially developed by Bammann (1990) to relate the deviatoric rate of deformation to the applied stress and ISVs and was later revised to include the effects of damage by Horstemeyer and Gokhale (1999),

$$\mathbf{D}_d = \sqrt{\frac{3}{2}} f(\theta) \left[\frac{\sqrt{\frac{3}{2}} \|\boldsymbol{\sigma}' - \sqrt{\frac{2}{3}} \boldsymbol{\alpha}\| - (R + Y(\theta)(1 - \phi))}{V(\theta)(1 - \phi)} \right] \cdot \frac{\boldsymbol{\sigma}' - \sqrt{\frac{2}{3}} \boldsymbol{\alpha}}{\|\boldsymbol{\sigma}' - \sqrt{\frac{2}{3}} \boldsymbol{\alpha}\|}, \quad (3.62)$$

where $\boldsymbol{\sigma}'$ is the deviatoric part of the Cauchy stress tensor; $Y(\theta)$, $V(\theta)$, and $f(\theta)$ are variables related to strain rate and thermally dependent yield; and R and α are stress-like ISVs for isotropic and kinematic hardening, respectively. For the yield terms, $Y(\theta)$ controls the strain-rate independent, thermally dependent yield, $f(\theta)$ determines the threshold for strain-rate dependent yield, and $V(\theta)$ controls the magnitude of strain-rate dependent yield. Equations (64)-(66) control the thermal and strain-rate dependent yield stress:

$$V(\theta) = C_1 \exp(-C_2/\theta), \quad (3.63)$$

$$Y(\theta) = C_3 \exp(C_4/\theta), \quad (3.64)$$

$$f(\theta) = C_5 \exp(-C_6/\theta). \quad (3.65)$$

In Eqs. (3.63)-(3.65), C_1 , C_3 , and C_5 are stress-like calibration constants, and C_2 , C_4 , C_6 are Arrhenius type temperature dependent calibration constants. The kinematic hardening rate tensor, $\dot{\boldsymbol{\alpha}}$, and isotropic hardening rate scalar, \dot{R} , were developed in Bammann (1990) and modified by Tucker and Horstemeyer (2010) to account for grain size effects:

$$\begin{aligned} \dot{\boldsymbol{\alpha}} = \dot{\boldsymbol{\alpha}} - \mathbf{W}_e \boldsymbol{\alpha} + \boldsymbol{\alpha} \mathbf{W}_e = & \left(h(\theta) \mathbf{D}_d - \left[\sqrt{\frac{2}{3}} r_d(\theta) \|\mathbf{D}_d\| + \right. \right. \\ & \left. \left. r_s(\theta) \right] \sqrt{\frac{2}{3}} \|\boldsymbol{\alpha}\| \boldsymbol{\alpha} \right) (D_{CS0}/D_{CS})^z, \end{aligned} \quad (3.68)$$

$$\dot{R} = \left(H(\theta) \sqrt{2/3} \mathbf{D}_d - \left[\sqrt{2/3} R_d(\theta) \|\mathbf{D}_d\| + R_s(\theta) \right] R^2 \right) (DCS0/DCS)^Z. \quad (3.69)$$

In Eq. (3.68) and Eq. (3.69) $h(\theta)$ and $H(\theta)$ are thermally dependent moduli terms, $r_d(\theta)$ and $R_d(\theta)$ are thermally dependent dynamic recovery terms to account for the mobility of glide dislocations, and $r_s(\theta)$ and $R_s(\theta)$ are thermally dependent static recovery terms that account for relaxation due to dislocation climb mobility for kinematic and isotropic hardening, respectively. The static and dynamic recovery terms are posed as:

$$r_d(\theta) = \left[C_7 \left(1 - C_a \left[\frac{4}{27} - \frac{J_3^2}{J_2^3} \right] \right) - C_b \frac{J_3}{J_2^{3/2}} \right] \exp \left(-C_8/\theta \right), \quad (3.70)$$

$$r_s(\theta) = C_{11} \exp \left(-C_{12}/\theta \right), \quad (3.71)$$

$$h(\theta) = \left[C_9 \left(1 + C_a \left[\frac{4}{27} - \frac{J_3^2}{J_2^3} \right] \right) + C_b \frac{J_3}{J_2^{3/2}} \right] \exp \left(-C_{10}/\theta \right), \quad (3.72)$$

$$R_d(\theta) = \left[C_{13} \left(1 - C_a \left[\frac{4}{27} - \frac{J_3^2}{J_2^3} \right] \right) - C_b \frac{J_3}{J_2^{3/2}} \right] \exp \left(-C_{14}/\theta \right), \quad (3.73)$$

$$R_s(\theta) = C_{17} \exp \left(-C_{18}/\theta \right), \quad (3.74)$$

$$H(\theta) = \left[C_{15} \left(1 + C_a \left[\frac{4}{27} - \frac{J_3^2}{J_2^3} \right] \right) + C_b \frac{J_3}{J_2^{3/2}} \right] \exp \left(-C_{16}/\theta \right). \quad (3.75)$$

In Eqs. (3.72) and (3.75), C_9 and C_{15} are modulus-like calibration constants, C_a controls the shear dependence for hardening, and C_b distinguishes between the effects of tension and compression. C_7 and C_{13} in Eqs. (3.70) and (3.73) are modulus-like terms for dynamic recovery for kinematic and isotropic hardening. Similarly, C_{11} and C_{17} in Eqs. (3.71) and (3.74) are modulus like calibration constants for static recovery for kinematic

and isotropic hardening. Exponents C_8 and C_{12} control thermal sensitivity for dynamic and static recovery, respectively, related to kinematic hardening. Exponents C_{14} and C_{18} control the thermal sensitivity for dynamic and static recovery, respectively, for isotropic hardening.

Closed-form integration of the kinematic and isotropic hardening rate equations has been performed by Bammann (1990) assuming a constant strain rate, uniaxial isothermal deformation, and that the plastic strain rate may be approximated by the total strain-rate after yielding. The relations for the kinematic and isotropic hardening ISVs with grain size effect become:

$$\alpha = \sqrt{\frac{\|\dot{\mathbf{E}}\| h(\theta)}{\|\dot{\mathbf{E}}\| r_d(\theta) + r_s(\theta)}} \cdot \tanh \left[\|\mathbf{E}\| \cdot (DCS0/DCS)^Z \cdot \sqrt{\frac{\|\dot{\mathbf{E}}\| h(\theta) r_d(\theta) + h(\theta) r_s(\theta)}{\|\dot{\mathbf{E}}\|}} \right], \quad (3.76)$$

$$R = \frac{6^{1/4} \sqrt{\|\dot{\mathbf{E}}\|}}{\sqrt{\sqrt{6} \|\dot{\mathbf{E}}\| R_d + 3R_s}} \cdot \tanh \left[\frac{2^{1/4} \|\mathbf{E}\|}{3^{3/4}} \cdot (DCS0/DCS)^Z \cdot \sqrt{\frac{\|\dot{\mathbf{E}}\| H(\theta) R_d(\theta) + H R_s(\theta)}{\|\dot{\mathbf{E}}\|}} \right]. \quad (3.77)$$

3.2.4 Kinetics: Damage

Damage in ductile materials is documented in the literature as the combined effects of the nucleation, growth, and coalescence of voids (Puttick, 1959; Gangulee and Gurland, 1967; Lindley *et al.* 1970; Embry and Brown, 1973; Hancock and Mackenzie, 1976). Following the framework developed by Horstemeyer *et al.* (2000), damage (void volume fraction) in the intermediate \mathbf{R}_3 configuration is assumed through Horstemeyer *et al.* (2000) to take the form:

$$\dot{\phi} = \eta \nu c, \quad (3.78)$$

where η is the void nucleation, ν is the void growth, and c is the void coalescence. The time rate of change of the void volume fraction becomes:

$$\dot{\phi} = \dot{\eta} \nu c + \eta \dot{\nu} c + \eta \nu \dot{c}. \quad (3.79)$$

Here, the rate evolution for void nucleation is described by Horstemeyer (1999; 2000) as

$$\dot{\eta} = \frac{d^{1/2}}{Kicf^{1/3}} \eta \cdot \left(a \left[\frac{4}{27} - \frac{J_3^2}{J_2^3} \right] + b \frac{J_3}{J_2} + c \left\| \frac{I_1}{\sqrt{J_2}} \right\| \right) \| \mathbf{D}_d \| \exp \left(C_{\eta T} / T \right), \quad (3.80)$$

where d and f are material property constants representing the initial secondary phase particle size and volume fraction, respectively. Stress state dependence is mathematically accounted for using stress invariants I_1 , J_2 , and J_3 . Calibration constants a , and c are used to capture material's torsional and stress triaxiality sensitivity for void nucleation, respectively, and the constant b distinguishes between tensile and compressive stress states. The calibration constant $C_{\eta T}$ is used to control the thermal sensitivity for void nucleation.

The void nucleation parameter, η , may be determined by integrating Eq. (3.79) with respect to time. Following Bammann (1990) assuming constant strain rate, isothermal deformation, uniaxial stress, and the plastic rate of deformation closely approximates the total rate of deformation at finite strains, η may be expressed as

$$\eta = \eta_0 \exp \left[\| \mathbf{E} \| \cdot \frac{d^{1/2}}{f^{1/3}} \cdot \left(a \left[\frac{4}{27} - \frac{J_3^2}{J_2^3} \right] + b \frac{J_3}{J_2} + c \left\| \frac{I_1}{\sqrt{J_2}} \right\| \right) \exp \left(C_{\eta T} / T \right) \right]. \quad (3.81)$$

A hyperbolic function of triaxiality was developed in McClintock (1968) and utilized by Horstemeyer (2000) to describe the growth rate of voids nucleated from secondary phase particles,

$$\dot{v} = \frac{4\pi}{3} \left(\frac{\sqrt{3}d_{v0}}{4(1-n)} \left[\sinh \left(\sqrt{3}(1-n) \frac{\sqrt{2}I_1}{3\sqrt{J_2}} \right) \right] \|\mathbf{D}_d\| \right)^3, \quad (3.82)$$

where d_{v0} represents the initial void diameter, and n is the McClintock growth rate constant originally motivated by the material hardening rate. Similarly, the hyperbolic growth rate of pre-existing voids and pores as a function of triaxiality has been postulated by Cocks and Ashby (1982) and implemented by Horstemeyer (2000) as the following,

$$\dot{\phi}_{pores} = \left[\frac{1}{(1-\phi_{pore})^m} - (1 - \phi_{pore}) \right] \sinh \left[\frac{(2V(T)/Y(T))-1}{(2V(T)/Y(T))+1} \cdot \frac{I_1}{3\sqrt{J_2}} \right] \|\mathbf{D}_d\|, \quad (3.83)$$

where Bammann *et al.* (1993) showed that $m = V(T)/Y(T)$ is a strain rate sensitivity material parameter. The preceding Eqs. (3.82-83) capture the hyperbolic correlation between void growth and stress-state triaxiality; however, void and crack evolution due to shear are not sufficiently accounted for. In the current form, the void growth relations given in Eqs. (3.82-83) may significantly underpredict void growth in shear dominated stress states. This issue is one of the primary focuses of the current work.

The implementation of the J_3 deviatoric stress invariant in constitutive modeling has roots in the J_2/J_3 based yield surface theory proposed by Drucker (1949; 1950). Until Bao and Wierzbicki (2004A; B) discussed the inadequacies of numerous prevalent fracture criteria, J_3 theory was used sparingly damage modeling. Bai and Wierzbicki (2008) used lode angle theory to describe a fracture strain surface whose shape is a function of the J_3

deviatoric stress invariant. Nashon and Hutchinson (2008) used the J_3 deviatoric stress invariant based lode parameter to account for shear-based damage within a Gurson (1977) void volume fraction evolutionary framework,

$$\dot{f} = (1 - f)\mathbf{D}_{kk}^d + Kf\omega(\boldsymbol{\sigma}) \frac{\mathbf{D}_{ij}^d:\boldsymbol{\sigma}'_{ij}}{\sqrt{3J_2}}, \quad (3.84)$$

where f is the void volume fraction, \mathbf{d}^d is the deviatoric component of the rate of deformation tensor, K is a shear sensitivity coefficient, $f\omega(\boldsymbol{\sigma})$ is a Lode angle function, $\boldsymbol{\sigma}'_{ij}$ is the deviatoric part of the Cauchy stress tensor, and J_2 is the second deviatoric stress invariant. where the Lode angle term is formulated as

$$\omega(\boldsymbol{\sigma}) = 1 - \left(\frac{27J_3}{2(3J_2)^{3/2}} \right)^2. \quad (3.85)$$

Combining the Lode angle dependence (Eq. 3.85) with void and pore growth equations (Eqs. 3.82-83) gives the yields Eqs. (3.86) and (3.87),

$$\dot{v} = \frac{4\pi}{3} \left(\frac{\sqrt{3}d_{v0}}{4(1-n)} \left[\sinh \left(\sqrt{3}(1-n) \frac{\sqrt{2}I_1}{3\sqrt{J_2}} \right) \right] \|\mathbf{D}_d\| + \frac{1}{2}K_{void}d_0 \left[1 - \left(\frac{27J_3}{2(3J_2)^{3/2}} \right)^2 \right] \frac{\mathbf{D}_{ij}^d:\boldsymbol{\sigma}'_{ij}}{\sqrt{3J_2}} \right)^3, \quad (3.86)$$

$$\dot{\phi}_{pores} = \left[\frac{1}{(1-\phi_{pore})^m} - (1 - \phi_{pore}) \right] \cdot \left(\sinh \left[\frac{(2V(T)/Y(T))-1}{(2V(T)/Y(T))+1} \cdot \frac{I_1}{\sqrt{3J_2}} \right] \|\mathbf{D}_d\| + K_{pore} \left[1 - \left(\frac{27J_3}{2(3J_2)^{3/2}} \right)^2 \right] \frac{\mathbf{D}_{ij}^d:\boldsymbol{\sigma}'_{ij}}{\sqrt{3J_2}} \right). \quad (3.87)$$

An analytical form of the size of voids nucleated from microstructural heterogeneities with shear dependence is derived by integrating Eq. (3.86) with respect to time assuming from Bammann (1990) that the plastic strain approximates the total strain at large strains,

$$v = \left(\frac{4\pi}{24} d_{v0}^3\right) \cdot \exp \left[\|\mathbf{E}\| \left\{ \left(\frac{\sqrt{3}}{2(1-n)} \left[\sinh \left(\sqrt{3}(1-n) \frac{\sqrt{2}I_1}{3\sqrt{J_2}} \right) \right] \right)^3 + \left(K_{void} \left[1 - \left(\frac{27J_3}{2(3J_2)^{3/2}} \right)^2 \right] \frac{D_{ij}^d \cdot \sigma'_{ij}}{\sqrt{3}J_2} \right)^3 \right\} \right]. \quad (3.88)$$

where \mathbf{E} is the total Green-Lagrange strain tensor. Similarly, the pore growth rate equation in Eq. (3.87) is integrated with respect to time to formulate the relationship between pore volume fraction and strain. Eq. (3.87) cannot be integrated analytically, therefore a forward Euler numerical approximation approach is used to formulate the relationship between the pore volume fraction and total strain increments for a given time increment,

$$\phi_{pore}^{n+1} = \phi_{pore}^n + \left[\frac{1}{(1-\phi_{pore}^n)^m} - (1 - \phi_{pore}^n) \right] \cdot \left(\sinh \left[\frac{(2V(T)/Y(T))-1}{(2V(T)/Y(T))+1} \frac{I_1}{\sqrt{3}J_2} \right] \|\Delta\mathbf{E}\| + K_{pore} \left[1 - \left(\frac{27J_3}{2(3J_2)^{3/2}} \right)^2 \right] \frac{\|\Delta\mathbf{E}\| \cdot \|\sigma'\|}{\sqrt{3}J_2} \right), \quad (3.89)$$

where $\Delta\mathbf{E}$ is the Green-Lagrange strain tensor increment, n is the current time increment, and $n+1$ is the future time increment in the forward Euler integration scheme.

Voids often coalesce through interaction of stress fields due to neighboring voids. Interacting voids coalesce via sheeting (Cottrell, 1959) and/or impingement (Brown and

Embery, 1973) mechanisms. Void coalescence has been formulated as a function of nucleation and growth of voids by Tucker and Horstemeyer (2010):

$$\dot{C} = [c_{d1} + c_{d2}(\eta\dot{\nu} + \eta\nu)]\exp^{(C_{CT}T)}(DCS_0/DCS)^Z, \quad (3.90)$$

where c_{d1} and c_{d2} are calibration constants, GS_0 (reference grain size) and GS (recrystallized grain size) capture the effects of grain growth on void coalescence, Z determines the magnitude of grain growth sensitivity, and C_{CT} is a calibration constant for thermal sensitivity for void coalescence. The ISV representing void coalescence was formulated as a function of the nearest neighbor distance of voids by Allison (2009)

$$\dot{C} = TC \left(\frac{4d_{v0}}{NND} \right)^\zeta \dot{\epsilon}. \quad (3.91)$$

In Eq. (3.91), NND represents the center to center void nearest neighbor distance, ζ is a calibration constant controlling the coalescence rate dependence on the nearest neighbor distance, and the critical Intervoid Ligament Distance (ILD) (Horstemeyer *et al.* 2000B) is an integer multiple of the average void diameter, d_{v0} . In Allison's formulation void coalescence exponentially increases as the nearest neighbor distance approaches the critical ILD ($4 \cdot d_0$).

The current study aims to capture a combination of the nearest neighbor distance, thermal, and grain size dependence on the void coalescence rate. The ILD has been shown in the literature to significantly influence the growth rate of neighboring voids (Bourcier and Koss, 1979; Horstemeyer *et al.* 2000B) versus the growth rate of noninteracting voids. The ILD in may be expressed as a function of the NND and average void diameter,

$$ILD = NND - 2d_v, \quad (3.92)$$

where the average current individual void diameter is assumed to be

$$d_v = \left(\frac{6v}{\pi}\right)^{1/3}. \quad (3.93)$$

Logically, the average NND decreases with the continued nucleation of voids. Consider a material that nucleates voids in such a fashion that all voids share an equal distance with their respective nearest neighbors at regularly observed void number density intervals. Figure 3.2 shows a two-dimensional conceptual representation of the void NND (defined as the distance between void center points) evolution for the increasing relative void number densities of (a) $\eta = \eta_0$, (b) $\eta = 2\eta_0$, and (c) $\eta = 4.5\eta_0$. In Fig. 3.2 a-c NND_0 and η_0 represent the initial void nearest neighbor distance and number density, respectively.

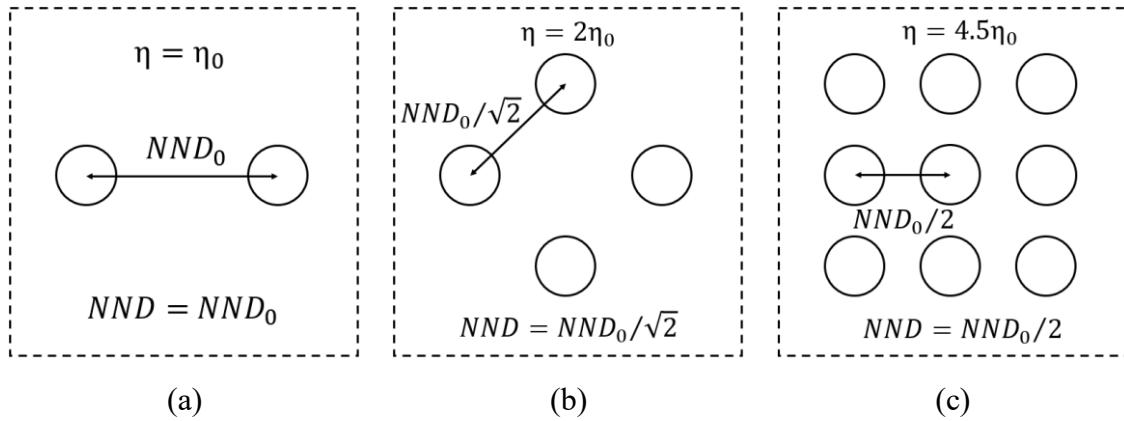


Figure 3.2 Effect of void number density on Nearest Neighbor Distance (NND).

Figure 3.2 demonstrates that the Nearest Neighbor Distance (NND) can be formulated through an inverse relationship to the square root of the number of nucleated voids. The assumed functional form of the NND equation is also motivated by the Hall-

Petch (Hall, 1951; Petch, 1953) length scale equation, which correlates plasticity (yield) to the square root of grain size,

$$NND = \frac{0.554}{\sqrt{\eta}}. \quad (3.94)$$

where the numerical term, 0.554, was derived in the Hertz (1909) and Chandrasekhar (1943) studies of percolation of randomly nucleating spheres. Thus, the current ILD becomes

$$ILD = \frac{0.554}{\sqrt{\eta}} - 2d_{void}, \quad (3.95)$$

where η represents the void number density, and d_{void} represents the current average void diameter. A coalescence rate equation is motivated by a combination from that of Horstemeyer *et al.* (2000A), Tucker and Horstemeyer (2010), and Allison *et al.* (2011),

$$\dot{C} = (T \cdot C_{CT}) C \left(\frac{4d_v}{ILD} \right)^\zeta \cdot \left(GS_0 / GS \right)^Z \cdot \|D_d\|, \quad (3.96)$$

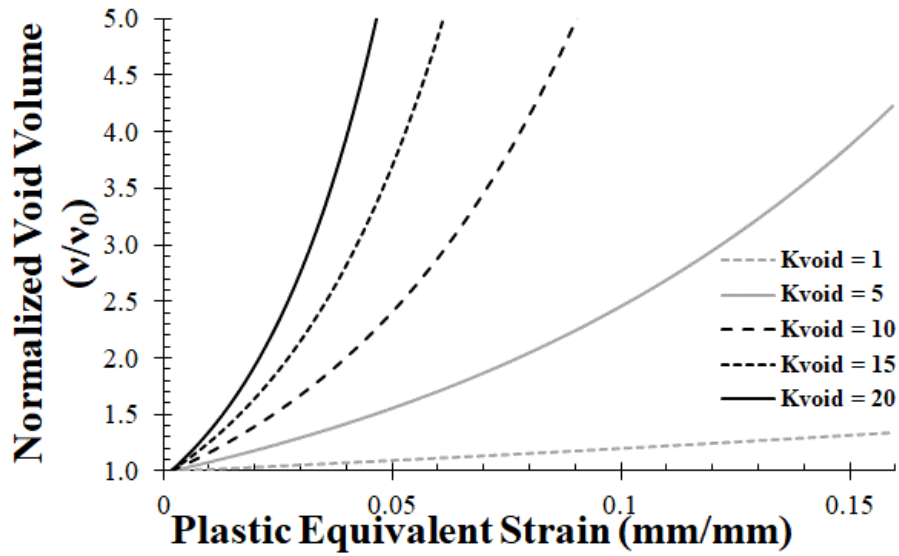
where T is the temperature, C_{CT} captures void coalescence temperature sensitivity, d_{void} is the current void diameter, ζ is a neighbor distance sensitivity exponent, GS_0 and GS are reference and current grain size terms, and Z is a grain size sensitivity exponent. The expression for the coalescence rate in Eq. (3.96) can be integrated with respect to time to derive the void coalescence as a function of strain:

$$C = C_0 \exp \left(\|E\| \left(\frac{4d_v}{ILD} \right)^\zeta \cdot \left(GS_0 / GS \right)^Z \cdot (C_{CT} T) \right). \quad (3.97)$$

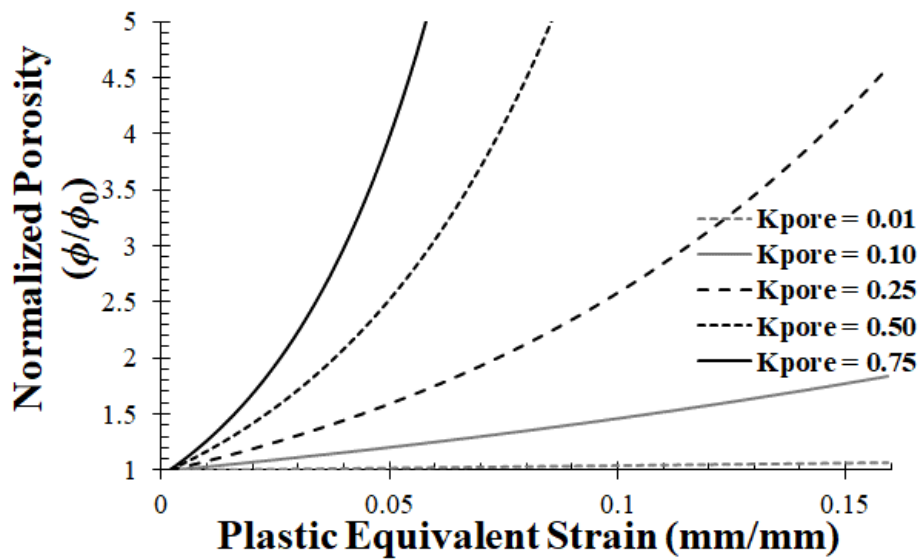
3.3 Implementation

3.3.1 Void Growth

The shear dependent evolution equations for nucleated and pre-existing voids (Eqs. 3.88 and 3.89, respectively) have been implemented into an ISV model framework to determine the effect of the shear sensitivity terms. A Representative Volume Element (RVE) of an Al 7085-T711 is subjected to a pure torsional stress-strain state and the mean nucleated void radius and pre-existing void volume fraction are calculated. Figures 3.3a and 3.3b show the normalized mean void volume and pore volume fractions versus plastic equivalent strain for varying values of the shear sensitivity coefficients K_{void} and K_{pore} , respectively. The void radius and void volume fraction increase exponentially as the sensitivity coefficients increase. Hence, K_{void} and K_{pore} effectively reflect the reduction of ductility of the material subjected to shearing.



(a)



(b)

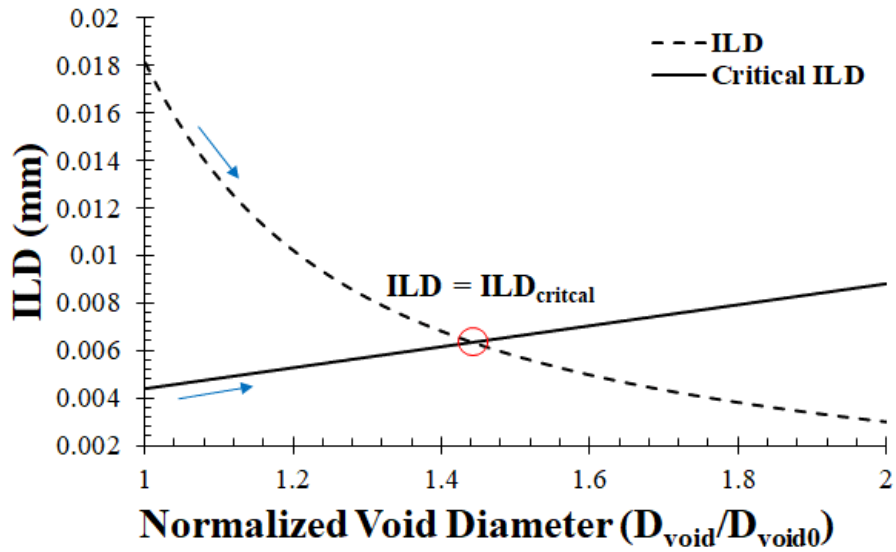
Figure 3.3 Shear sensitivity parameter effects on ISV model predicted void growth rates.

(a) Normalized void growth versus plastic equivalent strain.

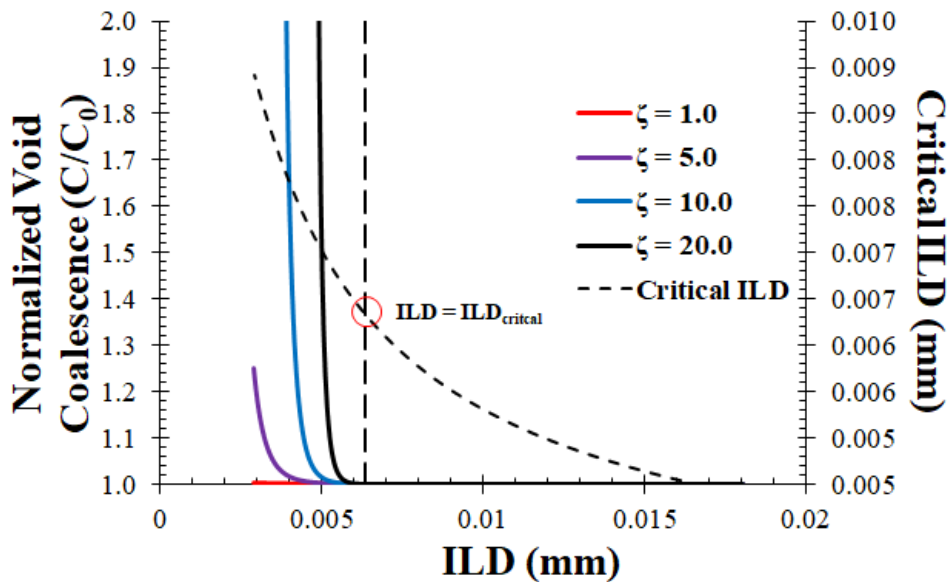
(b) Normalized pore growth versus plastic equivalent strain.

3.3.2 Void Coalescence

The evolving ILD-based coalescence equation, Eq. (3.97), has been evaluated using an Abaqus simulation of a single Representative Volume Element (RVE) under tension in conjunction with a calibrated ISV model for Al 7085-T711. The ISV model coefficients for Al 7085-T711 are listed in Table A1 in Appendix A. The current ILD (given by Eq. 3.95) and critical ILD (defined as four void diameters in Horstemeyer *et al.* 2000B) versus evolving void size is shown in Fig. 3.4a. The normalized void coalescence effect (given by Eq. 3.97) versus evolving ILD is shown in Fig. 3.4b. In Fig. 3.4a the critical ILD increases as the average void size increases because larger voids produce larger stress fields for potential interaction. Conversely, as the average void size increases the current average ILD decreases. The intersection point of critical and current ILD triggers an exponential increase in the void coalescence effect, predicted by Eq. (3.97) (Fig. 3.4-b). This is taken to represent the condition during the physical deformation when voids begin to coalesce together by sheeting or impingement mechanisms. For the Al 7085-T711 material, the average ILD value that leads to void coalescence is approximately 6.34 μm . Figure 3.4-b shows that increasing the ILD sensitivity parameter, ζ , moves the inflection point of the void coalescence curve closer to the critical ILD.



(a)



(b)

Figure 3.4 ISV model predicted intervoid ligament distance (ILD) based void coalescence characteristics.

- (a) Critical (4 void diameters) and current ILD evolution with increasing void radius.
- (b) Normalized coalescence evolution as a function of ILD.

3.3.3 ISV Damage Model Validation

The shear influenced void and pore growth equations (Eq. 3.88 and 3.89; rates given by Eq. 3.86 and 3.87) and void coalescence equations (Eq. 3.97; rate given by Eq. 3.96) have been validated using FEA simulations of complex stress state mechanical experiments. The shear dependent void growth ISVs have been validated using two test cases. Similar to the void coalescence studies of Bourcier and Koss (1979), flat dog-bone specimens were used to validate the shear influenced damage relation. Figure 3.5 shows the Dog Bone Shear Concentration (DBSC) sample geometry which features a pair of holes of 1 mm diameter holes spaced five diameters apart oriented 45° with respect to the tensile loading directions. Specimens were deformed under quasi-static tensile conditions until fracture using an Instron 5882 load-frame. Specimen gauge section extension was measured using an Instron 25 mm extensometer.

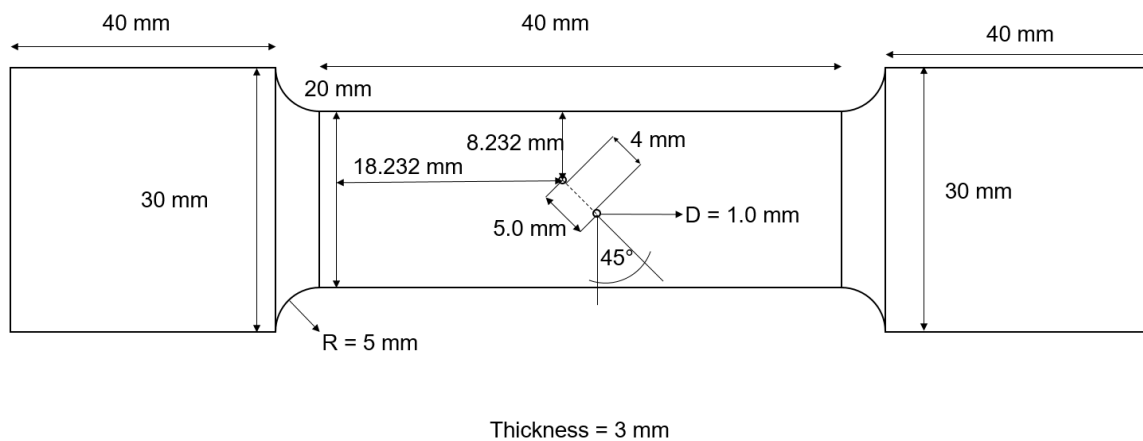


Figure 3.5 Schematic of Dog Bone Shear Concentration (DBSC) specimen used for validation of shear stress dependent void growth model.

Bourcier and Koss (1979) demonstrated that the complex strain state between the holes becomes dominated by shear strain as the angle of the holes approaches 45°. An ISV constitutive model for an Al 7085-T711 alloy developed in (Peterson *et al.* 2019) was used in an Abaqus Implicit FEA simulation of the deformation two-hole tension specimens. The specimen FE mesh consisted of approximately 70,000 linear hexahedral reduced integration (C3D8R) elements.

A comparison of the predicted and experimental load-extension behavior for the DBSC specimens is shown in Fig. 3.6. The DBSC experiments demonstrated an initial fracture of the interhole ligament followed by separate secondary fractures of the remaining edge ligaments resulting in distinguishable drops in the load-extension behavior of the specimens (Fig. 3.6). ISV model predictions predict continuous fracture evolution following the fracture of the interhole ligament resulting in a continuous decrease in load following initial localization.

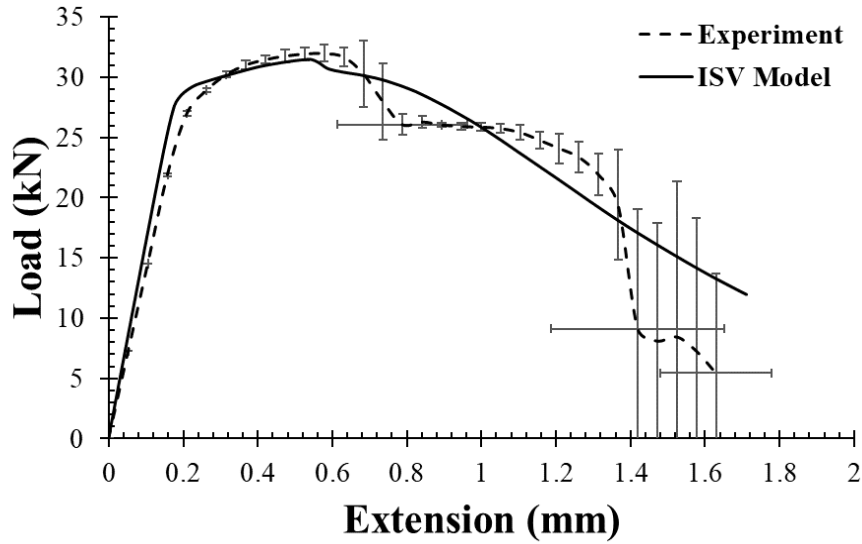


Figure 3.6 Comparison of predicted and observed load-extension behavior for Dog Bone Shear Concentration (DBSC) specimens.

The measured and predicted void number density, coalesced radius, and volume fraction in the ligament between the holes were used as properties for ISV model validation. The void morphology present in fractured interhole region of DBSC specimens was observed using a Zeiss Field Emission Gun (FEG) Scanning Electron Microscope (SEM). Void properties were quantified from electron micrographs using the ImageJ Digital Image Correlation (DIC) software (Abramoff *et al.* 2004). Figure 3.7 shows the void morphology in the central ligament of the DBSC fracture surface. Figure 3.7 shows networks of numerous, small voids which have nucleated around secondary phase particles and are interspersed among cleavage fracture regions.

Void properties from FEA simulations were quantified as the average value of void number density, η , coalesced void diameter, $d_{void} \cdot C$, and area fraction, ϕ , state variables of

elements between specimen holes. Figure 3.8 compares the predicted and observed void number density, coalesced radius, and area fraction for fractured DBSC specimens. In general, the ISV model overpredicted the evolutionary rates of damage with extension. However, Fig. 3.8 shows that the model predictions for void property values at fracture agree with the respective experimentally observed quantities. Specifically, the predicted average void number density (14595 voids/mm² predicted, 13997±1164 voids/mm² observed) and coalesced void diameter (6.0 μm predicted, 5.73±0.74 observed) fall within experimentally observed 95% confidence intervals while the predicted final void area fraction (0.4) exceeds the experimentally observed 0.36±0.17 area fraction by approximately 10%.

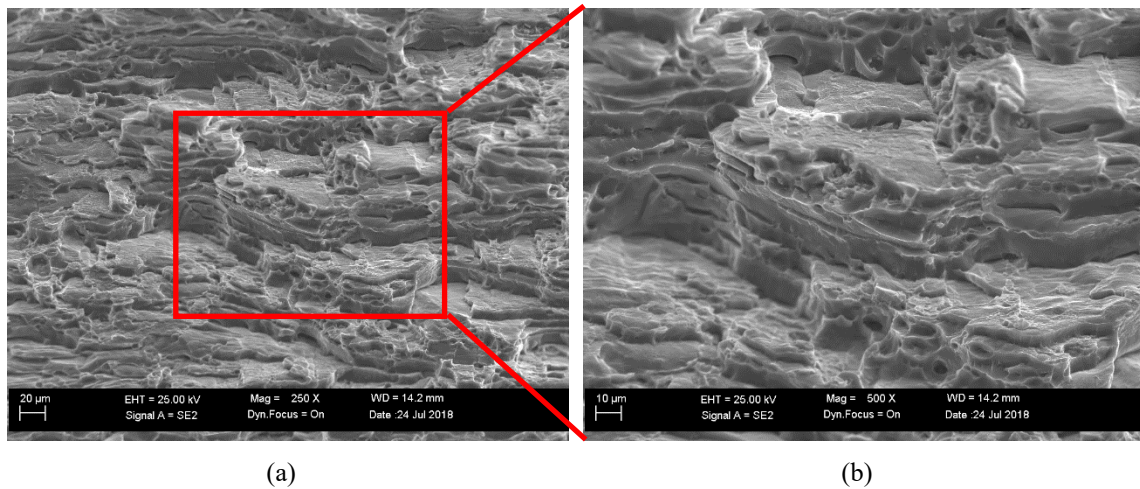
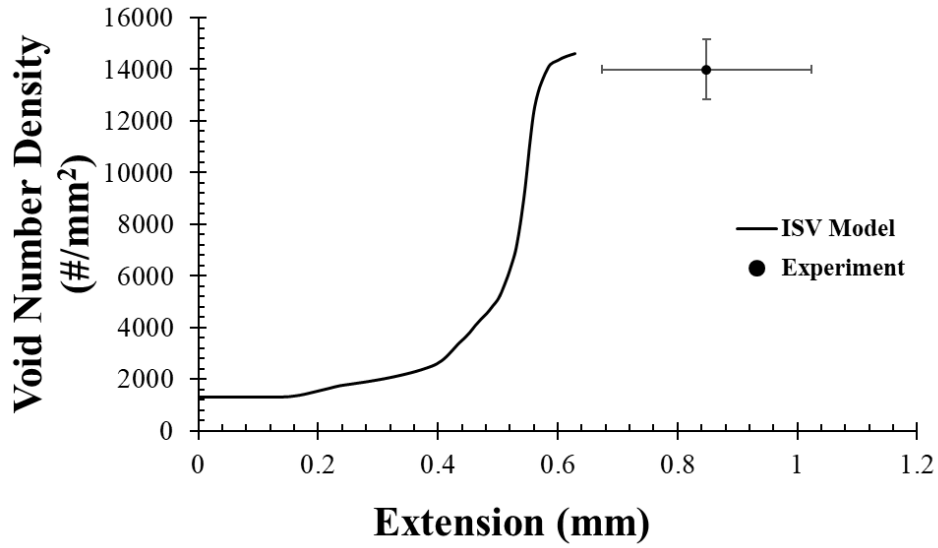
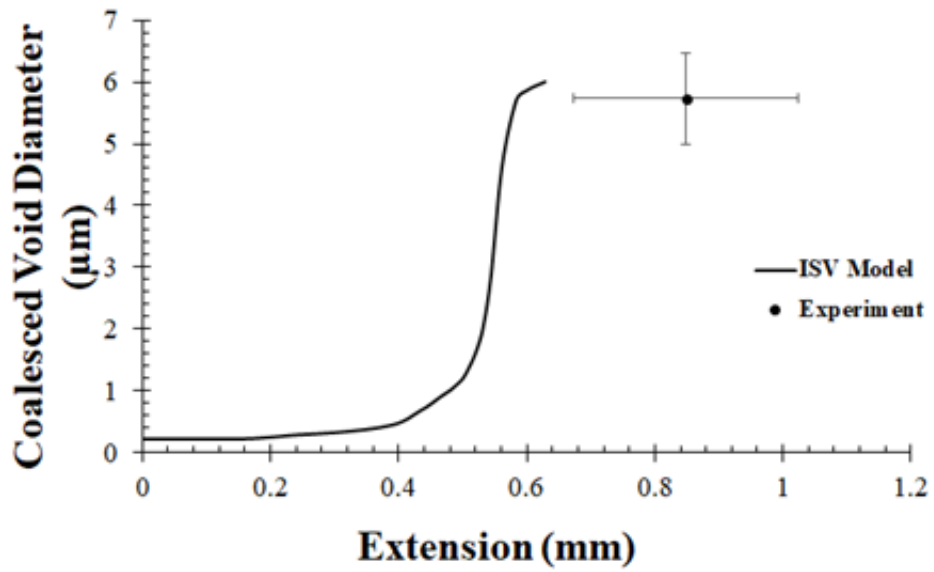


Figure 3.7 Electron micrographs of Dog Bone Shear Concentration (DBSC) fracture surface.

- (a) Fracture surface micrograph.
- (b) Initiation of voids around second phase Fe-Cu particles.

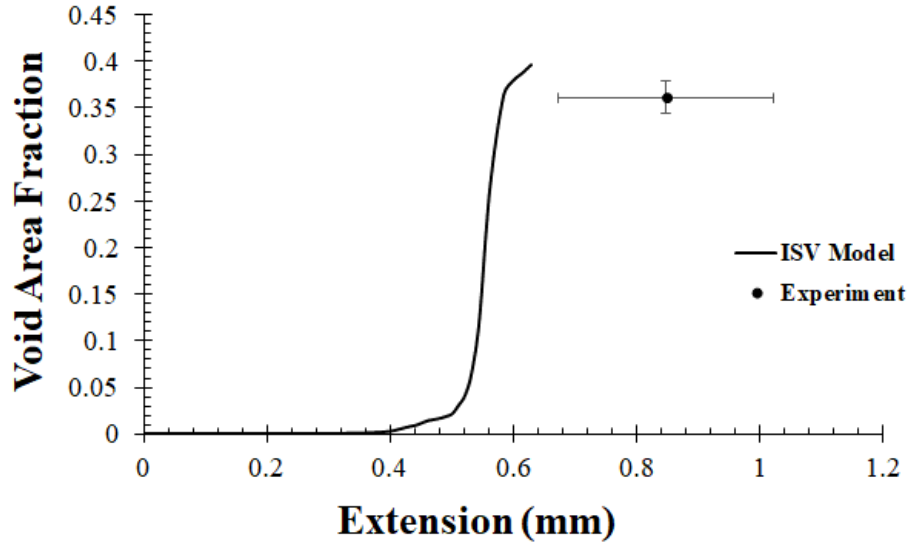


(a)



(b)

Figure 3.8 Comparison of predicted and observed void evolution characteristics for fractured Dog Bone Shear Concentration (DBSC) specimens.



(c)

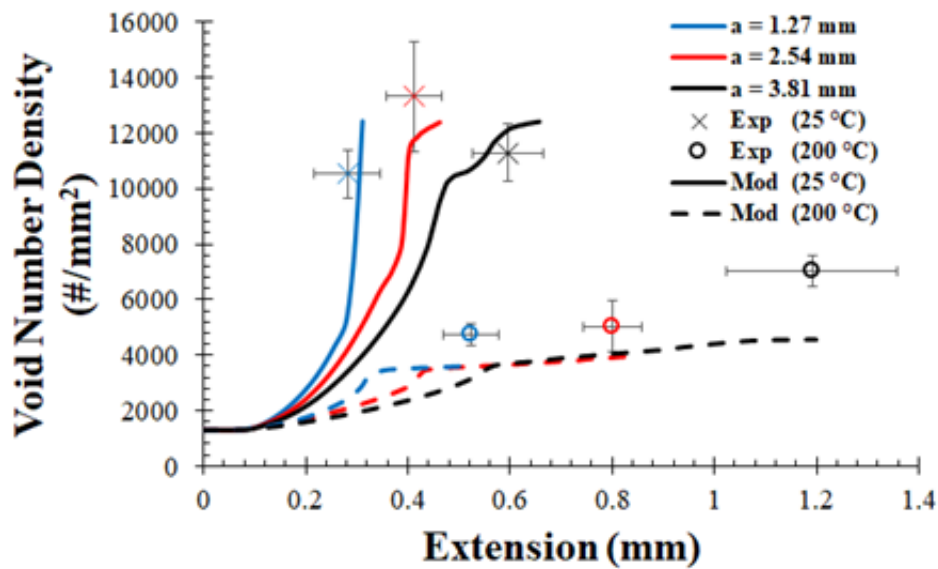
Figure 3.8 (continued)

- (a) Comparison of experimental and model predicted void nucleation for DBSC specimens.
 (b) Comparison of experimental and model predicted void radius for DBSC specimens.
 (c) Comparison of experimental and model predicted void area fraction for DBSC specimens.

3.3.4 Bridgman Notch Tension Specimen Modeling

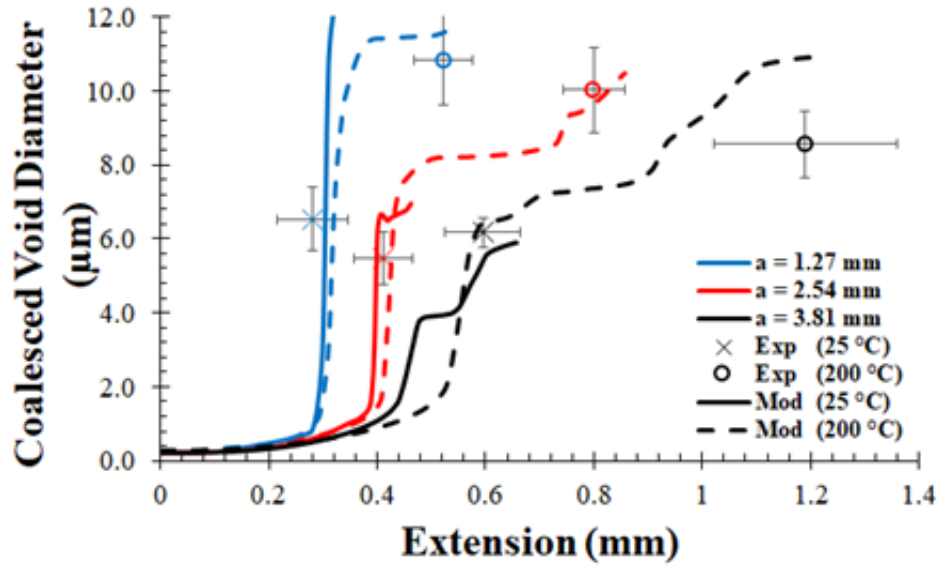
A series of Bridgman (1923, 1944) notched tension specimens featuring varying notch radii of 1.27, 2.54, and 3.81 mm were modeled to study the effects of varying stress states and temperatures on damage evolution. Bridgman (1944) demonstrated that as the notch radius (a) decreased relative to the notch cross sectional area (r), the degree of stress triaxiality in the specimen notch increased. Studies of damage evolution in ductile materials have shown a strong correlation between void growth rates and stress triaxiality (McClintock, 1968; Rice and Tracey, 1969; Gurson, 1977). Figure 3.9 compares the predicted and observed void number density, coalesced radius, and area fraction as a

function of specimen extension and temperature for varying notch radii. Figure 3.9 shows that the void nucleation and growth rates increase significantly with decreasing notch root radius and subsequently increasing the stress triaxiality. Figure 3.9 shows that the void nucleation rate sharply decreases, and the void growth rate slightly decreases for deformation at 200°C compared to 25°C. The result is that the total damage evolution rate decreases appreciably and leads to higher failure strains at elevated temperatures.

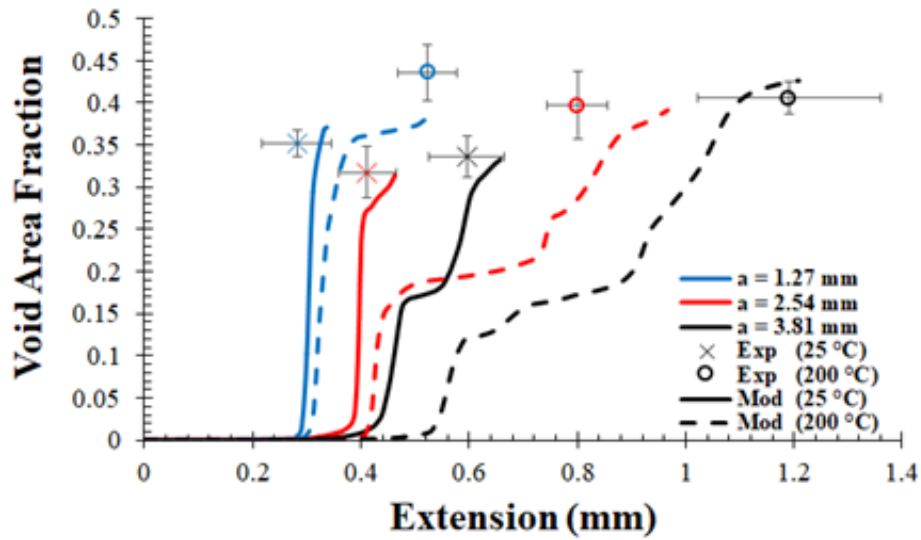


(a)

Figure 3.9 Comparison of predicted and observed void property evolution for Bridgman notched tension specimens deformed at varying stress states and temperatures



(b)



(c)

Figure 3.9 (continued)

- (a) Comparison of experimental and predicted void nucleation.
- (b) Comparison of experimental and predicted coalesced void diameter.
- (c) Comparison of experimental and predicted void area fraction

The notched tension specimen FEA model damage contours were compared to fracture surface micrographs generated using the FEG SEM. Figure 3.10a-10c contain a qualitative comparison of the model predicted damage (ϕ) contours and the physical fracture surface morphologies for the Bridgman tensile specimens with notch radii (a) 1.27, (b) 2.54, and (c) 3.81 inches, respectively. Physical specimens show an increase in the fracture surface area dominated by void evolution and subsequent decrease in shear influenced damage regions with increasing stress triaxiality. Qualitatively, the FEA model predicts a similar increase in area of the triaxiality dominated core of the fracture surface and the diminishing of shear influenced regions with increasing stress triaxiality levels.

The current ISV model framework is the first to be able to predict both shear and triaxiality influenced void growth. For example, Fig 3.11a shows FE predictions of void damage evolution in tensile Bridgman specimens by Bammann *et al.* 1993 using the BCJ model and a Cocks-Ashby (1982) void growth rule. Because the BCJ model only considers triaxiality stress state effects, damage progression (*i.e.*, flat fracture) is restricted to a plane perpendicular to the applied load. In contrast, the current ISV model (using Lode-angle dependent McClintock, 1968, and Cocks-Ashby, 1982, void growth rules) predicts planar damage at the center of the specimen that depends on the degree of constraint (triaxiality) along with shear dominated fracture near the specimen edges (Fig. 3.11b).

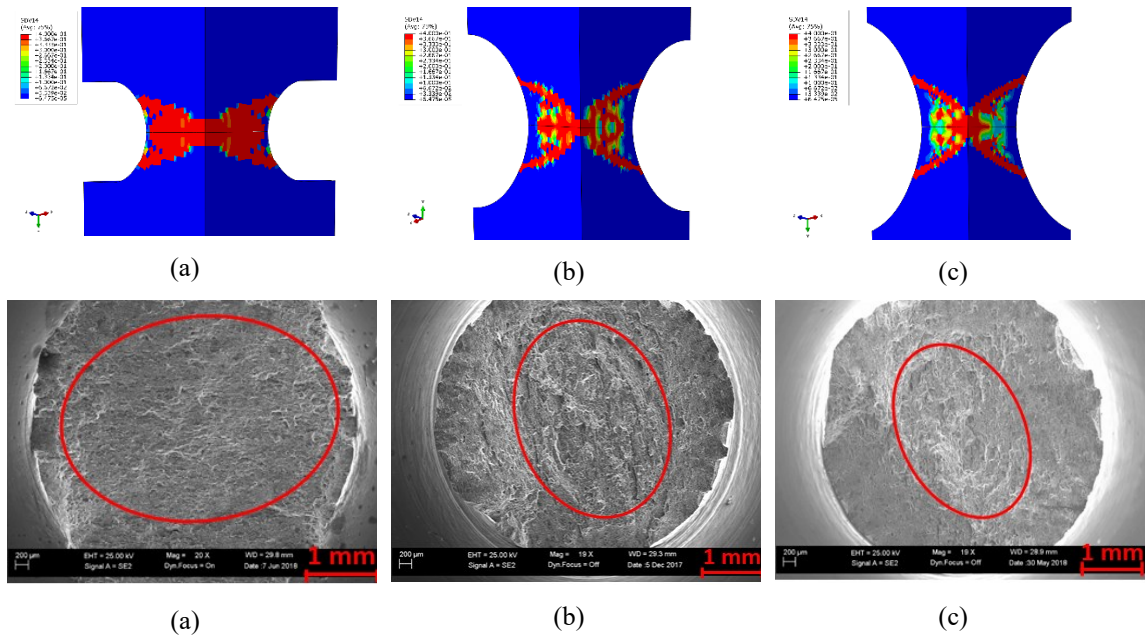


Figure 3.10 Comparison of Finite Element Analysis (FEA) predicted damage evolution and electron micrographs of experimental fracture surfaces for varying notch radii.

- (a) 1.27 mm notch root radius.
- (b) 2.54 mm notch root radius.
- (c) 3.81 mm notch root radius.

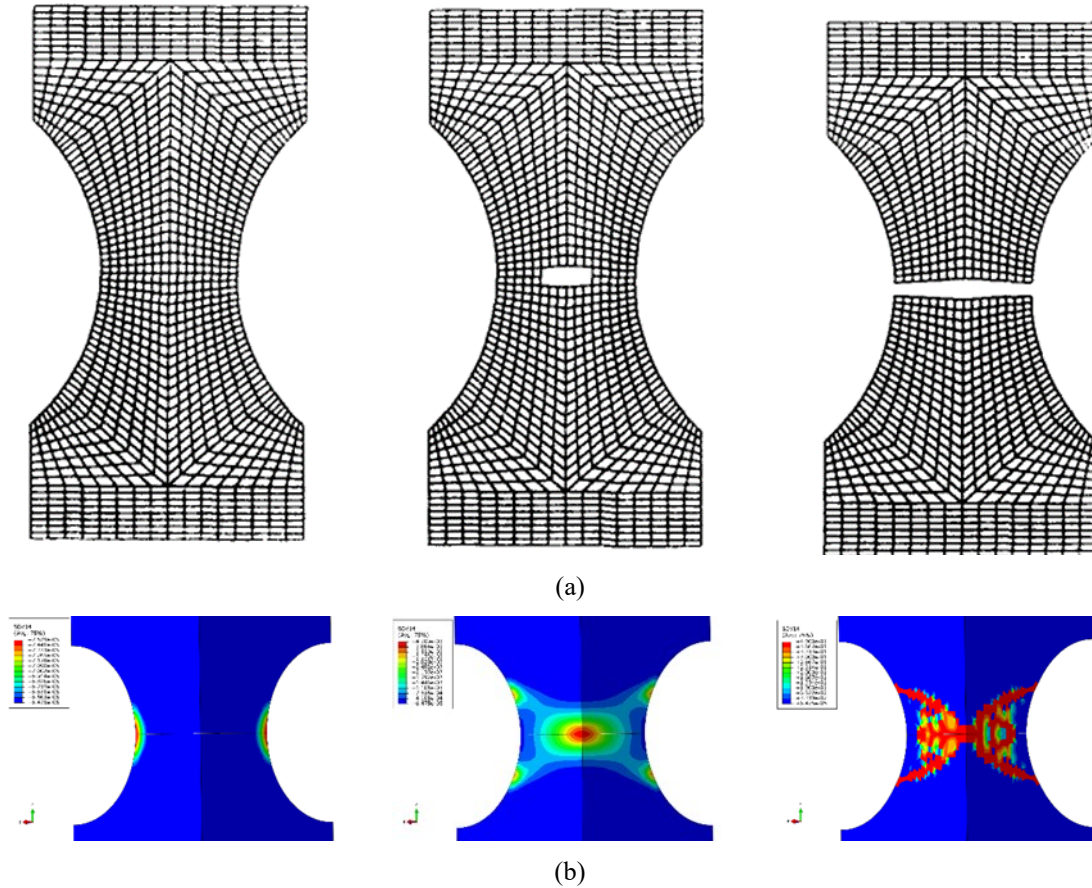


Figure 3.11 Finite element predicted damage evolution in Bridgman notch tension specimens.

(a) BCJ model damage model predicted damage evolution (Bammann *et al.* 1993).

(b) ISV plasticity-damage model predicted damage evolution.

3.3.5 Notch Tension Specimen Damage Evolution for a Heterogeneous Microstructure

FEA simulations using material models predicated upon homogeneous property distributions tend to predict symmetric contours for deformation, localization, and damage (*cf.*, Fig. 3.11). Asymmetry in otherwise symmetric state variable contours can be attributed to numerical error, mesh irregularities, and mesh dependence. Physical phenomena such as the cup-cone fracture cannot be predicted by most models due to the

absence of such irregularities or heterogeneities. Most boundary value problems simulations using a physically-motivated ISV model have been performed assuming a homogeneous distribution of microstructure properties (Bammann *et al.* 1993; Bammann *et al.* 1996; Horstemeyer and Ramaswamy, 2000; Fang *et al.* 2005; Horstemeyer *et al.* 2009; Crapps *et al.* 2010; Whittington *et al.* 2014). In practice, damage initiates at and propagates from microstructural heterogeneities in metal alloys (Puttick, 1959; Gangulee and Gurland, 1967; Lindley *et al.* 1970; Embry and Brown, 1973; Hancock and Mackenzie, 1976) and heterogeneous distributions of microstructural features can significantly influence the path and rate of damage progression in addition to structural geometry.

The microstructure properties of an Al 7085-T711 alloy have been quantified in another study (Peterson *et al.* 2019) and were used to calibrate an ISV model for use in FEA simulations. Two microstructure properties – initial second phase particle number density (η_0) and initial void diameter (D_0) – were each assumed to vary stochastically within the domain of a full length, quarter symmetric FE model of a Bridgman notch tension specimen with notch radius, 2.54 mm. The initial particle number density and void diameter were selected for this study because they are physical properties corresponding to the initial values of the void nucleation and growth ISV relations in Eq. 3.81 and 3.88, respectively. The initial second phase particle number density was randomly sampled from Gaussian distributions with sample means of 1300 and 1560 particles/mm² (standard deviation of ± 130) for regions (a) and (b) of the specimen respectively, (Fig. 3.12). Similarly, the initial void radius was randomly sampled from exponential distributions with sample means of 1.1 and 1.2 μm for regions (a) and (b). A velocity of 0.01 mm/s was

applied to a grip section base to deform the specimen. The specimen's opposite base was fixed in the axial direction but allowed to radially expand or contract to accommodate the Poisson's effect. In this study, the microstructure property distributions and their respective stochastically determined locations are idealizations selected to model the asymmetric "cup-cone" fracture behavior that is commonly observed in mechanical experiments. Traditional constitutive models operating under homogeneous material assumptions fail to predict this fracture mode (Bammann *et al.* 1993).

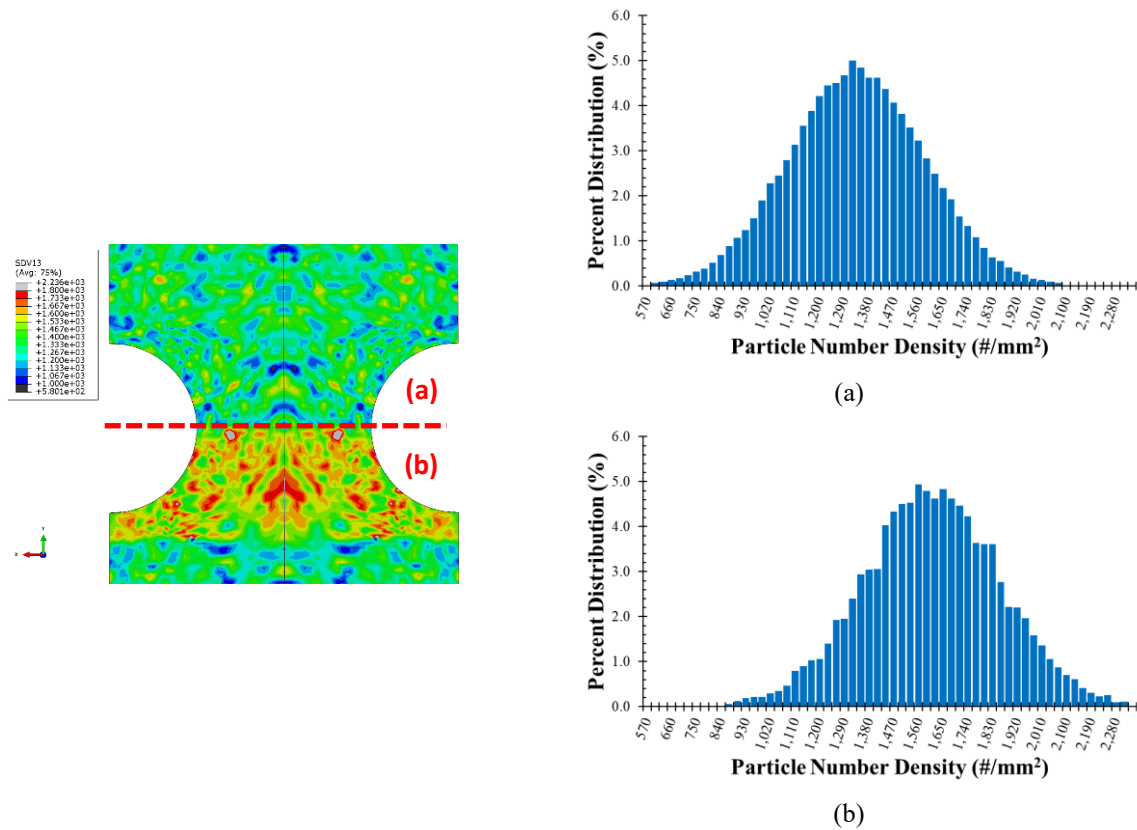


Figure 3.12 Heterogeneous initial particle number density distribution in an Al 7085-T711 notch tension specimen.

- (a) Particle number density distribution in region (a) of Bridgman specimen.
- (b) Particle number density distribution in region (b) of Bridgman specimen.

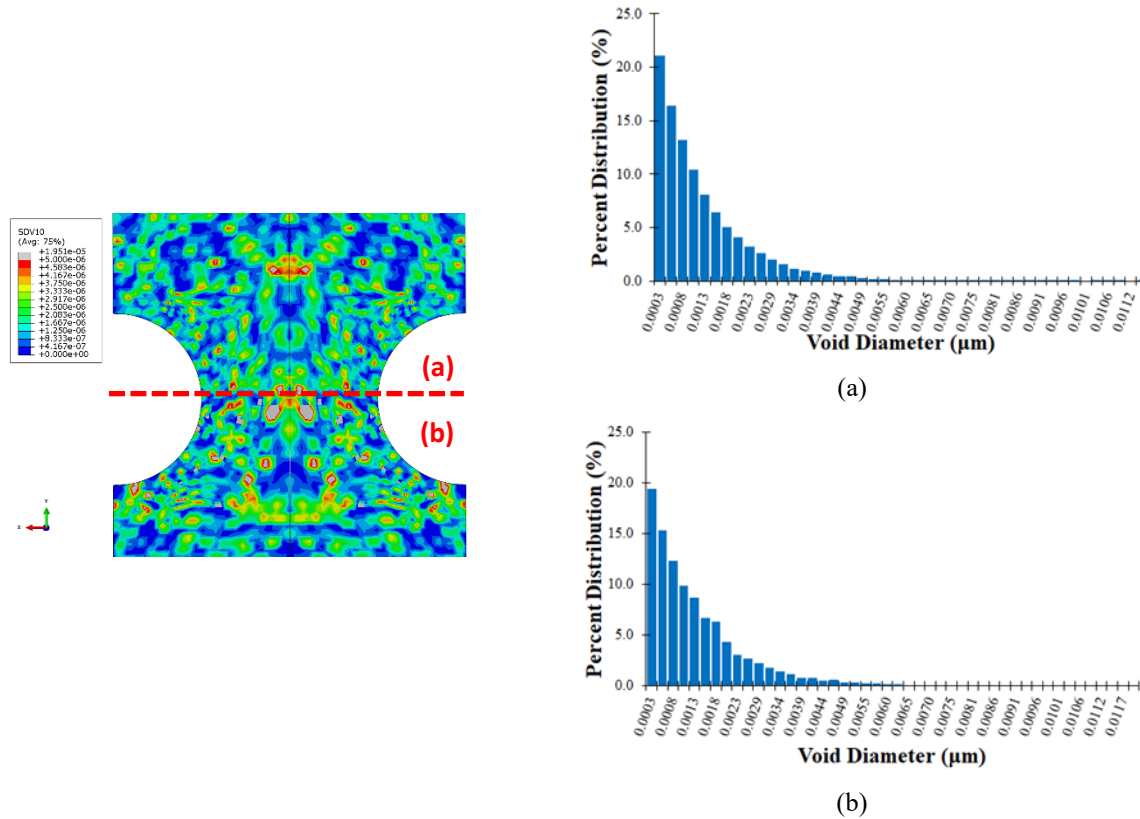


Figure 3.13 Heterogeneous distribution of initial void radii in an Al 7085-T711 notch tension specimen.

- (a) Void diameter distribution in region (a) of Bridgman specimens.
- (b) Void diameter distribution in region (b) of Bridgman specimens.

The contour for void area fraction was assessed to determine the model's ability to predict damage progression in a heterogeneous microstructure. A comparison of the void area fraction contour to an experimental fracture surface is given in Fig. 3.14. Figure 3.14 shows that the ISV model tends to predict a predominately localized damage evolution that approximates the cup-cone phenomena due to the nonuniform distribution of microstructural features. This effect is not evident in previous FEA simulations the material with assumed homogeneous distribution of microstructure properties (Fig. 3.10-

11). The combination of a fully stress state dependent damage model and heterogeneous microstructure property distribution permits the successful prediction of localized, asymmetric damage progression and, hence, the cup-and-cone fracture.

This work demonstrates the usefulness of the combined ISV constitutive model and heterogeneous microstructure property distribution for predicting failure modes that traditional models using homogeneous assumptions fail to capture. Experimental observation of microstructures could be used to statistically develop spatial property distributions that precisely represent actual material conditions. Horstemeyer (2012), Allison *et al.* (2013), and Doude *et al.* (2018) used similar methods in predicting microstructure influenced fracture initiation in areas of noncritical stress or tensile pressure concentration in engineering structures.

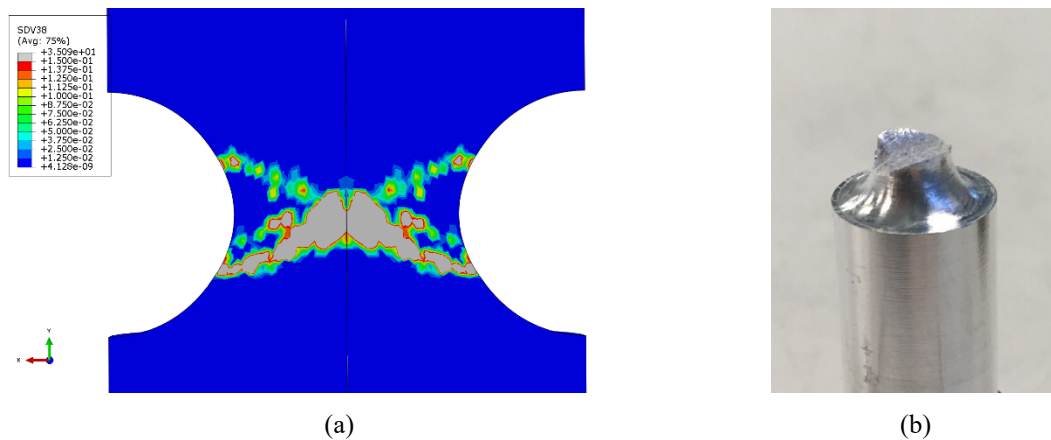


Figure 3.14 Comparison of model prediction and observed fracture surface morphology of 2.54 mm notch root radius Bridgman specimen fracture surface.

- (a) ISV model prediction of void area fraction progression.
- (b) Experimentally observed “cup” section of a cup-cone fracture.

3.4 Conclusions

An Internal State Variable (ISV) constitutive model for describing the non-uniform deformation and failure of an aluminum 7085-T711 alloy has been developed within a kinematic and thermodynamically consistent framework. While the model is used specifically for an aluminum 7085 alloy in this study, the general framework is applicable for a wide range of ductile metals. The ISV model's ability to predict plasticity and damage evolution has been validated using a variety of experimental results for DBSC and Bridgeman notched tensile specimens for aluminum 7085, along with high resolution microscopy. A concise list of conclusions from the work are as follows:

1. Shear influenced growth rates of pre-existing and nucleated voids are accurately captured for an aluminum 7085 alloy using a Lode angle function in equations describing void growth.
2. The relation governing void coalescence is posed as a function of an evolving Intervoid Ligament Distance (ILD). The ISV model can predict the microstructural conditions necessary for void coalescence to appreciably affect the void volume fraction evolution.
3. The robust stress state sensitive ISV relations for void nucleation, growth, and coalescence enable modeling of localization and failure mechanisms in materials subjected to complex structural deformation.
4. Modeling heterogeneous distributions of microstructure properties in conjunction with a robust stress state sensitivity damage model enables the prediction of

asymmetric fracture modes. In this case, the cup-cone fracture of a 0.254 mm aluminum 7085 notch radius Bridgman tension specimen was predicted.

The ISV constitutive model and heterogeneous microstructure property distribution framework facilitates finite element (FE) prediction of asymmetric failure modes commonly observed in engineering practice. Traditional constitutive models operating under homogeneous property assumptions often fail to predict such phenomena. The microstructure property informed ISV model is a powerful tool for predicting deformation of ductile alloys at varying strain rates, stress states, and temperatures. Currently, the ISV model is limited to scalar definitions of void growth and coalescence related to damage. Future studies should investigate second rank tensor relations for void growth and coalescence ISVs to capture shape, orientation, and distribution effects.

CHAPTER IV

USING AN INTERNAL STATE VARIABLE MODEL FRAMEWORK TO INVESTIGATE MICROSTRUCTURE AND MECHANICAL PROPERTY INFLUENCE ON BALLISTIC PERFORMANCE OF STEEL ALLOYS

4.1 Introduction

4.1.1 Ballistic Impact Modeling and Experiments

Ballistic impact of ductile metals is a topic of interest for defense and space applications. A summary of seminal experimental impact results and discussions of basic penetration mechanisms can be found in Backman and Goldsmith (1978) and Corbett *et al.* (1996). Backman and Goldsmith (1978) reviewed much of the foundational early literature pertaining to ballistic impacts and penetration. Backman and Goldsmith (1978) described a number of relevant plate impact damage mechanisms: (1) fracture due to stress waves (Tsai and Kolsky, 1967; Bowden and Field, 1964; Camacho and Ortiz, 1996), (2) radial fracture behind a stress wave (Evans *et al.* 1978, Johnson, 1981; Camacho and Ortiz, 1996), (3) spallation (Curran *et al.* 1977; Johnson, 1981; Meyers, 1983; Curran *et al.* 1987; Grady, 1988), (4) shear plugging (Ipson, 1963; Averbuch and Bodner, 1974; Curran *et al.* 1977, Goldsmith and Finnegan, 1986; Børvik *et al.* 1999), (5) petaling (Goldsmith *et al.* 1965;

Awerbuch and Bodner, 1974; Levy and Goldsmith, 1984; Hou and Goldsmith, 1996), (6) fragmentation (Johnson, 1981; Grady, 1982; Grady and Kipp, 1985; Glenn and Chudnovsky, 1986), and (7) ductile hole enlargement (Thomson, 1955). The current work primarily focuses on penetration mechanisms of plasticity induced rupture (related to ductile hole enlargement) and shear plugging.

A wealth of experimental and numerical model data pertaining to material ballistic impact performance exists in the literature. The behavior of a variety of metal plates subjected to normal and oblique impacts by projectiles of varying shape, size, material, and is discussed at length (Manganello, 1967; Goldsmith *et al.* 1971; Goldsmith and Finnegan, 1986; Littlefield *et al.* 1997). Additionally, Anderson *et al.* (1992) contains experimental data for hundreds of projectile/target configurations and test conditions. Examples of numerical ballistic penetration models can be found in Johnson and Cook (1985), Johnson and Holmquist (1988), Bammann *et al.* (1993), Anderson *et al.* (1999), Børvik *et al.* (2001), Børvik *et al.* (2003), Dey *et al.* (2004), and others. In general, the ballistic perforation resistance strongly correlates the target materials' strength and hardness values. However, Mescal and Rogers (1989), Dikshit *et al.* (1995), and Dey *et al.* (2004) observed that some steel plates exhibited a decrease in ballistic performance at high hardness typically exceeding 400 Brinell Hardness Number (BHN). Mescal and Rogers (1989) attributed this diminishing performance to a change in penetration mechanisms from rupture due to large plastic flow at low hardness values to perforation by localized shear plugging at high hardness.

In this study, the microstructural changes leading to an apparent decrease in ballistic performance associated with high material hardness values (Mescall and Rogers, 1989) is described by an Internal State Variable (ISV) based constitutive model. Part I of this document pertains to validation of the combined ISV model and finite element analysis framework for predicting behavior of materials subjected to ballistic loads. Part II summarizes a simulation-based parametric sensitivity study assessing the influence of select microstructural features and mechanical properties on ballistic performance. Part III presents the effects of variations in microstructural features and material properties within a finite element simulation framework on decreased ballistic performance of high hardness steels observed by Mescall and Rogers (1989).

4.1.2 Material Selection for Ballistic Impact Study

Chapters II and III involved predicting the mechanical behavior and microstructure evolution for deformation of an aluminum 7085-T711 alloy using an ISV framework extended to account for the effects of shear influenced void growth. The extended ISV model for aluminum 7085-T711 was validated by accurately predicting the mechanical response and void property (average void number density, size, and area fraction) evolution for Bridgman notch tension specimens of varying notch radii deformed at 25 and 200°C.

The objective of the current study is to apply the extended ISV model framework for predicting performance of ductile materials subjected to ballistic impact loads. Emphasis is placed upon studying the transition in perforation mechanisms and reduction

of ballistic performance for increasing Brinell hardness steel alloys observed by Mescall and Rogers (1989). To the best of the author's knowledge, these tendencies have not been documented for aluminum alloys in the literature. However, an ISV-based constitutive model was used to simulate plasticity and damage evolution due to high velocity impact of steel structures (Bammann *et al.* 1993). Therefore, a calibrated ISV model for a Rolled Homogeneous Armor (RHA) steel alloy (Whittington *et al.* 2014) is adapted to the extended ISV model framework for use in ballistic impact finite element simulations.

4.1.3 Internal State Variable Constitutive Model

A physically motivated viscoplasticity model was developed by Bammann (1984) within the ISV thermodynamic framework established by Coleman and Gurtin (1967). Bammann's ISV plasticity model was revised to account for damage in the form of void volume fraction (Bammann and Aifantis, 1989) and later refined to consider damage evolution stemming from the nucleation (Horstemeyer and Gokhale, 1999; Horstemeyer *et al.* 2003A), growth, and coalescence of voids (Horstemeyer *et al.* 2000A). The ISV model presented in Horstemeyer and Gokhale (1999) incorporates McClintock's (1968) void growth rule for voids growing from secondary phase particles and Cocks and Ashby's (1982) unified growth mechanism model for pre-existing voids. The ISV plasticity-damage model has been used to characterize the structure-property relationships for aluminum (Horstemeyer *et al.* 2000A; Jordon, 2007; Tucker *et al.* 2010), steel (Horstemeyer *et al.* 2000B; Horstemeyer and Ramaswamy, 2000; Guo *et al.* 2005; Anurag *et al.* 2009; Whittington *et al.* 2014), copper (Crapps *et al.* 2010), titanium (Guo *et al.*

2005), and magnesium (Lugo *et al.* 2011; Walton *et al.* 2014; Lugo *et al.* 2018) alloys. The constitutive model has been used within a Finite Element Analysis (FEA) framework to successfully simulate a variety of thermomechanical deformations including forming processes (Bammann *et al.* 1996; Horstemeyer and Ramaswamy, 2000; Crapps *et al.* 2010; Cho *et al.* 2015; Cho *et al.* 2018), high velocity impacts (Whittington *et al.* 2014), and structural crashworthiness (Bammann *et al.* 1993; Fang *et al.* 2005; Horstemeyer *et al.* 2009). Previous studies have shown that while the stress state, strain rate, and temperature sensitivities for plasticity and damage evolution vary by material and processing history, void nucleation and growth evolve exponentially with increasing strain for steels (Horstemeyer and Ramaswamy, 2000; Allison, 2009; Whittington *et al.* 2014) and aluminums (Horstemeyer and Ramaswamy, 2000; Jordon *et al.* 2007, Tucker *et al.* 2010). Furthermore, ISV model predicted damage evolution rates increase in steels (Allison, 2009; Whittington, 2014) and aluminums (Tucker *et al.* 2010) with increasing stress triaxiality in agreement with the established consensus (McClintock, 1968; Rice and Tracey, 1969; Gurson, 1977). The ISV model extended for shear influenced void growth captures the stress state sensitivity and exponential evolution of damage with plastic strain for an aluminum 7085-T711 alloy (Peterson *et al.* 2019) in agreement with the aforementioned studies. Therefore, the extended ISV model framework retains the general applicability to ductile metal alloys and is suitable for use in ballistic impact simulations for steel alloys.

4.2 Methods

4.2.1 Part I: Ballistic Impact of Rolled Homogeneous Armor Steel Plates by Spherical Projectiles

Experimental testing of Rolled Homogeneous Armor (RHA) steel spherical projectile impact of RHA steel plates was performed at the Engineer Research and Development Center (ERDC) in Vicksburg, MS. 457.2 mm wide square RHA steel plates of 9.53 mm and 12.7 mm thickness were experimentally impacted by 12.7 mm diameter RHA steel spheres fired from a .50 caliber rifled barrel at varying velocities to obtain the ballistic limit (perforation) velocity (V50) and residual velocity profiles for each target configuration. The experimental conditions were simulated using an Abaqus-Explicit FEA solver in conjunction with a previously calibrated (Whittington *et al.* 2014) ISV constitutive model for RHA steel (contained in Table A.1) to validate the ISV model framework for predicting ballistic performance.

4.2.2 Finite Element Simulation Framework

High velocity quarter symmetry impact simulations of RHA steel targets by RHA steel spheres and cylinders (configuration given in Fig. 4.1a-b) were performed using Abaqus-Explicit FEA software in conjunction with ISV constitutive model user material subroutines (VUMAT). Table 4.1 lists the target/projectile geometric properties and total number of finite elements for each case. Cases 1 and 2 each define spherical impact experiments used to validate the modeling framework. Case 3 simulates the cylindrical

projectile impact experiments performed by Mescall and Rogers (1989). Identical RHA steel mechanical properties were used for both target and projectile materials in every simulation. In the simulations, the in-plane target plate dimensions were reduced from their actual values to reduce computational expense. A minimum 10:1 plate width-to-thickness ratio and 10:1 plate width-to-projectile-diameter ratio were used to ensure plate edge effects were negligible. An initial velocity was applied to the projectile ranging from 700 – 1400 m/s, where quarter symmetry conditions were imposed on both projectile and target plate to reduce computational expense. The Abaqus Explicit FEA solver is limited to elements with first order (linear) formulation. Therefore, linear hexahedral temperature-displacement reduced integration (selected to prevent element shear locking) elements (C3D8RT) were used to mesh the projectile and target structures. Element erosion of the contact surface between target and projectile tip was used to facilitate solution convergence.

Table 4.1 Geometric properties of quarter symmetry projectiles and targets used in Abaqus-Explicit finite element analysis simulations.

Test Condition	Object	Shape	Thickness (mm)	Length (mm)	Diameter (mm)	No. Elements
1	Projectile	Sphere	-	-	12.70	11424
	Target	Square	9.53	127.0	-	206400
2	Projectile	Sphere	-	-	12.70	10136
	Target	Square	12.70	170.0	-	238680
3	Projectile	Cylinder	-	12.70	6.35	3840
	Target	Square	6.35	63.50	-	97344

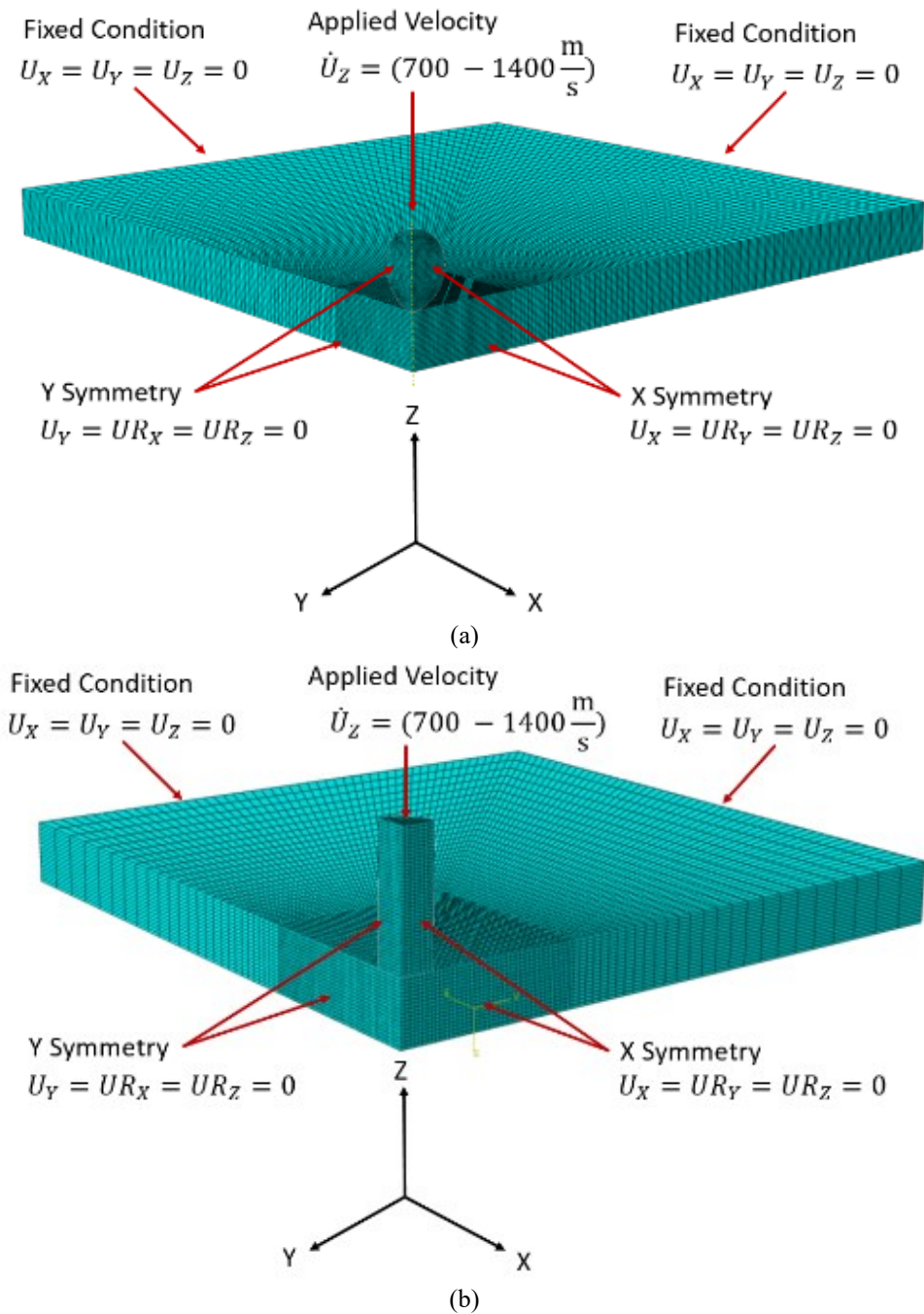


Figure 4.1 Abaqus Explicit Finite Element Analysis mesh and axisymmetric boundary conditions for ballistic impact of a semi-infinite square targets by cylindrical and spherical projectiles.

A mesh study was performed using test condition 3 from Table 4.1 to ensure the impact simulations consistently converge upon an accurate solution. The impact of an RHA steel cylinder against an RHA steel plate (dimensions given by condition 3 of Table 4.1) at 950 m/s was simulated for the mesh convergence study. Figure 4.2 shows the residual projectile velocity converges to zero (projectile arrested) after a target mesh density of approximately 70,000 C3D8RT elements. The mesh density was achieved by using a minimum of 20 elements through the thickness of the contact region of the target plate. The principle of maintaining 20 or more elements through the target thickness was subsequently applied for all simulations from test conditions 1-3 in Table 4.1 to ensure convergent results. Elements in the projectiles for test conditions 1-3 were smaller or equal in size to the smallest elements in the contact region of the target mesh.

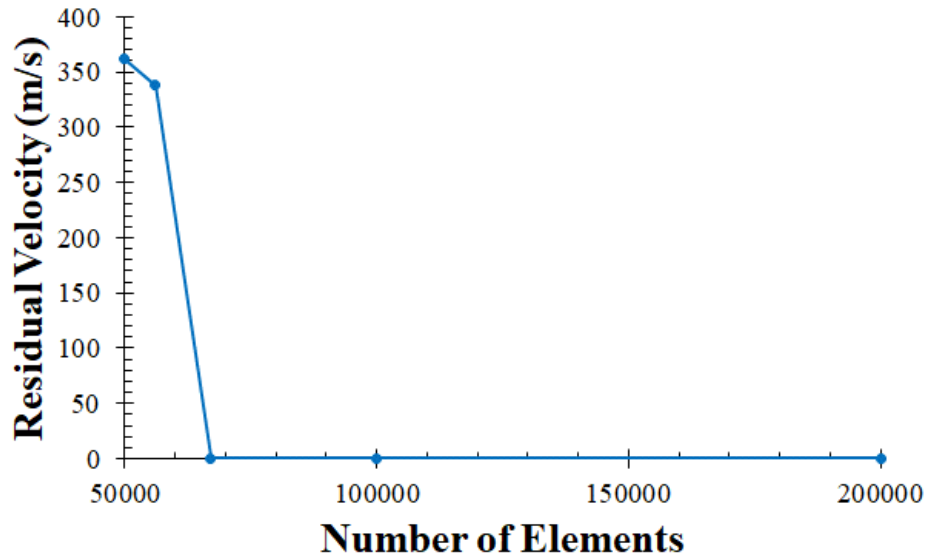


Figure 4.2 Mesh convergence study for RHA steel cylinder impacting RHA steel plate at 950 m/s.

4.2.3 Internal State Variable Constitutive Model

A theory for ISV plasticity and damage modeling has been developed by Bammann (1984; 1989; 1996) and Horstemeyer (1999; 2000A; 2001; 2003A) that accounts for internal dissipative mechanisms and load history effects to predict a material's future constitutive behavior. The material history is strongly influenced by the plasticity-based hardening and porosity-based softening mechanisms, although the selection and implementation of appropriate ISVs may be somewhat subjective. Horstemeyer *et al.* (2003B) noted that the ISV plasticity-damage model incorporates deviatoric inelastic deformation resulting from the presence of dislocations in crystalline materials, dilatational deformation, and ensuing failure from damage progression. Here damage reduced material strength, increased inelastic flow rate, and increase compliance in ductile metals.

A summary of the ISV plasticity-damage model relations is provided in the following section. A standard tensorial notation is employed. Assume a nominal parameter, (A) , bold symbols denote second rank tensors (\mathbf{A}), rate functions are denoted by a dot accent (\dot{A}) and frame indifferent second rank tensors are denoted by an overbar and dot accent ($\overline{\dot{\mathbf{A}}}$).

The kinetic stress-strain relationship between stress and strain is observed to be strain rate, stress state, and temperature dependent in nature for many ductile materials. The presence of dislocations, secondary phase particles, voids, and other microstructural features influence the mechanical material behavior. The following kinetic and kinematic constitutive relations (Horstemeyer *et al.* 2000A) describe the frame indifferent stress rate, elastic rate of deformation, and inelastic flow, respectively:

$$\overline{\dot{\boldsymbol{\sigma}}} = \dot{\boldsymbol{\sigma}} - \mathbf{W}_e \boldsymbol{\sigma} + \boldsymbol{\sigma} \mathbf{W}_e = \lambda(1 - \phi) + 2\mu(1 - \phi) \mathbf{D}_e - \frac{\dot{\phi}}{1 - \phi} \boldsymbol{\sigma}, \quad (4.1)$$

$$\mathbf{D}_e = \mathbf{D} - \mathbf{D}_{in}, \quad (4.2)$$

$$\mathbf{D}_{in} = \sqrt{\frac{3}{2}} f(T) \left[\frac{\left[\sqrt{\frac{3}{2}} \left\| \boldsymbol{\sigma}' - \sqrt{\frac{2}{3}} \boldsymbol{\alpha} \right\| - (R + Y(T))(1 - \phi) \right]}{V(T)(1 - \phi)} \right] \cdot \frac{\boldsymbol{\sigma}' - \sqrt{\frac{2}{3}} \boldsymbol{\alpha}}{\left\| \boldsymbol{\sigma}' - \sqrt{\frac{2}{3}} \boldsymbol{\alpha} \right\|}. \quad (4.3)$$

Here, an objective (frame indifferent) Jaumann stress rate, $\overline{\dot{\boldsymbol{\sigma}}}$, is assumed such that the total spin tensor is equivalent to the elastic spin tensor, \mathbf{W}_e (*i.e.*, the inelastic spin is negligible). $\boldsymbol{\sigma}$ describes the Cauchy stress tensor in the current configuration, and λ and μ are Lamé elastic constants. \mathbf{D} , \mathbf{D}_e , and \mathbf{D}_{in} are the total, elastic, and inelastic rate of deformation tensors, respectively. The void volume fraction, ϕ , is used to define the extent of damage.

In Eq. (4.3), creep and plasticity are accounted for through specification of the inelastic rate of deformation, \mathbf{D}_{in} , as a function of temperature (T), deviatoric stress tensor ($\boldsymbol{\sigma}'$), kinematic hardening ISV ($\boldsymbol{\alpha}$), isotropic hardening ISV (R), void volume fraction (ϕ), and yield related functions $Y(T)$, $f(T)$, and $V(T)$. The functions $Y(T)$, $f(T)$, and $V(T)$ have an Arrhenius-type temperature dependence as described in Bammann *et al.* (1993). In general, $Y(T)$, $f(T)$, and $V(T)$ are used to characterize the rate independent yield stress, threshold for strain rate dependent yielding, and influence of loading rate on yielding, respectively. Monotonic compression, tension, and torsion tests at different temperatures and strain rates are used to determine the functions $f(T)$, $V(T)$, and $Y(T)$. Equations (4.1) and (4.3) reflect the tendency for damage, ϕ , to increase compliance and increase inelastic flow rate (leading to strain localization), respectively.

ISVs that account for dislocation density effects control the plasticity evolution of the constitutive model. Kinematic and isotropic hardening ISVs ($\boldsymbol{\alpha}$ and R) are used to represent the effects of geometrically necessary and statistically stored dislocation densities, respectively. The frame indifferent kinematic hardening rate, $\dot{\boldsymbol{\alpha}}$, and isotropic hardening rate, \dot{R} , are described in Jordon be described as

$$\dot{\boldsymbol{\alpha}} = \dot{\boldsymbol{\alpha}} - \mathbf{W}_e \boldsymbol{\alpha} + \boldsymbol{\alpha} \mathbf{W}_e = \left(h(T) \mathbf{D}_{in} - \left[\sqrt{\frac{2}{3}} r_d(T) + r_s(T) \right] \|\boldsymbol{\alpha}\| \boldsymbol{\alpha} \right) \left(\frac{GS_0}{GS} \right)^Z, (4.4)$$

where $h(T)$ represents the kinematic hardening modulus, and $r_s(T)$ and $r_d(T)$ are scalar functions describing the static and dynamic recovery for kinematic hardening, respectively. Similarly, the frame indifferent isotropic hardening rate, \dot{R} , may be expressed as

$$\dot{R} = \left(H(T) \sqrt{2/3} \mathbf{D}_{in} - \left[\sqrt{2/3} R_d(T) \|\mathbf{D}_{in}\| + R_s(T) \right] R^2 \right) \left(\frac{GS_0}{GS} \right)^Z. \quad (4.5)$$

where $H(T)$ characterizes the isotropic hardening modulus, and $R_s(T)$ and $R_d(T)$ account for the static and dynamic recoveries for isotropic hardening. Equations (4.4) and (4.5) each account for grain growth dependence (where GS_0 and GS represent the initial and final grain sizes, respectively) and strain-rate dependence.

Within ductile materials, damage primarily consists of microstructural porosity. Significant levels of damage cause an increase in compliance and contribute to strain localization. Damage evolution in ductile materials arises due to the nucleation, growth, and coalescence of voids (*cf.* Horstemeyer *et al.* 2000A) from microstructural heterogeneities during deformation. Additionally, pre-existing voids (pores) due to processing defects may grow and coalesce during deformation. The total porosity evolution equation (*cf.* Jordon *et al.* 2007) is may be expressed as:

$$\dot{\phi} = [\dot{\phi}_{particles} + \dot{\phi}_{pores}]C + [\phi_{particles} + \phi_{pores}]\dot{C}, \quad (4.6)$$

where C is a coalescence parameter, \dot{C} is the rate of void coalescence, $\phi_{particles}$ is the *current* volume fraction of voids nucleated from particles during deformation, and ϕ_{pores} is the *current* volume fraction of pre-existing voids. The rate of change in volume fraction of nucleated and pre-existing voids may be written as (*cf.* Jordon *et al.* 2007):

$$\dot{\phi}_{particles} = \dot{\eta}v + \eta\dot{v}, \quad (4.7)$$

and

$$\dot{\phi}_{pores} = \left[\frac{1}{(1-\phi_{pore})^m} - (1 - \phi_{pore}) \right] \sinh \left[\frac{(2V(T)/Y(T))-1}{(2V(T)/Y(T))+1} \cdot \frac{I_1}{3\sqrt{J_2}} \right] \| \mathbf{D}_{in} \|. \quad (4.8)$$

In Eq. (4.7), $\dot{\phi}_{particles}$ is a function of the average void number density (η), average void volume (v), void nucleation rate ($\dot{\eta}$), and void growth rate (\dot{v}). The expression for $\dot{\phi}_{pores}$ in Eq. (4.8) was formulated using the Cocks-Ashby (1982) damage evolution framework to account for stress triaxiality and strain-rate effects for pre-existing pores: m is the Cocks-Ashby calibration coefficient; the ratio $V(T)/Y(T)$ accounts for strain rate sensitivity; and the first stress invariant (I_1) and second deviatoric stress invariant (J_2) account for the effect of stress triaxiality on pore growth rates.

Horstemeyer (1999; 2000A, 2003A) employed ISVs to represent the effects of void nucleation from second phase particles, their associated growth and coalescence on the total void volume fraction (damage) within ductile materials. Void nucleation, growth, and coalescence rates exhibit material dependent strain rate, stress state, and thermal sensitivities. Horstemeyer and Gokhale (1999) posed the void nucleation rate as,

$$\dot{\eta} = \frac{d^{1/2}}{K_{IC} f^{1/3}} \eta \cdot \left(a \left[\frac{4}{27} - \frac{J_3^2}{J_2^3} \right] + b \frac{J_3}{J_2^3} + c e^{mH_B} \left\| \frac{I_1}{\sqrt{J_2}} \right\| \right) \| \mathbf{D}_{in} \| \exp \left(\frac{C_{\eta T}}{T} \right). \quad (4.9)$$

Here, K_{IC} is the fracture toughness, d is the secondary phase particle size, f is secondary phase particle volume fraction, and J_3 is the third deviatoric stress invariant. The stress state sensitivity is modeled using the invariants I_1 , J_2 and J_3 . The calibration parameters a , b , and c control the shear sensitivity, distinguish between tension and compression, and capture the stress triaxiality sensitivity, respectively. Consistent with Dighe *et al.* (1998), the void nucleation rate ($\dot{\eta}$) is dependent on temperature (T) and the calibration constant

($C_{\eta T}$) is used to control the magnitude of temperature dependence. Chandler *et al.* (2013) introduced the parameters H_B and m_h to represent the interfacial hydrogen concentration in atomic parts per million (APPM) and a given material's fracture sensitivity due to the presence of hydrogen, respectively. Chandler *et al.* 2013 related the lattice hydrogen concentration in stressed regions (H_σ) to the trapped hydrogen concentration at interfaces of grain, subgrain, and inclusion boundaries (H_B) using a theoretical approach developed by McClean (1957) and Oriani and Josephic (1979), *i.e.*,

$$\frac{H_B}{1-H_B} = \frac{H_\sigma}{1-H_\sigma} \exp\left(\frac{-W_B}{RT}\right). \quad (4.10)$$

where W_B is the binding energy of hydrogen at trapping sites, and R is the universal gas constant and H_σ is the hydrogen concentration in stressed regions. The hydrogen concentration in a stressed region (H_σ) is a function of the lattice hydrogen in unstressed regions (H_L) and the hydrostatic pressure (*i.e.*, $\sim I_1$):

$$H_\sigma = H_L \exp\left(\frac{I_1 V}{3RT}\right), \quad (4.11)$$

where V is the hydrogen molar volume.

McClintock (1968) developed a void growth framework that captures the effects of thermal and stress state dependence on void growth mechanisms. Using this framework, a void growth evolution equation may be expressed as (Peterson *et al.* 2019)

$$\dot{v} = \frac{\pi}{6} \left(\left(A_{void} D_0 \left[1 - \left(\frac{27J_3}{2(3J_2)^{3/2}} \right)^2 \right] \frac{D_{ij}^d \cdot \sigma'_{ij}}{\sqrt{3}J_2} + B_{void} D_0 \frac{J_3}{J_2^2} \| \underline{D}^{in} \| + \frac{\sqrt{3}D_0}{2(1-n)} \left[\sinh \left(\sqrt{3}(1-n) \frac{\sqrt{2}I_1}{3\sqrt{J_2}} \right) \right] \| \underline{D}^{in} \| \right) \exp(C_{Tv} \cdot T) \right)^3 \quad (4.12)$$

where D_0 is the average initial diameter of voids in the material. Like the relation for void nucleation rate (Eq. 4.9), the void growth rate relation (\dot{v}) employs stress invariant ratios to account for stress state effects. Parameters A_{void} , B_{void} , and n control the shear sensitivity, distinguish between tension and compression, and the stress triaxiality sensitivity of the void growth rate, respectively. Additionally, the calibration constant C_{Tv} controls the void growth ISV's temperature dependence. Analogously, an expression for void coalescence rate (\dot{C}) was developed that accounts for the effects of void nucleation and coalescence (Horstemeyer *et al.* 2000A), grain size (Jordon *et al.* 2007) and void nearest neighbor distance effects (Allison, 2009),

$$\dot{C} = \left[\left(4d_0 / NND \right)^\zeta + cd_2 [\dot{\eta}v + v\dot{\eta}] \right] \exp(C_{CT}T) \left(GS_0 / GS \right)^z, \quad (4.13)$$

where d_0 is the average initial diameter, v is the average void volume, η is the average void number density, NND is the average nearest neighbor distance between voids, ζ is a dimensionless length scale calibration parameter, GS_0 represents the initial grain size, and GS accounts for grain growth due to recrystallization.

4.2.4 Part II: Parameter Sensitivity Study

4.2.4.1 Second Phase Particle Number Density and Size

Microstructures of crystalline materials are typically heterogeneous, consisting of a number of, high volume fraction phases, small secondary phase particles, impurities, and voids. Secondary phase particles are known to serve as nucleation sites for damage in

heterogeneous crystalline materials (Puttick, 1959; Gangulee and Gurland, 1967; Lindley *et al.* 1970; Brown and Embury, 1973; Hancock and Mackenzie, 1976). The Horstemeyer *et al.* (1999) void nucleation ISV model (Eq. 4.9) was predicated on the empirical relationship for void nucleation rate as a function between second phase particle size and volume fraction developed by Gangulee and Gurland (1967). For this study particle number density, η , and diameter, d , are treated as independent design variables and particle area fraction is calculated as the product of average void number density and area for the sake of consistency:

$$f = \eta \cdot \pi \left(\frac{d}{2}\right)^2. \quad (4.14)$$

The distribution of second phase number densities has been experimentally quantified for several high strength steels and included in Table 4.2. The orders of magnitude of particle number densities appears to consistently vary between 10^2 and 10^3 particles/mm². The nominal upper and lower bounds for η were selected as 250 and 4000 particles/mm², respectively, for the parameter sensitivity study.

The effects of particle size on damage evolution have been noted in the literature (Gangulee and Gurland, 1967; Gurland 1972). Gangulee and Gurland showed that the fraction of fractured particles in a stressed material followed a $d^{1/2}/f^{1/3}$ relationship, thus increasing particle size for a given volume fraction increases void nucleation rates. In steels, secondary phase particle diameters have been observed to range from the order of 10^{-4} to 10^{-2} mm (Table 4.2). The values for particle size, d , correspondingly range from 10^{-4} to 10^{-2} mm in the parameter sensitivity study.

Table 4.2 Second phase particle property distributions in high strength steels from literature sources.

Study	Material	Number Density (#/mm ²)	Diameter (μ m)	Volume Fraction
Cox and Low (1974)	4340 Steel	800 – 4000	4.5 – 9.7	0.06
Fisher and Gurland (1974)	0.17-0.44 C Steel	430	14.0	0.066
Maloney and Garrison (1989)	HY 180 Steel	2600 – 6000	0.20 – 0.32	0.00019 – 0.00021
Whittington (2014)	RHA Steel	170	7.0	0.00065

4.2.4.2 Grain Size

Grain size and morphology effects on inelastic behavior of crystalline materials has been a cornerstone of metals research for the last century. Hall (1951) and Petch (1953) observed an inverse square root relationship between grain size and yield stress applicable to a variety of metals. Research has also shown an inverse correlation between grain size and hardening rate (Meakin and Petch, 1963; Conrad *et al.* 1967; Conrad, 1970; Thompson, 1977; Narutani and Takamura, 1991), although notable exceptions are discussed in Thompson *et al.* (1973). However, Grain boundaries serve as preferential nucleation sites for heterogeneities (dislocations, second phase particles, carbides, and voids) and the positive correlation between microstructure heterogeneity properties and damage evolutionary rates is well documented (Puttick, 1959; Gangulee and Gurland, 1967; Lindley *et al.* 1970; Brown and Embury, 1973; Hancock and Mackenzie, 1976). Smaller grain boundaries lead to not only more potential heterogeneity precipitation sites but also shorter distances between defects that can facilitate local stress field interaction and subsequent void coalescence (Cottrell, 1959; Brown and Embury, 1973; Bourcier and Koss, 1979).

It is understood that grain size and morphology will influence damage evolution modes and rates. Void coalescence in Eq. (4.13) based on the models of Horstemeyer and Gokhale (1999), Allison (2009), and Horstemeyer and Tucker (2010) is posed as a function of grain size, where GS_0 is a reference grain size, GS is the current grain size due to recrystallization, and Z is the grain size sensitivity exponent. The grain size sensitivity exponent, Z , has been calibrated for a variety of materials, including steel (Cho *et al.* 2018). Grain sizes in steel have been shown to vary from 1 μm in diameter for high strength steels (and even less than 1 μm in specially designed ultra-fine-grained materials) to greater than 100 μm size for mild steels (Petch, 1953; Li *et al.* 2016). The bounds for the grain size term, GS , were selected as 1 μm and 100 μm , accordingly.

4.2.4.3 Initial Void Volume Fraction

Porosity in the microstructure of crystalline materials can deleteriously affect the material's mechanical performance. Yamamoto (1978) demonstrates that increasing levels of initial material significantly reduces the localization to yield strain ratio. Similarly, Tvergaard (1982) uses micromechanics-based calculations to show that initial microporosity contributes to large localized strains and void growth. The initial void volume fraction depends largely on the material's processing history. Initial void volume fraction magnitudes can approach 10^{-2} to 10^{-1} for cast steels (Department of the Army, 1959; Dong *et al.* 1997; Hardin and Backerman, 2007). Conversely, wrought steels may exhibit very low initial porosities (10^{-4} noted in Whittington *et al.* 2014). Horstemeyer and Ramaswamy (2000) notes that experimental quantification of void volume fractions lower

than 10^{-4} is difficult, but numerically demonstrated significant effects of microporosity of 10^{-6} on void growth rates in aluminum and 304L stainless steel alloys. For engineering materials, minimal strain is required for failure beyond aggregate void volume fractions of 10^{-1} . Therefore, the upper and lower bounds for initial porosity in the parameter sensitivity study were selected as 10^{-2} and 10^{-6} , respectively.

4.2.4.4 Lattice Hydrogen Concentration

Hydrogen content in materials increases damage evolution rates and amplifies damage effects in a mechanism referred to as ‘hydrogen embrittlement’ (Barnett, 1957; Westlake, 1969; Beachem, 1972; Ferreira *et al.*, 1999). Sakamoto and Mantani (1976) shows that high strength steels are particularly susceptible to hydrogen embrittlement because lattice imperfections (dislocations, vacancies, subgrain boundaries, and microvoids) from the martensitic transformation process serve as trapping sites for diffusing hydrogen atoms. Chandler *et al.* 2008 used molecular dynamics (MD) simulations in conjunction with an embedded atom method (EAM) potential to study the effects of hydrogen concentrations at grain boundaries in a nickel alloy. The local interfacial boundary hydrogen concentration rate from lattice concentration levels was shown to strongly correlate to the stress triaxiality in the crystals. A relationship between the void nucleation rate and localized hydrogen concentration was derived for polycrystalline materials (Chandler *et al.* 2013). They studied the effects of lattice hydrogen concentrations between 10^{-5} and 10^{-4} atomic parts per million (APPM) in 1518 spheroidized steel and showed significant increase in nucleation rate relative to

unhydrogenated materials. However, Lee and Gangloff (2007) observed lattice hydrogen concentrations as high as 10^{-2} APPM in hydrogen embrittled steels. The upper and lower bounds for lattice hydrogen concentration, H_L , were selected as 10^{-3} and 10^{-5} APPM, respectively. Values for the binding energy, $W_B = 56 \text{ kJ}\cdot\text{mol}^{-1}$, gas constant, $R = 8.31 \text{ J}\cdot\text{mol}^{-1}\cdot\text{K}^{-1}$, and molar hydrogen volume, $V = 2.0 \text{ cm}^3\cdot\text{mol}^{-1}$, and hydrogen sensitivity, $m_h = 3.0$, coefficients used in Eq. (4.10)-(4.11) were obtained from Chandler *et al.* 2013.

4.2.4.5 Material Hardness

A variety of studies have assessed the effect of hardness and mechanical properties on ballistic performance of target materials (Manganello and Carter, 1967; Speich *et al.*, 1974; Hu *et al.*, 1976; Mescall and Rogers, 1989; Dikshit *et al.*, 1995). Theoretically, increasingly hard materials with similar failure strains should perform more favorably under ballistic impact due to higher energy absorption capacity. However, Mescall and Rogers (1989), Dikshit *et al.* (1995) and (for blunt projectiles) Dey *et al.* (2004) show the ballistic merit of target materials initially increases with hardness until high Brinell hardness (BHN) levels (greater than 400 BHN) where performance significantly diminishes. Mescall and Rogers (1989) asserted that variations in microstructure heterogeneity properties for high hardness materials leads to adiabatic shear band nucleation, fracture, and subsequent reduced perforation velocities. The sensitivity of residual projectile velocity to mechanical properties affecting hardness has been assessed in this study. The steel hardness values were varied between 250 – 550 BHN to observe the hardness range experimentally studied by Mescall and Rogers (1989). Yield and

ultimate tensile strength (UTS) of a previously characterized RHA steel alloy (Whittington *et al.* 2014) were varied in accordance with known strength-hardness correlations for 4340 steel (Bhat, 1977; Horn and Ritchie, 1978) to achieve the desired hardness values. The ISV model constants C03, C09, and C15 were varied to achieve the desired mechanical properties and are shown in Table 4.3.

Table 4.3 Mechanical properties and model coefficients for steel alloys of varying Brinell Hardness (BHN).

		Brinell Hardness (BHN)				
	Description	250	350	450	500	550
Yield (MPa)	-	700	1075	1250	1400	1500
UTS (MPa)	-	870	1150	1392	1600	1740
C03 (MPa)	Model constant affecting yield	690	1003	1203	1300	1403
C09 (MPa)	Kinematic hardening modulus	4416	4416	4416	5216	6016
C15 (MPa)	Isotropic Hardening modulus	700	700	700	1000	1300

4.2.4.6 Design of Experiments

A design of experiments (DOE) technique was used to assess the sensitivity of residual projectile velocity to six microstructure and mechanical properties. Due to the nonlinear relationship between hardness and ballistic merit observed Mescall and Rogers (1989), each parameter was assigned five possible levels, the bounds of which are discussed in previous sections. A finite element simulation of the impact event was

simulated for each unique parameter set and, in each instance, the predicted residual velocity was recorded. The DOE orthogonal array is the $L_{25}(5^6)$, or L25, array which allows up to six independent parameters with five levels. A full factorial set of calculations would require $5^6 = 15,625$ separate calculations, however the L25 array requires only twenty-five. Similar DOE based computational approaches for studying void growth and nucleation using an ISV constitutive model can be found in Horstemeyer and Ramaswamy (2000) and Horstemeyer *et al.* (2003A).

The DOE approach produces a linear system of equations that may be solved to relate the calculation output response vector $\{\mathbf{R}\}$ to the unknown influence vector $\{\mathbf{A}\}$ through the orthogonal array $[\mathbf{P}]$:

$$[\mathbf{P}]\{\mathbf{A}\} = \{\mathbf{R}\}. \quad (4.15)$$

The components of $[\mathbf{P}]$, $\{\mathbf{R}\}$, and $\{\mathbf{A}\}$ are described in Taguchi (1987) as:

$$[\mathbf{P}] = \begin{bmatrix} +1.0 & +1.0 & +1.0 & +1.0 & +1.0 & +1.0 \\ +1.0 & +0.5 & +0.5 & +0.5 & +0.5 & +0.5 \\ +1.0 & 0 & 0 & 0 & 0 & 0 \\ +1.0 & -0.5 & -0.5 & -0.5 & -0.5 & -0.5 \\ +1.0 & -1.0 & -1.0 & -1.0 & -1.0 & +1.0 \\ +0.5 & +1.0 & +0.5 & 0 & -0.5 & -1.0 \\ +0.5 & +0.5 & 0 & -0.5 & -1.0 & +1.0 \\ +0.5 & 0 & -0.5 & -1.0 & +1.0 & +0.5 \\ +0.5 & -0.5 & -1.0 & +1.0 & +0.5 & 0 \\ +0.5 & -1.0 & +1.0 & +0.5 & 0 & -0.5 \\ 0 & +1.0 & 0 & -1.0 & +0.5 & -0.5 \\ 0 & +0.5 & -0.5 & +1.0 & 0 & -1.0 \\ 0 & 0 & -1.0 & +0.5 & -0.5 & +1.0 \\ 0 & -0.5 & +1.0 & 0 & -1.0 & +0.5 \\ 0 & -1.0 & +0.5 & -0.5 & +1.0 & 0 \\ -0.5 & +1.0 & -0.5 & +0.5 & -1.0 & +0.5 \\ -0.5 & +0.5 & -1.0 & 0 & -0.5 & 0 \\ -0.5 & 0 & +1.0 & -0.5 & -1.0 & -0.5 \\ -0.5 & -0.5 & +0.5 & -1.0 & +1.0 & -1.0 \\ -0.5 & -1.0 & 0 & +1.0 & +0.5 & +1.0 \\ -1.0 & +1.0 & -1.0 & -0.5 & 0 & +0.5 \\ -1.0 & +0.5 & +1.0 & -1.0 & -0.5 & 0 \\ -1.0 & 0 & +0.5 & +1.0 & -1.0 & -0.5 \\ -1.0 & -0.5 & 0 & +0.5 & +1.0 & -1.0 \\ -1.0 & -1.0 & -0.5 & 0 & +0.5 & +1.0 \end{bmatrix}, \quad \mathbf{R} = \begin{bmatrix} R_1 \\ R_2 \\ R_3 \\ R_4 \\ R_5 \\ R_6 \\ R_7 \\ R_8 \\ R_9 \\ R_{10} \\ R_{11} \\ R_{12} \\ R_{13} \\ R_{14} \\ R_{15} \\ R_{16} \\ R_{17} \\ R_{18} \\ R_{19} \\ R_{20} \\ R_{21} \\ R_{22} \\ R_{23} \\ R_{24} \\ R_{25} \end{bmatrix}, \quad \mathbf{A} = \begin{bmatrix} A_1 \\ A_2 \\ A_3 \\ A_4 \\ A_5 \\ A_6 \end{bmatrix}. \quad (4.16)$$

In the orthogonal matrix $[\mathbf{P}]$ values of +1, +0.5, 0, -0.5, and -1 represent levels 1, 2, 3, 4, and 5, respectively. The values of each column of $[\mathbf{P}]$ are selected such that the inner product between any two columns is zero, satisfying the orthogonality condition. Orthogonality of $[\mathbf{P}]$ ensures that each value of $\{\mathbf{A}\}$ uniquely describes test result sensitivity to one test variable (columns of $[\mathbf{P}]$). For the sake of clarity, Table 4.4 maps each parameter's respective values to the levels used to populate $[\mathbf{P}]$.

Table 4.4 Levels for microstructure and material properties used in parametric sensitivity study.

Parameter	Parameter Levels				
	+1	+0.5	0	-0.5	-1
Particle No. Density (#/mm²)	250	500	1000	2000	4000
Particle Diameter (μm)	0.1	0.5	1.0	5.0	10.0
Grain Diameter (μm)	1.0	5.0	10.0	50.0	100.0
Initial Porosity	10 ⁻⁶	10 ⁻⁵	10 ⁻⁴	10 ⁻³	10 ⁻²
Lattice Hydrogen (APPM)	10 ⁻⁵	10 ⁻⁴	2.5·10 ⁻⁴	5·10 ⁻⁴	10 ⁻³
Brinell Hardness	250	350	450	500	550

In order to determine the value of $\{\mathbf{A}\}$, the inverse of $[\mathbf{P}]$ was multiplied by both sides of Eq. (4.15). Since $[\mathbf{P}]$ is a non-square matrix of dimensions $m \times n = 25 \times 6$, where $m (25) > n (6)$, the inverse of $[\mathbf{P}]$ is formulated as the left inverse matrix, that is:

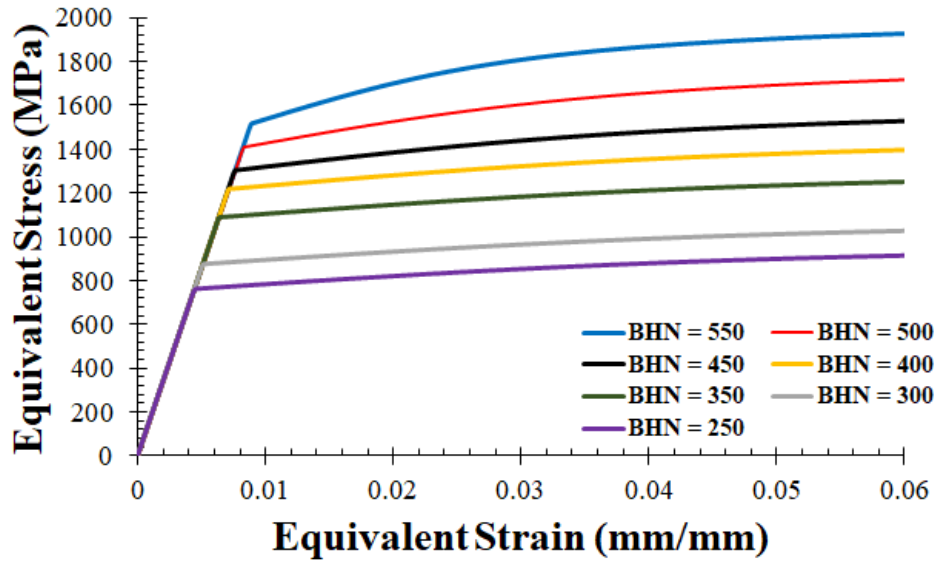
$$[\mathbf{P}]_{left}^{-1} = ([\mathbf{P}]^T[\mathbf{P}])^{-1}[\mathbf{P}]^T = \quad (4.17)$$

Therefore, the solution for $\{\mathbf{A}\}$ is given as:

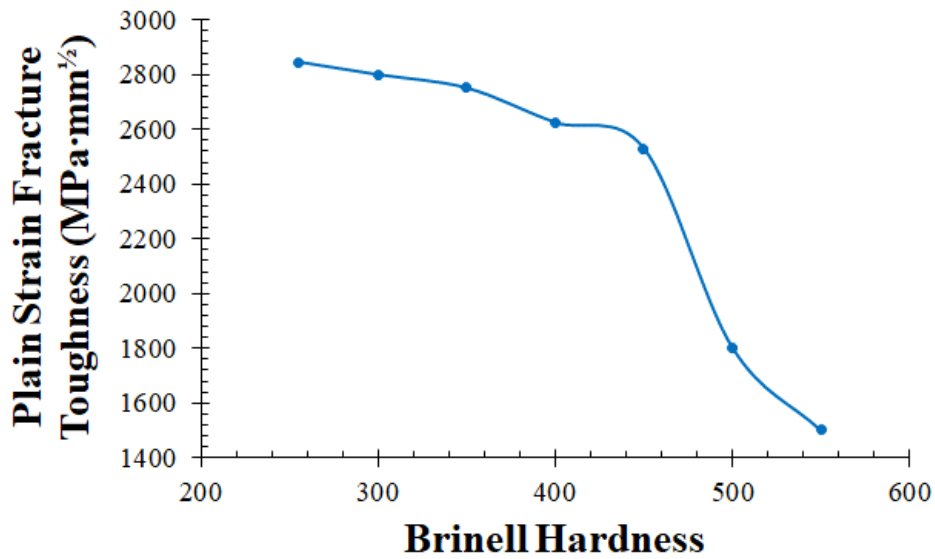
$$\mathbf{A} = [\mathbf{P}]_{left}^{-1}\mathbf{R}. \quad (4.18)$$

4.2.5 Part III. Modeling the Microstructurally Driven Transition of Penetration Modes for Increasing Material Hardness

In general, literature has shown a strong correlation between increasing mechanical strength and ballistic performance of target materials (Manganello, 1967; Goldsmith *et al.* 1971; Goldsmith and Finnegan, 1986; Littlefield *et al.* 1997). However, Mescal and Rogers (1989) and later Dikshit *et al.* (1995) and (for blunt projectiles only) Dey *et al.* (2004) observed that the ballistic performance of steel target plates diminished after a certain hardness or strength threshold (usually greater than 400 BHN). Mescal and Rogers (1989) attributed the decrease in ballistic performance to a transition in penetration modes from large plasticity driven rupture at low hardness to plugging (Backman and Goldsmith, 1978) driven by localization phenomena (adiabatic shear band nucleation, propagation, and fracture) at high hardness. The Abaqus Explicit FEA framework for cylinders impacting semi-infinite plates discussed in Part II was used for this study (Part III). Microstructure and mechanical properties of a 4340-steel alloy were varied for hardness values ranging from 250-550 BHN. Figure 4.3 shows the stress-strain behavior (Fig. 4.3a) and fracture toughness (Fig. 4.3b) of 4340 steel, which satisfies RHA steel performance specifications by MIL-A-12560H (US Military, 1990), over a 250-550 BHN range using data compiled from Bhat (1977) and Horn and Ritchie (1978). For 4340 steel, both yield and flow stress increase with hardness, however the material's fracture toughness drastically decreases above 400 BHN (Bhat, 1977; Horn and Ritchie 1978).



(a)



(b)

Figure 4.3 ISV model mechanical and fracture toughness properties of varying Brinell hardness rolled 4340 Steel alloys experimentally characterized by Bhat (1977) and Horn and Ritchie (1978).

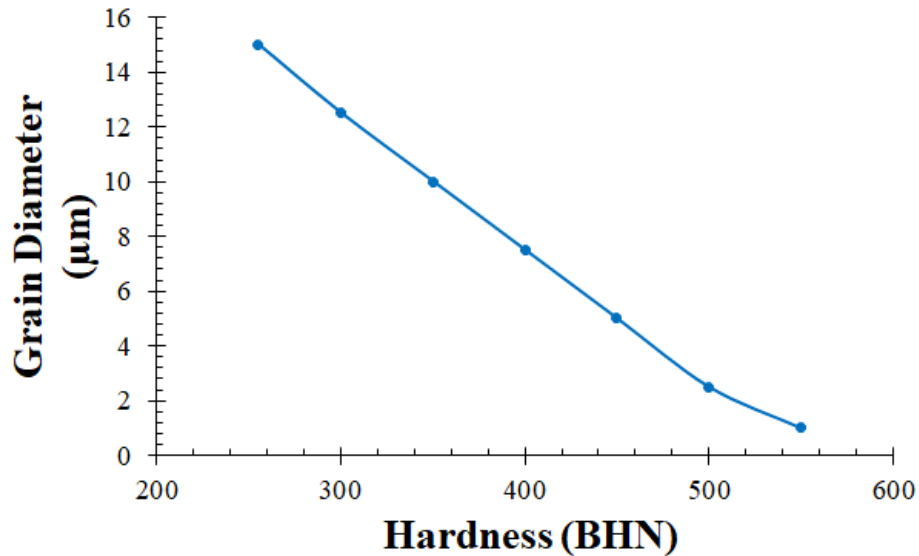
(a) Equivalent stress versus equivalent strain for varying hardness 4340 steel.

(b) Fracture toughness versus hardness for 4340 steel.

The microstructure properties selected for variation include initial particle number density, η_0 , particle size, d , particle volume fraction, f , grain size, GS . Literature sources (Baker *et al.* 1965; Parker and Zackay, 1975; Horn and Ritchie, 1978; Cowie and Azrin, 1990; Ayer and Machmeier, 1993) qualitatively suggest that lower quench rates and higher tempering temperatures lead to a coarsening of second phase particles and precipitates accompanied by a reduction in undissolved carbides. Unfortunately, little of the published literature quantitatively compares second phase particle, precipitate, and carbide properties to hardness or material processing histories for steels. Nevertheless, the higher quench rates and lower tempering temperatures necessary for achieving high volume fraction martensitic grain steels could plausibly result in fine, relatively high number density heterogeneity distributions. Grain size is correlated to thermomechanical processing temperature and time due to recrystallization (Doherty *et al.* 1997). Grain size and hardness are inversely correlated for a given steel alloy, consistent with the findings of Hall (1951) and Petch (1953). These qualitative trends were applied in varying the particle number density, particle size, and grain size with hardness for this study. Particle volume fraction was calculated as a function of size and number density using Eq. (4.14). Specific values for each microstructure property were carefully selected in order to qualitatively predict the perforation mode and ballistic performance trends discussed in Mescall and Rogers (1989).

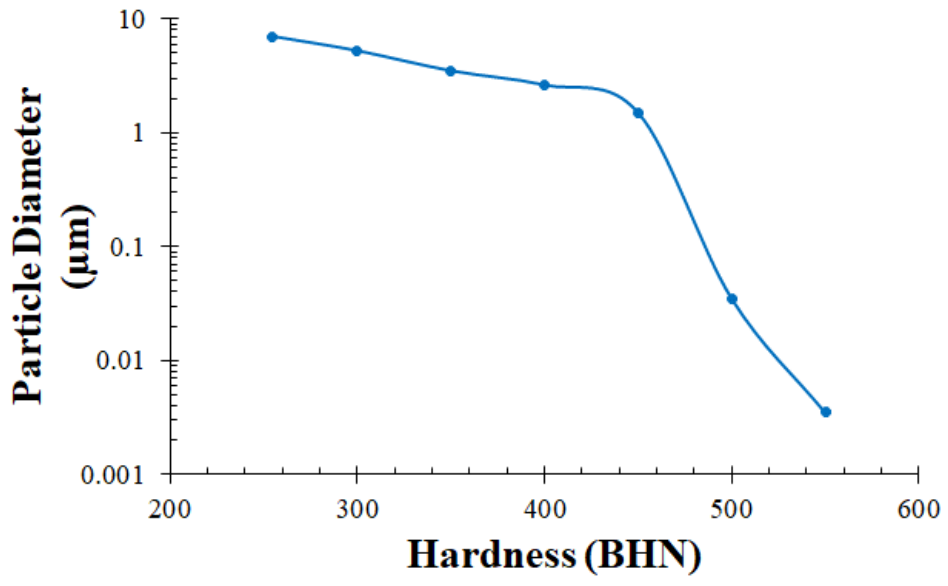
The value of each microstructure property versus material hardness is included in Fig. 4.4. The bounds for the grain diameter range (1-15 μm) was selected based on literature quantifications of high strength steel microstructures (0.1-1 μm Takaki *et al.* 2001; 12 μm

in Whittington *et al.* 2014). Similarly, the bounds for particle number density (200-4000 particles/mm²) has basis in the steel literature findings contained in Table 4.2. Second phase particle diameters in steel can vary widely from ~10 μm (Cox and Lowe, 1974) to less than 5 nm (Ayer and Machmeier, 1993) which were selected as the particle diameter bounds for this study. Future efforts to validate this framework would benefit from quantitative microstructural characterizations of RHA steel alloys over the 250-550 BHN range to develop physically representative ISV model calibrations.

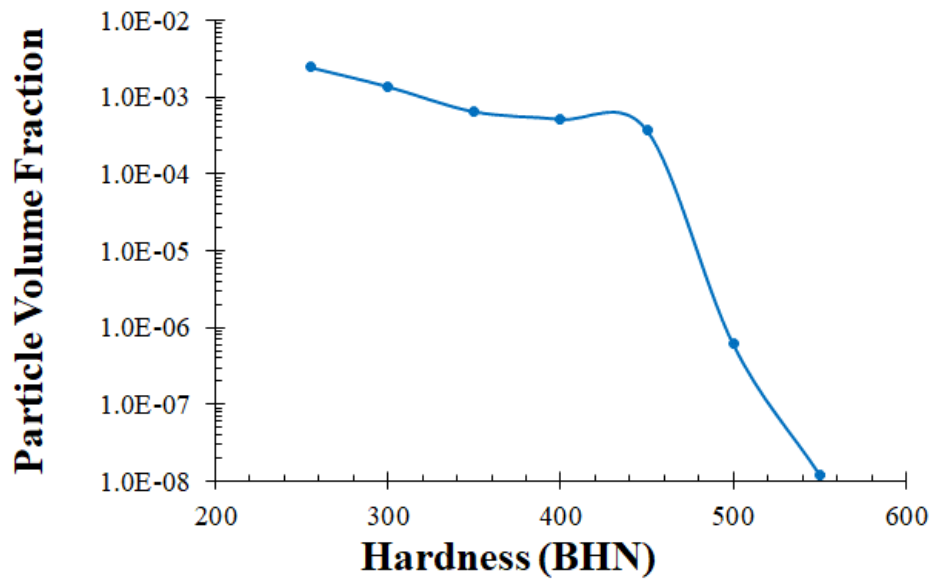


(a)

Figure 4.4 Microstructure properties at varying hardness levels of RHA steel alloy.

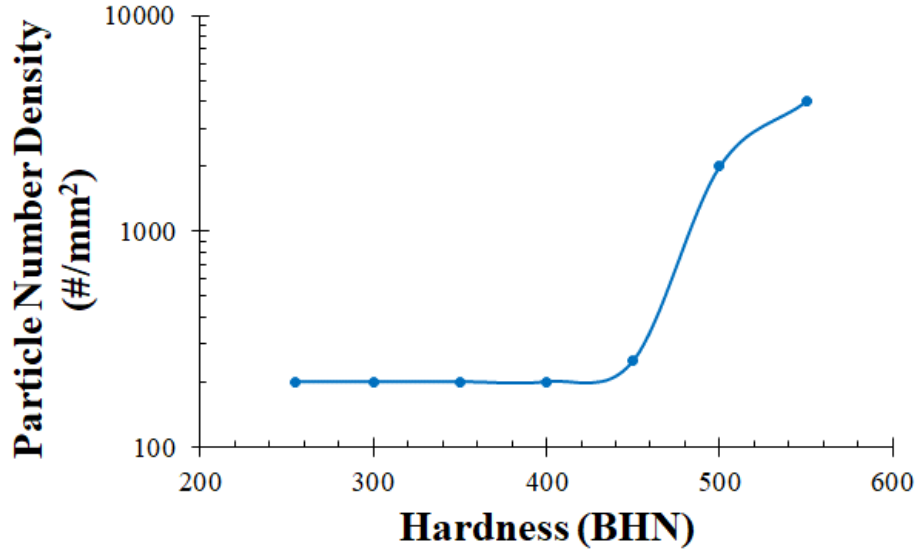


(b)



(c)

Figure 4.4 (continued)



(d)

Figure 4.4 (continued)

- (a) Grain diameter versus hardness.
- (b) Second phase particle diameter versus hardness.
- (c) Second phase particle volume fraction versus hardness.
- (d) Second phase particle number density versus hardness.

A complete listing of the ISV model constants for each BHN level RHA material is included in Table B.2. The complete perforation velocity of each material system was determined as used as a metric for evaluating ballistic performance through Eq. (4.19):

$$M = V_p / V_{p0}, \quad (4.19)$$

where M represents ballistic merit, V_p is the perforation velocity of the current material system and is normalized by a nominal perforation velocity (taken to be V_p at 250 BHN), V_{p0} .

4.3. Results and Discussion

4.3.1 Part I: Validation of Internal State Variable Finite Element Framework

Finite element simulations of ballistic impact of RHA steel plates of varying thickness by 12.7 mm diameter RHA steel spheres were performed to demonstrate the usefulness of ISV based constitutive models for predicting ballistic performance of materials. The ISV model coefficients for the 250 BHN RHA steel alloy used in the study is contained in Table B.1. Numerical simulation results are compared to experimental data generated by ERDC in Fig. 4.5. Figure 4.5 demonstrates agreement between simulation predictions and experimental data for complete perforation and residual projectile velocities. In Fig. 4.5, both experimental and numerical residual velocity data appears to follow a parabolic, concave downward shape with increasing initial projectile velocity consistent with literature findings (Anderson *et al.* 1992; Littlefield *et al.* 1997; Anderson *et al.* 1999; Børvik *et al.* 2001; Børvik *et al.* 2003; Dey *et al.* 2004). The FEA model prediction strongly agrees with experimentally determined perforation velocity of the 9.53 mm thick plate (experimental V50 = 754 m/s) and under predicts the perforation velocity of the 12.7 mm thick plate by only 5.7 percent (1150 m/s predicted, 1218.6 m/s observed). The shapes of the predicted residual velocity curves generally agree with experimental residual velocity data as well. Therefore, the ISV constitutive model can be confidently used within a Lagrangian FEA framework to predict behaviors of materials during high velocity impacts.

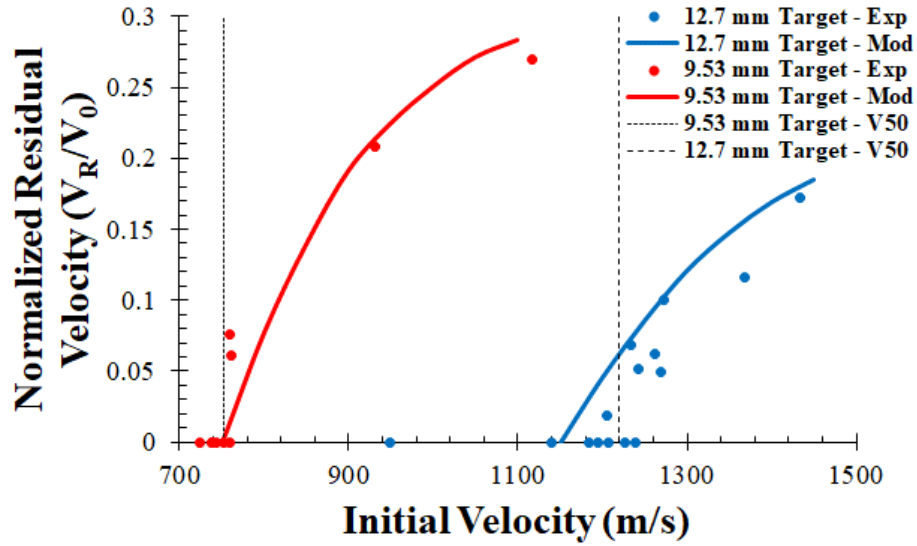


Figure 4.5 Comparison of experimental and finite element model predicted normalized residual velocities for RHA steel spheres impacting RHA steel plates.

4.3.2 Part II: Parameter Sensitivity Study

Twenty-five simulations of 6.35 mm diameter, 12.7 mm long RHA cylinders impacting 6.35 mm thick RHA steel target plates were performed to assess the effect of (1) particle number density, (2) particle size, (3) grain size, (4) initial void volume fraction, (5) lattice hydrogen concentration, and (6) mechanical hardness on projectile residual velocity. The residual velocity results for 25 simulations included in Fig. 4.6 were used to populate the $\{\mathbf{R}\}$ array. The data in Fig. 4.6 was used in conjunction with the parameter levels matrix $[\mathbf{P}]$ to solve Eq. (4.18) and determine the sensitivity of residual velocity to parameters (1)-(6). The results of the parameter sensitivity array $\{\mathbf{A}\}$ were normalized by the maximum value of $\{\mathbf{A}\}$ and are shown in Fig. 4.7.

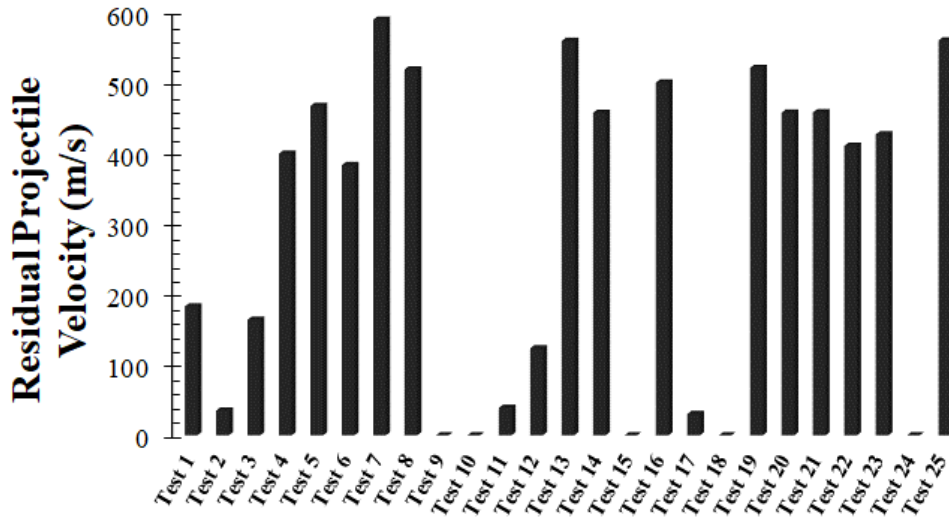


Figure 4.6 Residual velocity results of 25 impact simulations used to populate array $\{R\}$ in parametric sensitivity study.

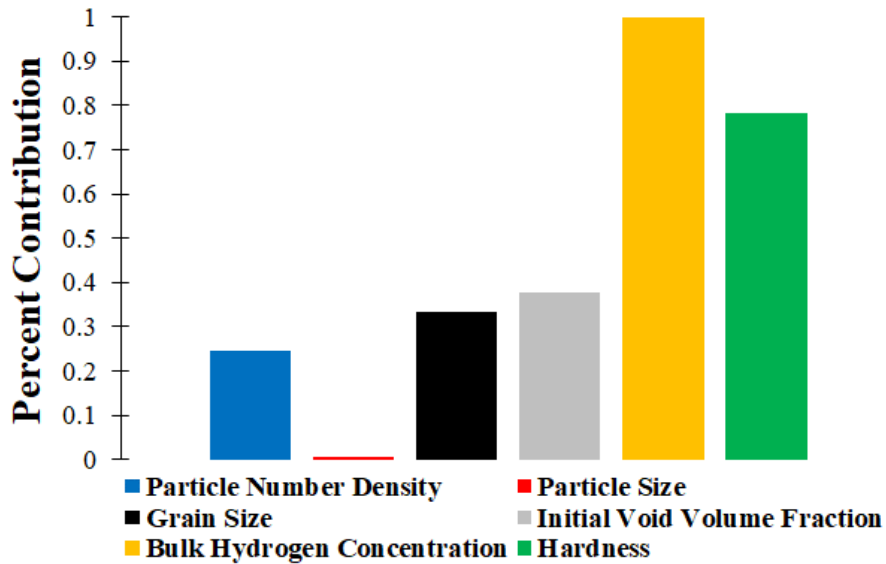


Figure 4.7 Comparison of residual velocity sensitivity to six parameters for an RHA steel cylinder impacting of 6.35 mm thick RHA steel target.

Figure 4.7 shows that for the parameter ranges studied, lattice hydrogen concentration is the dominant factor affecting projectile residual velocity while mechanical hardness plays a substantial secondary role (0.78 normalized contribution). Sufficiently high levels of lattice hydrogen concentration approaching 0.001 APPM results in significant void nucleation rate in materials experiencing tensile pressure. The initial compressive pressure wave is reflected from the target's rear free surface as a high amplitude tensile pressure wave (Bowden and Field, 1964; Fugelso and Bloedow, 1966). According to Eq. (4.9)-(4.11), sufficiently hydrogenated materials undergo significant tensile stress induced hydrogen segregation to trapping sites at interfaces (dislocation, void, grain, subgrain, and inclusion boundaries) and experience high void nucleation rates that weaken the target's structural integrity in a matter consistent with literature findings on hydrogen embrittlement (Barnett, 1957; Westlake, 1969; Beachem, 1972; Ferreira *et al*, 1999).

The influence of mechanical hardness on projectile residual velocity is sensible given proper context. Consider materials of differing mechanical strengths but identical failure strains. The stronger material will be able to dissipate the most energy as mechanical energy absorption corresponds to the integral of the stress-strain relationship ($\int_0^\epsilon \sigma d\epsilon$). In the DOE, no specifications were made as to the relationship of hardness or strength to failure strains and damage evolution rates; these properties were assumed to be uncorrelated (a required assumption from Taguchi, 1987) for the sake of establishing the orthogonal matrix [P]. Future studies would benefit from considering the correlation between mechanical strength and ductility. Under these assumptions the normalized

sensitivity of residual velocity to material hardness (A_6) was determined to be 0.78. Thus, material hardness is a strong secondary influence on ballistic performance of metal targets.

Initial void volume fraction, grain size, and particle number density all play tertiary roles with normalized sensitivity contributions of 0.38, 0.33, and 0.24 respectively. Particle size had negligible effects on residual velocity. Table 4.5 was generated to provide additional context for parameter contribution to residual velocity. Specifically, Table 4.5 displays the parameter sets resulting in residual velocities over 500 m/s (representing residual of greater than 50% of initial projectile velocity) and residual velocities of 0 m/s (projectile fully arrested). Significant initial porosity ($\phi_{pore} = 0.01$) in test 8 (see Table 4.5) could be inferred to have played a dominant role in the test's high residual velocity (518.94 m/s) because of the otherwise low lattice hydrogen concentration (10^{-5} APPM) and moderate target and projectile hardness (350 BHN). However, high residual projectile velocities only occurred at initial porosities under 10^{-2} in the presence of either significant lattice hydrogen concentrations (10^{-3} and $5 \cdot 10^{-4}$ APPM in tests 7 and 13, respectively) or low material hardness (250 BHN in tests 7, 13, 18, and 19). Table 4.5 shows no conclusive correlation between particle number density, particle diameter, and grain diameter for tests resulting in the highest and lowest projectile residual velocities.

Table 4.5 Select test parameter levels and resultant residual velocity values from parameter sensitivity study

Test	Particle No. Density (μm)	Particle Diameter (μm)	Grain Diameter (μm)	Initial Porosity	Lattice Hydrogen (APPM)	Brinell Hardness (BHN)	Residual Velocity (m/s)
7	500	0.5	10	10^{-3}	10^{-3}	250	589.60
8	500	1.0	50	10^{-2}	10^{-5}	350	518.94
13	1000	1.0	100	10^{-5}	$5 \cdot 10^{-4}$	250	559.44
19	2000	5.0	5	10^{-2}	$2.5 \cdot 10^{-4}$	250	521.16
25	4000	10.0	50	10^{-4}	10^{-4}	250	560.12
9	500	5.0	100	10^{-6}	10^{-4}	450	0
10	500	10.0	1	10^{-5}	$2.5 \cdot 10^{-4}$	500	0
15	1000	10.0	5	10^{-3}	10^{-5}	450	0
18	2000	1.0	1	10^{-3}	10^{-4}	550	0
24	4000	5.0	10	10^{-6}	10^{-5}	550	0

4.3.3 Part III: Modeling the Microstructurally Driven Transition of Penetration Modes for Varying Target Hardness

Abaqus Explicit finite element simulations were run using an ISV constitutive model for RHA steel alloys of varying mechanical and microstructure properties to demonstrate a microstructurally driven transition in target perforation modes initially discussed in Mescal and Rogers (1989). Figure 4.8 shows images of the cross sectional and rear target surface during perforation for 300, 400, and 500 BHN steel. In Fig. 4.8 the contours represent plastic equivalent strain and grey hues denote regions of material experiencing greater than fifty percent plastic equivalent strain. The figures show a decrease in the cross-sectional area experiencing large strains as BHN levels increase from 300 to 500. Furthermore, perforation of the 300 BHN target (Fig. 4.8a) appears to be driven by ductile rupture due to large plastic deformation while perforation of the 500 BHN target

(Fig. 4.8c) occurs by shear plugging consistent with experimental observations of Mescall and Rogers (1989).

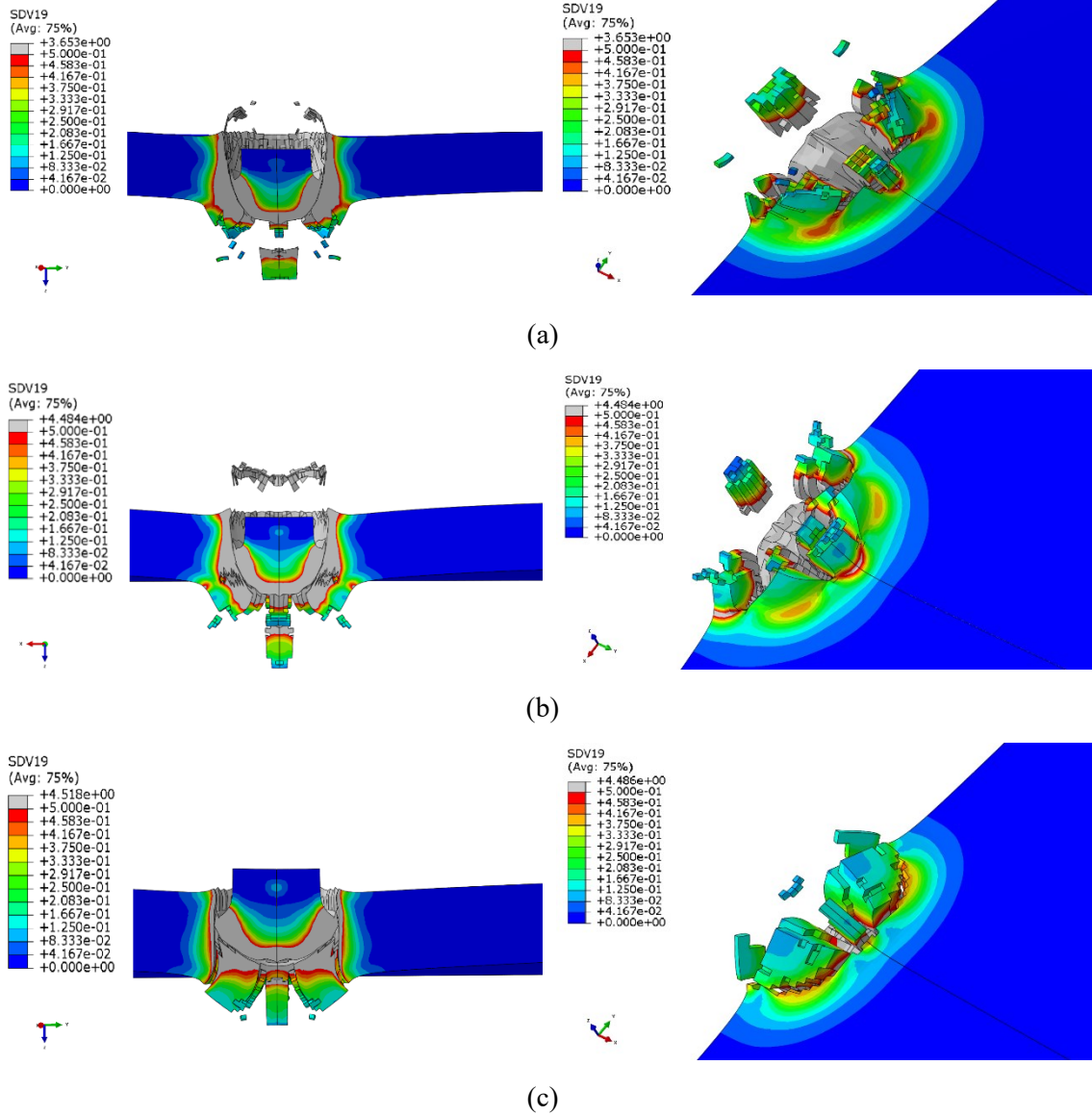


Figure 4.8 Plastic equivalent strain contours for impact perforation of varying Brinell hardness (BHN) rolled homogenous armor steel (RHA) steel plates.

- (a) Finite element simulation of impact of 300 BHN RHA steel plate.
- (b) Finite element simulation of impact of 400 BHN RHA steel plate.
- (c) Finite element simulation of impact of 500 BHN RHA steel plate.

The ballistic merit of each hardness RHA alloy was calculated using minimum perforation velocity data from simulations in part III in conjunction with Eq. (4.19). In this case, the perforation velocity of each material configuration was normalized by the perforation velocity of the 250 BHN material. In Figure 4.9 the predicted ballistic merit behavior for increasing target hardness is compared to ballistic merit data experimentally generated by Mescal and Rogers for vacuum induction melted (VIM) and electroslag remelted (ESR) 6.35 mm 4340 steel plates impacted by 6.35 mm diameter, 12.7 mm long 4340 steel cylinders. Figure 4.9 demonstrates the ISV model's ability to qualitatively predict the decrease in ballistic performance at elevated material hardness given sufficient variation of microstructure properties.

In reference to Figs. 4.3b-4 fracture toughness, grain size, particle size, and particle volume fraction decrease with BHN while particle number density increases. Each of the mechanical and microstructure properties vary in such a way that the ISV model predictions for void nucleation rate in Eq. (4.9) and void coalescence rate in Eq. (4.13) increase with increasing BHN. The increasing rate of damage evolution by Eq. (4.6) and (4.7) leads to strain localization in damage affected elements by the inelastic flow rule in Eq. (4.3). The coupled localization of strain and damage is responsible for the change in predicted perforation modes in Fig. 4.8 from rupture due to large plasticity at low BHN values (BHN less than 450) to shear plugging at high BHN values (BHN greater than 450). The microstructure and material property driven transition to highly localized straining and damage evolution diminishes high BHN material's ability to effectively dissipate impact energy through large regions of plastic strain. The ultimate result is the qualitatively

predicted trend of diminishing ballistic performance of high hardness plates consistent with the results of Mescall and Rogers (1989). This predicted tendency is a result of an ISV model framework predicated upon idealized property assumptions for varying hardness materials. A true validation of this framework requires thorough microstructure and mechanical property characterizations of several hardness classes of steels and subsequent calibration of high-fidelity ISV constitutive models.

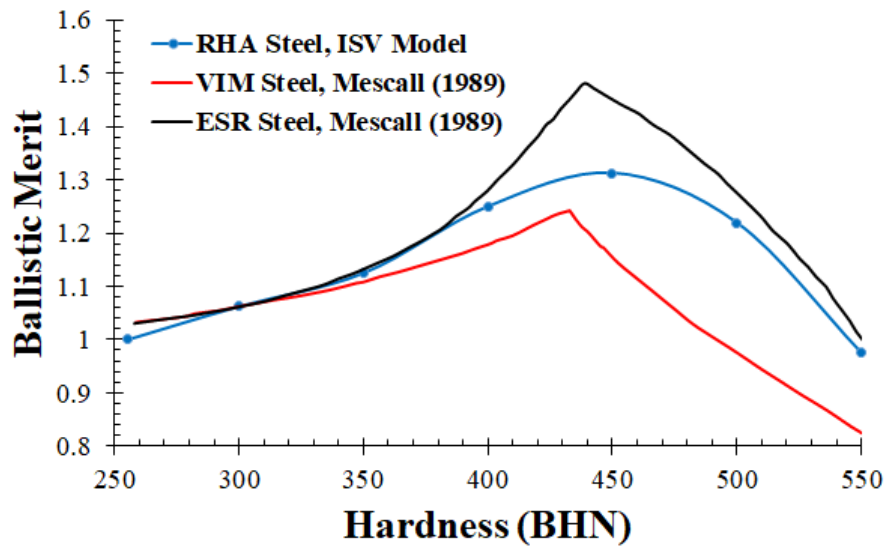


Figure 4.9 Comparison of Ballistic Merit for varying hardness experimentally impacted 4340 steel alloys (Mescall and Rogers, 1989) and simulated RHA steel.

4.4 Conclusions

Simulations of ballistic impact of spherical and cylindrical shaped rolled homogeneous armor steel (RHA) projectiles against semi-infinite RHA target plates have been performed within an Abaqus Explicit finite element analysis (FEA) framework using

internal state variable (ISV) based constitutive models. The effects of varying microstructure and mechanical properties on projectile residual velocity have been assessed in a parametric sensitivity study. The tendency for high hardness steel targets to exhibit reduced ballistic performance has been qualitatively predicted by FEA simulations given sufficient variation of microstructure and material properties. The following definitive conclusions can be made:

1. The ISV model framework has been validated through satisfactory agreement between FEA simulation predictions and experimental data for spherical projectile impacts.
2. A parametric sensitivity study measuring the effects of (1) particle number density, (2) particle size, (3) grain size, (4) initial void volume fraction, (5) lattice hydrogen concentration, and (6) material hardness demonstrates that hydrogen concentration and material hardness significantly influence residual projectile velocity. Particle number density, grain size, and initial void volume fraction are shown to be secondary influences on residual projectile velocity.
3. Diminished ballistic performance of high hardness targets experimentally observed by Mescall and Rogers (1989) can be qualitatively predicted using an ISV based framework featuring decreasing grain size, particle size, particle volume fraction, and fracture toughness and increasing particle number density with increasing material hardness in accord with qualitative trends documented in relevant literature.

CHAPTER V

SUMMARY AND FUTURE WORK

An Internal State Variable (ISV) constitutive model has been modified to consider shear influenced void growth for ductile metals. Void coalescence has been posed as a functional of an evolving Intervoid Ligament Distance enabling the meaningful prediction of the microstructural state of a material at which void coalescence appreciably affects the rate of void volume fraction evolution.

The ISV model was calibrated for an aluminum 7085-T711 alloy to characterize the material's mechanical behavior and microstructural evolution during deformation. The ISV model revisions are validated through accurate, finite element analysis (FEA) prediction mechanical behavior and damage evolution for a variety of structural deformations at varying stress states and temperatures. Finite element simulations featuring heterogeneous distributions of microstructure properties demonstrate the ISV model framework's capability to predict the "cup-cone" fracture phenomena in Al 7085 notched tension specimens.

Simulations of ballistic impact of rolled homogeneous armor (RHA) steel alloys have been performed using the ISV model within an Abaqus-Explicit FEA framework.

The model framework was validated through successfully predicting perforation velocity and residual velocity characteristics of RHA steel spheres impacting RHA steel plates of multiple thicknesses. A simulation based parametric study was performed to determine sensitivity of ballistic residual velocity to microstructure and mechanical properties. The study demonstrated that elevated lattice hydrogen concentrations and low mechanical hardness significantly increase perforation velocity due to reduction of ductility and reduced energy absorption capacity, respectively. A final simulation-based study showed that the literature documented reduction in ballistic performance of high hardness steels can be attributed an evolution of microstructure properties with increasing hardness. Specifically, the increase in second phase particle number density and decrease in grain size increases the material's void nucleation and growth rates, respectively. The increased rate of damage evolution leads to localization of fracture and results in a transition from rupture due to large aggregate plasticity to perforation by shear plugging phenomena.

The studies discussed in Chapters II-IV create several avenues for future potential research. The kinematic, thermodynamic, and kinetic foundations of the Internal State Variable (ISV) model should be continually refined with supporting experimental findings to account for influential microstructure-property effects within a generalized framework. The following points discuss potential future work regarding the ISV model and its application.

1. The ability to model microstructure property spatial distributions in materials should be addressed using supporting experimental methods (microscopy and x-ray computed tomography) to generate statistically representative spatial property

- distributions. Modeling accurate heterogeneity distribution throughout material structures may enable the ISV model to make high fidelity predictions of plasticity and damage evolution.
2. Nonlocal spatial gradient and Laplacian terms should be introduced to the void coalescence relations to represent the physical mechanisms of void sheeting and impingement, respectively. In a finite element framework, the nonlocal higher order operators nullify mesh sensitivity effects, thus allowing confident prediction of strain and damage localization.
 3. True validation of the relationship between void nucleation, growth, and coalescence relations may be accomplished by comparison of model predictions to deformation experiments using scanning electron microscopes or x-ray computed tomography for in-situ observation of microstructure evolution.
 4. A design of experiments (DOE) approach using the ISV constitutive model can be applied to finite element simulations of high velocity impacts of metals to determine the effects of layer properties of multilayer structures to determine optimal configurations for impact resistance.
 5. The effects of microstructure-mechanical property relationships on ballistic performance of monolithic alloy targets (qualitatively performed in Part III of Chapter IV) should be examined using material systems experimentally characterized expressly for the study. This would enable quantitative correlation of microstructure and mechanical properties to structural performance and provide

a quantitative assessment of the viability of the ISV model framework within the problem domain.

REFERENCES

- Abramoff, M.D., Magalhaes, P.J., Ram, S.J., "Image Processing with ImageJ," *Biophotonics International*, Vol. 11, No. 7, 2004, pp. 36-42.
- Agarwal, H., Gokhale, A.M., Graham, S., Horstemeyer, M.F., "Void Growth in 6061-Aluminum Alloy Under Triaxial Stress State," *Materials Science and Engineering: A*, Vol. 341, No. 1, 2003, pp. 35-42.
- Aifantis, E.C., "On the Role of Gradients in the Localization of Deformation and Fracture," *International Journal of Engineering Science*, Vol. 30, No. 10, 1992, pp. 1279-1299.
- Allison, P.G., *Structure-Property Relations for Monotonic and Fatigue Loading Conditions for a Powder Metal Steel*, Dissertation, Mississippi State University, 2009.
- Allison, P.G., "Plasticity and fracture modeling/experimental study of a porous metal under various strain rates, temperatures, and stress states," *Journal of Engineering Materials and Technology*, Vol. 135, No. 4, 2013.
- Al-Rub, R.K.A, Voyiadjis, G.Z., "A Direct Finite Element Implementation of the Gradient-Dependent Theory," *International Journal of Numerical Methods in Engineering*, Vol. 63, No. 4, pp. 603-629.
- Al-Rub, R.K.A., Darabi, M.K., Masad, E.A., "A Straightforward Numerical Technique for Finite Element Implementation of Non-local Gradient-dependent Continuum Damage Mechanics Theories," *International Journal of Theoretical and Applied Multiscale Mechanics*, Vol. 1, No. 4, 2010, pp. 352-385.
- Anderson, P. M., Fleck, N. A., Johnson, K. L., "Localization of Plastic Deformation in Shear Due to Microcracks," *J. Mech. Phys. Solids*, Vol. 38, No. 5, 1990, pp. 681-699.
- Anderson, C.E., Morris, B.L., Littlefield, D.L., *A penetration mechanics database*, No. SWRI-3593/001. Southwest Research Inst. San Antonio TX, 1992.

Anderson, C.E., Hohler, V., Walker, J.D, Stilp, A.J., "The influence of projectile hardness on ballistic performance," *International Journal of Impact Engineering*, Vol. 22, No. 6, 1999, pp. 619-632.

Anurag, S., Guo, Y.B., Horstemeyer, M.F., "The effect of materials testing modes on finite element simulation of hard machining via the use of internal state variable plasticity model coupled with experimental study," *Computers and Structures*, Vol. 87, No. 5-6, 2009, p. 303-317. DOI: <https://doi.org/10.1016/j.compstruc.2009.01.001>

Asaro, R.J., Rice, J.R. "Strain Localization in Ductile Single Crystals," *J. Mech. Phys. Solids*, Vol. 25, No. 5, 1977, pp. 309-338.

ASM Handbook, Properties, "Selction: Nonferrous Alloys and Special Purpose Materials, Vol. 2," *ASM International*, Materials Park, OH (1990)

ASTM, E. "1382-97," *Standard Test Methods for Determining Average Grain Size Using Semiautomatic and Automatic Image Analysis*, 1997.

Awerbuch, J., and S.R., Bodner, "Analysis of the Mechanics of Perforation of Projectiles in Metallic Plates," *International Journal of Solids and Structures*, Vol. 10, No. 6, 1974, pp. 671-684.

Ayer, R., Machmeier, P.M., "Transmission electron microscopy examination of hardening and toughening phenomena in Aermet 100," *Metallurgical Transactions A*, Vol. 24, No. 9, 1993, pp. 1943-1955.

Backman, M.E., Goldsmith, W., "The Mechanics of Penetration of Projectiles into Targets," *International Journal of Engineering Science*, Vol. 16, No. 1, 1978, pp. 1-99.

Bai, Y., "Effect of Loading History on Necking and Fracture," Department of Mechanical Engineering, Massachusetts Institute of Technology, February 2008.

Bai, Y., Wierzbicki, T., "A new model of metal plasticity and fracture with pressure and Lode dependence," *International Journal of Plasticity*, Vol. 24, 2008, pp. 1071-1096.

Bai, Y., Wierzbicki, T., "Application of extended Mohr-Coulomb criterion to ductile fracture," *Int. J. Fract.* Vol. 161, 2010, pp. 1-20

Baker, A., Lauta, F., Wei, R., "Relationships Between Microstructure and Toughness in Quenched and Tempered Ultrahigh-Strength Steels," *Structure and Properties of Ultrahigh-Strength Steels*, ASTM International, 1965.

Baker, W.E., Yew, C.H., "Strain-rate effects in the propagation of torsional plastic waves," *Journal of Applied Mechanics*, Vol. 33, No. 4, 1966, pp. 917-923.

- Bammann, D.J., "An Internal Variable Model of Viscoplasticity," *International Journal of Engineering Science*, Vol. 22, No. 8-10, 1984, pp. 1041-1053.
- Bammann, D.J., Johnson, G.C., "On the Kinematics of Finite-Deformation Plasticity," *Acta Mechanica*, Vol. 70, No. 1-4, 1987, pp. 1-13.
- Bammann, D.J., Aifantis, E.C., "A Damage Model for Ductile Metals," *Nuclear Engineering and Design*, Vol. 116, No. 3, 1989, pp. 355-362.
- Bammann, D.J., Chiesa, M.L., Horstemeyer, M.F., Weingarten, L.I., "Failure in Ductile Porous Metals," *Fracture Behavior and Design of Materials and Structures*, Vol. 1, Proceedings of the 8th European Conference on Fracture, Firrao, D., Ed., 1993, pp. 1-54.
- Bammann, D.J., Chiesa, M.L., Horstemeyer, M.F., Weingarten, L.I., Wierzbicki, N.J.A.T., "Structural Crashworthiness and Failure," *Applied Science (Elsevier, London, 1993)*, 1993.
- Bammann, D.J., Chiesa, M.L., Johnson, G.C., "Modeling Large Deformation and Failure in Manufacturing Processes." *Theoretical and Applied Mechanics*, Vol. 9, 1996, pp. 359-376.
- Bammann, D.J., Solanki, N.K., "On kinematic, thermodynamic, and kinetic coupling of a damage theory for polycrystalline material," *International Journal of Plasticity*, Vol. 26, No. 6, 2010, pp. 775-793.
- Banthia, N., Mindess, S., Bentur, A., Pigeon, M., "Impact Testing of Concrete using a Drop-Weight Impact Machine," *Experimental Mechanics*, Vol. 29, No. 1, 63-69, 1989.
- Bao, Y., Wierzbicki, T., "On fracture locus in the equivalent strain and stress triaxiality space," *International Journal of Mechanical Sciences*, Vol. 46, 2004A, pp. 81-98.
- Bao, Y., Wierzbicki, T., "A comparative study on the various ductile crack forming criteria," *Journal of engineering materials and technology*, Vol. 126, No. 3, 2004B, pp. 314-324.
- Barnett, W.J., Troiano, A.R., "Crack propagation in the hydrogen-induced brittle fracture of steel," *JOM*, Vol. 9, No. 4, 1957, pp. 486-494.
- Beacham, C.D., "A new model for hydrogen-assisted cracking (hydrogen "embrittlement")." *Metallurgical Materials Transactions B*, Vol. 3, No. 2, 1972, pp. 441-455.
- Begley, J.A., Landes, J.D., "The J integral as a fracture criterion," *Fracture Toughness: Part II*, ASTM International, 1972.

Benk, R.F., *Quasi-Static Tensile Stress Strain Curves—II, Rolled Homogeneous Armor*, No. BRL-MR-2703, Army Ballistic Research Lab Aberdeen Proving Ground MD, 1976.

Benk, R.F., Robitaille, J.L., *Tensile Stress-Strain Curves—III, Rolled Homogeneous Armor at a Strain Rate of 0.042 Per Second*, No. BRL-MR-2760, Army Ballistic Research Lab Aberdeen Proving Ground MD, 1977.

Bhat, M.S., “Microstructure and Mechanical Properties of AISI 4340 Steel Modified with Aluminum and Silicon,” Dissertation, University of California Berkley, 1977.

Bhattacharyya, J.J., Agnew, S.R., Lee, M.M., Whittington, W.R., El Kadiri, H., “Measuring and Modeling the Anisotropic, High Strain Rate Deformation of Al alloy, 7085, Plate in T711 Temper,” *International Journal of Plasticity*, Vol. 93, pp. 46-63, 2017.

Bhattacharyya, J.J., Bittmann, B., Agnew, S.R., “The Effect of Precipitate-Induced Backstresses on Plastic Anisotropy: Demonstrated by Modeling the Behavior of Aluminum Alloy, 7085,” *International Journal of Plasticity*, 2018.

Boehler J.P., Demmerle, S., Koss, S., “A New Direct Biaxial Testing Machine for Anisotropic Materials,” *Experimental Mechanics*, Vol. 34, No. 1, 1994, pp. 1-9.

Børvik, T., Langseth, M., Hopperstad O.S., Malo, K.A., “Ballistic Penetration of Steel Plates,” *International Journal of Impact Engineering*, Vol. 22, No. 9-10, 1999, pp. 855-886.

Børvik, T., Hopperstad, O.S., Berstad, T., Langseth, M., “A computational model of viscoplasticity and ductile damage for impact and penetration,” *European Journal of Mechanics-A/Solids*, Vol. 20, No. 5, 2001, pp. 685-712.

Børvik, T., Hopperstad, O.S., Langseth, M., Malo, K.A., “Effect of target thickness in blunt projectile penetration of Weldox 460 E steel plates,” *International journal of impact engineering*, Vol. 28, No. 4, 2003, 413-464.

Bourcier, R.J., Koss, D.A., *Ductile Fracture Under Multiaxial Stress States between Pairs of Holes*, No. 11, TR-11, Michigan Technological University Houghton Department of Metallurgical Engineering, 1979.

Bouvard, J.L., Francis, D.K., Tschopp, M.A., Marin, E.B., Bammann, D.J., Horstemeyer, M.F., “An Internal State Variable Material Model for Predicting the Time, Thermomechanical, and Stress State Dependence of Amorphous Glassy Polymers Under Large Deformation,” *International Journal of Plasticity*, Vol. 42, 2013, pp. 168-193.

Bowden, F.P., Field, J.E., "The Brittle Fracture of Solids by Liquid Impact, by Solid Impact, and by Shock," *Proceedings of the Royal Society of London A: Mathematical, Physical and Engineering Sciences*, Vol. 282, No. 1390, The Royal Society, 1964, pp. 331-352.

Bridgman, P. W., *Proc. Am. Acad. Arts Sci.*, vol. 58, 1923, pp. 163.

Bridgman, P.W., "The stress distribution at the neck of a tension specimen," *Trans. ASM* 32, 1944, pp. 553-574.

Brown, L.M., Embury, J.D., "The initiation and growth of voids at second phase particles," *Proc. 3rd Int. Conf. on Strength of Metals and Alloys*, Inst. Of Metals, London, 1973, pp. 164-169.

Browne, R.J., Flewitt, P.G.J., Lansdale, D., Shammass, M.S., Soo, J.N., "Multiaxial Creep of Fire-Grained 1 Cr-0.5 Mo Steels," *Materials Science and Technology*, Vol. 7, 1991, pp. 707-717.

Budiansky, B., Hutchinson, J.W., Slutsky, S., *Void Growth and Collapse in Viscous Solids*, Pergamon Press, London, 1982.

Camacho, G.T., Ortiz, M., "Computational Modelling of Impact Damage in Brittle Materials," *International Journal of Solids and Structures*, Vol. 33, No. 20-22, 1996, pp. 2899-2938.

Chandler, M.Q., Horstemeyer, M.F., Baskes, M.I., Wagener, G.J., Gullett, P.M., Jelinek, B., "Hydrogen effects on nanovoid nucleation at nickel grain boundaries," *Acta Materialia*, Vol. 56, No. 3, 2008, pp. 619-631.

Chandler, M.Q., Bammann, D.J., Horstemeyer, M.F., "A continuum model for hydrogen assisted void nucleation in ductile materials," *Modelling and Simulation in Materials Science and Engineering*, Vol. 21, No. 5, 2013, 055028.

Chandrasekhar, S., "Stochastic Problems in Physics and Astronomy," *Reviews of Modern Physics*, Vol. 15, No. 1, 1943, pp. 2-89.

Chen, S., Chen, K., Peng, K., Chen, X., Ceng, Q., "Effect of Heat Treatment on Hot Deformation Behavior and Microstructure Evolution of 7085 Aluminum Alloy," *Journal of Alloys and Compounds*, Vol. 537, 2012A, pp. 338-345.

Chen, S.Y., Chen, K.H., Peng, G.S., Liang, X., Chen, X.H., "Effect of Quenching Rate on Microstructure and Stress Corrosion Cracking of 7085 Aluminum Alloy," *Transactions of Nonferrous Metals Society of China*, Vol. 22, No. 1, 2012B, pp. 47-52.

- Chen, S.Y., Chen, K.H., Peng, G.S., Le, J.I.A., “Effect of Initial Microstructure on Hot Workability of 7085 Aluminum Alloy,” *Transactions of Nonferrous Metals Society of China*, Vol. 23, No. 4, 2013A, pp. 956-963.
- Chen, S.Y., Chen, K.H., Le, J.I.A., Peng, G.S., “Effect of Hot Deformation Conditions on Grain Structure and Properties of 7085 Aluminum Alloy,” *Transactions of Nonferrous Metals Society of China*, Vol. 23, No. 2, 2013B, pp. 329-334.
- Chichili, D.R., Ramesh K.T., “Recovery experiments for adiabatic shear localization: A novel experimental technique,” *Transactions-American Society of Mechanical Engineers Journal of Applied Mechanics*, Vol. 66, 1999, pp. 10-20.
- Chichili, D.R., Ramesh, K.T., Hemker, K.J., “Adiabatic shear localization in alpha-titanium: experiments, modeling, and microstructural evolution,” *Journal of the Mechanics and Physics of Solids*, Vol. 52, No. 7, 2004, pp. 1889-1909.
- Cho, H., Horstemeyer, M.F., Hammi, Y., Francis, D.K., “Finite Element Model for Plymouth Tube Processing using Internal State Variables,” *Proceedings of the 3rd World Congress on Integrated Computational Materials Engineering, ICME 2015*, John Wiley & Sons, Inc., 2015.
- Cho, H.E., Hammi, Y., Francis, D.K., Stone, T., Mao, Y., Sullivan, K., Wilbanks, J., Zelinka, R. and Horstemeyer, M.F., 2018. “Microstructure-Sensitive, History-Dependent Internal State Variable Plasticity-Damage Model for a Sequential Tubing Process,” *Integrated Computational Materials Engineering (ICME) for Metals: Concepts and Case Studies*, p.199.
- Clifton, R.J., Duffy, J., Hartley, K.A., Shawki, T.G., “On Critical Conditions for Shear Band Formation At High Strain Rates,” *Scripta Metallurgica*, Vol. 18, 1984, pp. 443-448.
- Cocks, A.C.F., Ashby, M.F., “Creep Fracture By Void Growth,” *Progress in Materials Science*, Vol. 27, Pergamon Press, 1982, pp. 189-244.
- Coleman B.D., Gurtin, M.E., “Thermodynamics with Internal State Variables,” *The Journal of Chemical Physics*, Vol. 47, No. 2, 1967, pp. 597-613.
- Coleman, H.W., Steele, W. G, *Experimentation, Validation, and Uncertainty Analysis for Engineers*, John Wiley & Sons, 2009.
- Conrad, H., Feuerstein, S., Rice, L., “Effects of grain size on the dislocation density and flow stress of niobium,” *Materials Science and Engineering*, Vol. 2, No. 3, 1967, pp. 157-168.

Conrad, H., "Work-hardening model for the effect of grain size on the flow stress of metals," *Ultrafine-Grain Metals*, 1970.

Corbett, G.G., Reid, S.R., Johnson, W., "Impact Loading of Plates and Shells by Free-Flying Projectiles: A Review," *International Journal of Impact Engineering*, Vol. 18, No. 2, 1996, pp. 141-230.

Cottrell, A.H., "Theoretical aspects of fracture," *Fracture*, Ed. Averbach, B.L., Felbeck, D.R., Hahn, G.T., and Thomas, D.A., 20; 1959, New York, The Technological Press of MIT and John Wiley and Sons, Inc.

Cowie, J.G., Azrin, M., Olson, G.B., "Microvoid formation during shear deformation of ultrahigh strength steels," *Metallurgical transactions A*, Vol. 20, No. 1, 1989, pp. 143-153.

Crapps, J., Marin, EB, Horstemeyer, MF, Yassar, R, and Wang, PT, "Internal State Variable Plasticity-Damage Modeling of Copper Tee-Shaped Tube Hydroforming Process," *J. Matls. Proc. Tech*, ASME, 1726-1737, 2010. DOI: <https://doi.org/10.1016/j.jmatprotec.2010.06.003>

Curran, D.R., Seaman, L., Shockey, D.A., "Dynamic Failure in Solids," *Physics Today*, Vol. 30, No. 1, 1977, pp. 46-55.

Curran, D.R., Seaman, L., Shockey, D.A., "Dynamic Failure of Solids," *Physics Reports*, Vol. 147, No. 5-6, 1987, pp. 253-388.

Da Silva, M.G., Ramesh, K.T., "The rate-dependent deformation and localization of fully dense and porous Ti-6Al-4V," *Material Science and Engineering A*, Vol. 232, No. 1-2, 1997, pp. 11-22.

Dassault Systems Simulia Corp., *ABAQUS Theory and User's Manual: Version 6.14*, Providence, RI., 2014.

Davies, E.D.H., Hunter, S.C., "The Dynamic Compression Testing of Solids By The Method of The Split Hopkinson Pressure Bar," *Journal of the Mechanics and Physics of Solids*, Vol. 11, 1963, pp. 155-179.

de Koning, A.E., *A contribution to the analysis of slow crack growth*, Rep. NLR MP 75035 U, National Aerospace Laboratory (NLR), The Netherlands, 1975.

Deltort, B., "Experimental and Numerical Aspects of Adiabatic Shear in a 4340 Steel," *Le Journal de Physique IV*, Vol. 4, No. C8, 1994, C8-447.

Department of the Army, Ordnance Corps, *Investigation of Solidification of High Strength Steel Castings Under Simulated Production Conditions*, Rodman Laboratory, Watertown Arsenal, 1959.

Dey, S., Børvik, T., Hopperstad, O.S., Leinum, J.R., Langseth, M., “The effect of target strength on the perforation of steel plates using three different projectile nose shapes,” *International Journal of Impact Engineering*, Vol. 30, No. 8-9, 2004, pp. 1005-1038.

Dieter, G.E., *Mechanical Metallurgy*, 2nd ed., McGraw-Hill, 1976, p. 682.

Dighe, M.D., Gokhale, A.M., and Horstemeyer, M. F., “Effect of Temperature on Silicon Particle Damage in Cast Microstructure of A356 Alloy,” *Metallurgical and Materials Transactions*, 1997, Vol 29a, pp. 905-908, 1998. DOI: <https://doi.org/10.1007/s11661-002-0117-2>

Dikshit, S.N., Kutumbarao, V.V., Sundararajan, G., “The influence of plate hardness on the ballistic penetration of thick steel plates,” *International Journal of Impact Engineering*, Vol. 16, No. 2, 1995, pp. 293-320.

Doherty, R.D., Hughes, D.A., Humphreys, F.J., Jonas, J.J., Jensen, D.J., Kassner, M.E., King, W.E., McNelly, T.R, McQueen, H.J., Rollet, A.D., “Current issues in recrystallization: a review,” *Materials Science and Engineering: A* 238, No. 2, 1997, pp. 219-274.

Dong, M.J., Prioul, C., Francois, D., “Damage effect on the fracture toughness of nodular cast iron: part 1. Damage characterization and plastic flow stress modeling,” *Metallurgical and Materials Transactions A*, Vol. 28 No. 11, 1997, pp. 2245-2254.

Doude, H., Oglesby, D., Gullett, P.M., El Kadiri, H., Jelinek, B., Baskes, M.I., Oppedal, A., Hammi, Y., Horstemeyer, M.F., “Cast Magnesium Alloy Corvette Cradel,” *Integrated Computational Materials Engineering (ICME) for Metals: Concepts and Case Studies*, John Wiley & Sons, Inc., Hoboken, NJ, USA, 2018, p. 337-376.

Drucker, D.D., “A More Fundamental Approach to Plastic Stress-Strain Relations,” *Journal of Applied Mechanics-Transactions of the ASME*, Vol. 18, No. 3, 345 E 47th St., New York, NY10017: ASME-AMER SOC MECHANICAL ENG, 1951.

Drucker, D.D., *A Definition of Stable Inelastic Material*, No. TR-2, Brown University, Providence, RI, 1957.

Duan, Z.Q., Li, S.X., Huang, D.W., “Microstructures and Adiabatic Shear Bands Formed by Ballistic Impact in Steels and Tungsten Alloy,” *Fatigue & Fracture of Engineering Materials & Structures*, Vol. 26, No. 12, 2003, pp. 1119-1126.

Duhem, P.M.M., *Traité de Energétique ou de thermodynamique générales*, 1. Guathey-Villary, 1911.

Dunand, M., Mohr, D., "On the predictive capabilities of the shear modified Gurson and the modified Mohr-Coulomb fracture models over a wide range of stress triaxialities and Lode angles," *Journal of the Mechanics and Physics of Solids*, Vol. 59, 2011, pp. 1374-1394.

Eringen, A.C., "Linear Theory of Nonlocal Elasticity and Dispersion of Plane Waves," *International Journal of Engineering Science*, Vol. 10, 1972, pp. 425-435.

Eringen, A.C., "Stress Concentration at The Tip Of Crack," *Mechanics Research Communications*, Vol. 1, No. 4, 1974, pp. 233-237.

Eringen, A.C., Speziale, C.G., Kim, B.S., "Crack-Tip Problem in Non-Local Elasticity," *Journal of the Mechanics and Physics of Solids*, Vol. 25, 1977, pp. 339-355.

Evans, A.G., Gulden, M.E., Rosenblatt, M., "Impact Damage in Brittle Materials in the Elastic-Plastic Response Regime," *Proceedings of the Royal Society of London A: Mathematical, Physical, and Engineering Sciences*, Vol. 361, No. 1706, The Royal Society, 1978, pp. 343-365.

Fang, H., Rais-Rohani, M., Liu, Z., Horstemeyer, M.F., "A comparative study of metamodeling methods for multiobjective crashworthiness optimization," *Computers & Structures*, Vol. 83, no. 25-26, 2005, pp. 2121-2136.

Fang, H., Solanki, K., Horstemeyer, M.F., "Numerical simulations of multiple vehicle crashes and multidisciplinary crashworthiness optimization," *International Journal of Crashworthiness*, Vol. 10 (2), 2005, pp. 161-171. DOI: <https://doi.org/10.1533/ijcr.2005.0335>

Fernando, U.S., Brown, M.W., Miller, K.J., "Low Cycle Fatigue Behavior of 1% CrMrV Steel Using a New Multiaxial Test Facility, Vol. 3, *Fracture Behavior and Design of Materials and Structures*, Eng. Materials Advisory Services, Ltd. U.K., 1990, pp. 1753-1758.

Ferreira, P.J., Robertson, I.M., Birnbaum, H.K., "Hydrogen effects on the character of dislocations in high-purity aluminum," *Acta Materialia*, Vol. 47, No. 10, 1999, pp. 2991-2998.

Fleck, N.A., Hutchinson, J.W., "A Phenomenological Theory for Strain Gradient Effects in Plasticity," *Journal of the Mechanics and Physics of Solids*, Vol. 41, No. 12, 1993, pp. 1825-1857.

Fowles, R., Williams, R.F., "Plane Stress Wave Propagation in Solids," *Journal of Applied Physics*, Vol. 41, No. 1, 1970, pp. 360-363

- Francis, D.K., Bouvard, J.L., Hammi, Y., Horstemeyer, M.F., "Formulation of a Damage Internal State Variable Model for Amorphous Glassy Polymers," *International Journal of Solids and Structures*, Vol. 51, No. 15, 2014, pp. 2765-2776.
- Fugelso, L.E., Bloedow, F.H., *Studies in the Perforation of Thin Metallic Plates by Projectile Impact: 1. Normal Impact of Circular Cylinders*. No. MR-1250, General American Transportation Corp Niles IL MRD Div, 1966.
- Gangulee, A., Gurland, J., "On the Fracture of Silicon Particles in Aluminum-Silicon Alloys," *AIME MET SOC TRANS* 239, No. 2, 1967, pp. 269-272.
- Garboczi, E.J., Snyder, K.A., Douglas, J.F., "Geometrical Percolation Threshold of Overlapping Ellipsoids," *Physical Review E*, Vol. 51, No. 1, 1995, pp. 819-828. DOI: <https://doi.org/10.1103/PhysRevE.52.819>
- Giglio, M., Manes, A., Vigano, F., "Ductile fracture locus of Ti-6Al-4V titanium alloy," *International Journal of Mechanical Sciences*, Vol. 54, 2012, pp. 121-135.
- Gilat, A., "Torsional Kolsky Bar Testing," *ASM Handbook*, Vol 8, Eds. Khun, H.K., Medlin, D., ASM International, Materials Park, Ohio, 2000, pp. 505-518.
- Glen, L.A., Chudnovsky, A., "Strain-Energy Effects on Dynamic Fragmentation," *Journal of Applied Physics*, Vol. 59, No. 4, 1986, pp. 1379-1380.
- Goldsmith, W., Lui, T.W., Chulay, S., "Plate Impact and Perforation by Projectiles," *Experimental Mechanics*, Vol. 5, No. 12, 1965, pp. 385-404.
- Goldsmith, W., Finnegan, S.A., Rinehart, K.I., *High-Velocity Impact of Steel Spheres of Metallic Targets*, No. NWC-TP-5110. Naval Weapons Center China Lake CA, 1971.
- Goldsmith, W., Finnegan, S.A., "Normal and Oblique Impact of Cylindro-Conical and Cylindrical Projectiles on Metallic Plates," *International Journal of Impact Engineering*, Vol. 4, No. 2, 1986, pp. 83-105.
- Goods, S.H., Brown, L.M., "The nucleation of cavities by plastic deformation," *Acta Metallurgica*, Vol. 27, 1979, pp. 1-15. DOI: <https://doi.org/10.1016/B978-0-08-030541-7.50007-2>
- Grady, D.E., "Local Inertial Effects in Dynamic Fragmentation," *Journal of Applied Physics*, Vol. 53, No. 1, 1982, pp. 322-325.
- Grady, D.E., Kipp, M.E., "Geometric Statistics and Dynamic Fragmentation," *Journal of Applied Physics*, Vol. 58, No. 3, 1985, pp. 1210-1222.
- Grady, D.E., "The Spall Strength of Condensed Matter," *Journal of the Mechanics and Physics of Solids*, Vol. 36, No. 3, 1988, pp. 353-384.

Gray, G.T., Chen, S.R., Wright, W., Lopez, M.F., "Constitutive Equations for Annealed Metals Under Compression at High Strain Rates and High Temperatures," Los Alamos National Laboratory, Los Alamos, 1994.

Green, A.E., Naghdi, P.M., "A General Theory of An Elastic-Plastic Continuum," *Archive for Rational Mechanics and Analysis*, Vol. 18, No. 4, 1965, pp. 251-281.

Griffith, A.A., "The Phenomena of Rupture and Flow in Solids," *Philosophical Transactions of The Royal Society of London, Series A, Containing Papers of a Mathematical or Physical Character*, Vol. 221, 1921, pp. 163-198.

Grüneisen, E., "Theorie des Festen Zustandes Einatomiger Elemente," *Annalen der Physik*, Vol. 344, No. 12, 1912, pp. 257-306.

Guduru, P.R., Rosakis, A.J., Ravichandran, G., "Dynamic Shear Bands: An Investigation Using High Speed Optical and Infrared Diagnostics," *Mechanics of Materials*, Vol. 33, No. 6, 2001, pp. 371-402.

Guo, Y.B., Wen, Q., Horstemeyer, M.F., "An Internal State Variable Plasticity-Based Approach to Determine Dynamic Loading History Effects on Material Property in Manufacturing Processes," *Int. J. Mechanical Sciences*, vol. 47, pp. 1423-1441, 2005. DOI: <https://doi.org/10.1016/j.ijmecsci.2005.04.015>

Gupta, N.K., Madhu, V., "An Experimental Study of Normal and Oblique Impact of Hard-Core Projectile on Single and Layered Plates," *International Journal of Impact Engineering*, Vol. 19, No. 5, 1997, pp. 395-414.

Gurland, J., "Observations on the fracture of cementite particles in a spheroidized 1.05% C steel deformed at room temperature," *Acta Metallurgica*, Vol. 20, No. 5, 1972, pp. 735-741.

Gurson, A.L., "Continuum Theory of Ductile Rupture by Void Nucleation and Growth: Part 1- Yield Criteria and Flow Rules for Porous Ductile Media," *Journal of Engineering Materials and Technology*, Vol. 99, No. 1, 1977, pp. 2-15.

Hall, E.O., "The deformation and ageing of mild steel: III discussion of results," *Proceedings, of the Physical Society, Section B*, Vol. 64, No. 9, 1951, pp. 747.

Hancock, J.W., Mackenzie, A.C., "On the mechanisms of ductile failure in high-strength steels subjected to multi-axial stress-states," *Journal of the Mechanics and Physics of Solids*, Vol. 24, No. 2-3, 1976, pp. 147-160.

Hardin, R.A., Backerman, C., "Effect of porosity on the stiffness of cast steel," *Metallurgical and Materials Transactions A*, Vol. 38, No. 12, 2007, pp. 2992-3006.

He, L., Li, X., Zhu, P., Cao, Y., Cui, J., "Effects of High Magnetic Field on the Evolutions of Constituent Phases in 7085 Aluminum Alloy During Homogenization," *Materials Characterization*, Vol. 71, 2012, pp. 19-23.

Hertz, H., *Miscellaneous Papers*, Macmillan, 1896.

Hill, R., "Acceleration Waves in Solids," *Journal of the Mechanics and Physics of Solids*, Vol. 10, 1969, pp. 1-16.

Holzappel, G.A., *Nonlinear Solid Mechanics: A Continuum Approach for Engineering*, Wiley 2000.

Hopkinson, B., "A Method of Measuring the Pressure Produced in the Detonation of High Explosives or the Impact of Bullets," *Philosophical Transactions of the Royal Society of London, Series A, Containing Papers of a Mathematical or Physical Character*, Vol. 213, 1914, pp. 437-456.

Horn, R.M., Ritchie, R.O., "Mechanisms of Tempered Martensite Embrittlement in Low Alloy Steels," *Metallurgical Transactions A*, Vol. 9, 1978, pp. 1039-1053.

Horstemeyer, M.F., Gokhale, A.M., "A Void-Crack Nucleation Model for Ductile Metals," *International Journal of Solids and Structures*, Vol. 36, 1999, pp. 5029-5055.

Horstemeyer, M.F., Lathrop, J., Gokhale, A.M., Dighe, M.D., "Modeling Stress State Dependent Damage Evolution in a Cast Al-Si-MG Aluminum Alloy," *Theoretical and Applied Fracture Mechanics*, Vol. 31, No. 1, 2000A, pp. 31-47.

Horstemeyer, M.F., Matalanis, M., Sieber, A.M., Botos, M.L., "Micromechanical Finite Element Calculations of Temperature and Void Configuration Effects on Void Growth and Coalescence," *International Journal of Plasticity*, Vol. 16, No. 7, 2000B, pp. 979-1015.

Horstemeyer, M.F., Ramaswamy, S., "On Factors Affecting Localization and Void Growth in Ductile Metals: a Parametric Study," *International Journal of Damage Mechanics*, Vol. 9, No. 1, 2000, pp. 5-28.

Horstemeyer, M.F., "A Numerical Parametric Investigation of Localization and Forming Limits," *International Journal of Damage Mechanics*, Vol. 9, No. 3, 2000, pp. 255-285.

Horstemeyer, M.F., "From Atoms to Autos – A New Design Paradigm Using Microstructure Property Modeling Part 1: Monotonic Loading Conditions," 2001, available <http://www.osti.gov/servlets/purl/791300-CSIVA5/native/>

Horstemeyer, M.F., Negrete, M., and Ramaswamy, S., "Using a Micromechanical Finite Element Parametric Study to Motivate a Phenomenological Macroscale Model

for Void/Crack Nucleation in Aluminum with a Hard Second Phase," *Mechanics of Materials*, Vol. 35, pp. 675-687, 2003A. DOI: [https://doi.org/10.1016/S0167-6636\(02\)00165-5](https://doi.org/10.1016/S0167-6636(02)00165-5)

Horstemeyer, M.F., Gall, K.D., Dolan K.W., Waters, A., Haskins, J.J., Perkins, D.E., Gokhale, A.M., Dighe, M.D., "Numerical, Experimental, Nondestructive, and Image Analysis of Damage Progression in Cast A356 Aluminum Notch Tensile Bars," *Theoretical and Applied Fracture Mechanics*, Vol. 39, No. 1, 2003B, pp. 23-45.

Horstemeyer, M.F.; X. C. Ren; H. Fang; E. Acar; P. T. Wang, "A comparative study of design optimization methodologies for side-impact crashworthiness, using injury-based versus energy-based criterion," *International Journal of Crashworthiness*, 1754-2111, Volume 14, Issue 2, Pages 125 – 138, 2009. DOI: <https://doi.org/10.1080/13588260802539489>

Horstemeyer, M.F., "Case Study: From Atoms to Autos: A Redesign of a Cadillac Control Arm," *Integrated Computational Materials Engineering (ICME) for Metals: Using Multiscale Modeling to Invigorate Engineering Design with Science*, John Wiley & Sons, Inc., Hoboken, NJ, USA, 2012, p. 187-339.

Horstemeyer, M.R., Chaudhuri, S., "A Systematic Multiscale Modeling and Experimental Approach to Protect Grain Boundaries in Magnesium Alloys from Corrosion," Mississippi State University, Mississippi State, MS, 2015.

Hou, X., Goldsmith, W., "Projectile perforation of moving plates: Experimental Investigation," *International Journal of Impact Engineering*, Vol. 18, No. 7-8, 1996, pp. 859-875.

Hsiao, H.M., Daniel, I.M., Cordes, R.D., "Dynamic Compressive Behavior of Thick Composite Materials," *Experimental Mechanics*, Vol. 38, No. 3, 1998, pp. 172-180.

Hu, H., Speich, G.R., Miller, R.L., *Effect of Crystallographic Texture, Retained Austenite, and Austenite Grain Size on the Mechanical and Ballistic Properties of Steel Armor Plates*, No. 76-H-018. United States Steel Corp Monroeville PA Research Lab, 1976.

Hu, C.J., Lee, P.Y., Chen, J.S., "Ballistic Performance and Microstructure of Modified Rolled Homogeneous Armor Steel," *Journal of the Chinese Institute of Engineers*, Vol. 25, No. 1, 2002, pp. 99-107.

Huang, Y., et al, "Analytic and numerical studies on mode I and Mode II fracture in elastic-plastic materials with strain gradient effects," *International Journal of Fracture*, Vol. 100, No. 1 1999, pp. 1-27.

Hugoniot, H., "Memoir on the Propagation of Movements in Bodies Especially Perfect Gases (First Part), *J. de l'Ecole Polytechnique*, Vol. 57, 1887, pp. 3-97.

- Hutchinson, J.W., Tvergaard, V., "Shear Band Formation in Plane Strain," *Int. J. Solids Structures*, Vol. 17, No. 5, 1981, pp. 451-470.
- Hutchinson, J.W., Neale K.W., "Neck Propagation," *J. Mech. Phys. Solids*, Vol. 31, No. 5, 1983, pp. 405-426.
- Hutchinson, J.W., "Mixed Mode Fracture Mechanics of Interfaces," *Metal-Ceramic Interfaces, Acta-Scripta Metallurgica Proceedings Series*, Vol. 4, 1990, pp. 295-306.
- Ipson, T.W., "Ballistic Perforation Dynamics," *Journal of Applied Mechanics*, Vol. 30, 1963, pp. 384-390.
- Irwin, G.R., "Fracture Dynamics," *Fracturing of Metals*, 152, 1948.
- Irwin, G.R., "Analysis of Stresses and Strains Near the End of a Crack Traversing a Plate," *Journal of Applied Mechanics*, 1957.
- Jabra, J., et al. "The Effect of Thermal Exposure on the Mechanical Properties of 2999-T6 Die Forgings, 2099-T83 Extrusions, 7075-T7651 Plate, 7085-T7452 Die Forgings, 7085-T7651 Plate, and 2397-T87 Plate Aluminum Alloys," *Journal of Engineering Materials and Performance*, Vol. 15, No. 5, 2006, pp. 601-607.
- Johnson, J.N., "Dynamic Fracture and Spallation in Ductile Solids," *Journal of Applied Physics*, Vol. 52, No. 4, 1981, pp. 2812-2825.
- Johnson, G.R., Cook, W.H., "A Constitutive Model and Data for Metals Subjected to Large Strains, High Strain Rates and High Temperatures," *Proceedings of the 7th International Symposium on Ballistics*, Vol. 21, No. 1983, 1983, pp. 541-547.
- Johnson, G.R., Cook, W.H., "Fracture characteristics of three metals subjected to various strains, strain rates, temperatures, and pressures," *Engineering fracture mechanics*, Vol. 21, No. 1, 1985, pp. 31-48.
- Johnson, G.R., Stryk, R.A., *User Instructions for the EPIC-3 Code*, Honeywell INC Defense Systems Div, Brooklyn Park, MN, 1987.
- Johnson, G.R., Holmquist, T.J., "Evaluation of cylinder-impact test data for constitutive model constants," *Journal of Applied Physics*, Vol. 64, No. 8, 1988, pp. 3901-3910.
- Jordon, J.B., Horstmeyer, M.F., Solanki, K., Xue, Y., "Damage and Stress State Influence on the Buaschinger Effect in Aluminum Alloys," *Mechanics of Materials*, Vol. 39, No. 10, 2007, pp. 920-931.
- Jordon, J.B., Horstemeyer, M.F., Solanki, K., Bernard, J.D., Berry, J.T., Williams, T.N., "Damage Characterization and Modeling of a 7075-T651 Aluminum Plate,"

Materials Science and Engineering: A, Vol. 527, No. 1-2, 2009, pp. 169-178. DOI: <https://doi.org/10.1016/j.msea.2009.07.049>

Kachanov, L.M., "Rupture Time Under Creep Conditions," *Izvestia Akademii Nauk SSSR, Otdelenie Tekhnicheskikh Nauk* 8, pp. 21-31.

Kanninen, M.F., Rybicki, E.F., Stonesifer, R.B., Broek, D., Rosenfield, A.R., Marschall, C.W., and Hahn, G.T., "Elastic-Plastic Fracture Mechanics for Two-Dimensional Stable Crack Growth and Instability Problems," *Elastic-Plastic Fracture, ASTM STP 668*, J.D. Landes, J.A. Begley, and G.A. Clarke, Eds., American Society for Testing and Materials, 1979, pp. 121-150.

Karabin, M.E., Barlat, F., Shuey, R.T., "Finite Element Modeling of Plane Strain Toughness for 7085 Aluminum Alloy," *Metallurgical and Materials Transactions A*, Vol. 40, No. 2, 2009, pp. 354-364.

Kestin, J., Rice, J.R., "Paradoxes in the Application of Thermodynamics to Strained Solids," Division of Engineering, Brown University, 1969.

Kim, K.S., Chen, X., Han, C., Lee, H.W., "Estimation methods for fatigue properties of steels under axial and torsional loading," *International Journal of Fatigue*, Vol. 24, No. 7, 2002, pp. 783-793.

Koller, M.G., Kolsky, H., "Waves Produced by the Elastic Impact of Spheres on Thick Plates," *International Journal of Solids Structures*, Vol. 23, No. 10, 1987, pp. 1387-1400.

Kolsky, H., "An Investigation of the Mechanical Properties of Materials at very High Rates of Loading," *Proceedings of the Physical Society, Section B*, Vol. 62, No. 11, 1949, p 676.

Kuhn, H.A., "Shear, Torsion, and Multiaxial Testing," *ASM Handbook*, Vol. 8, Eds. Khun, H.K., Medlin, D., ASM International, Materials Park, Ohio, 2000, pp. 185-194.

Lasry, D., Belytschko, T., "Localization Limiters in Transient Problems," *International Journal of Solids and Structures*, Vol. 24, No. 6, 1988, pp. 581-597.

Lee, Y., Gangloff, R.P., "Measurement and modeling of hydrogen environment-assisted cracking of ultra-high-strength steel," *Metallurgical and Materials Transactions A*, Vol. 38, No. 13, 2007, pp. 2174-2190.

Levy, "Memoire sur les equations generatees des mouvements intérieurs des corps solides ductiles au delà des limites ou l'élasticité pourrait les ramener a leur premier état," *CR Acad. Sci. Paris*, Vol. 70, 1870, pp. 1323-1325.

Levy, N., Goldsmith, W., "Normal Impact and Perforation of Thin Plates by Hemispherically-Tipped Projectiles – II. Experimental Results." *International Journal of Impact Engineering*, Vol. 2, No. 4, 1984, pp. 299-324.

Lee, E. H., Liu, D. T., "Finite Strain Elastic-plastic Theory with Application to Plane-Wave Analysis," *J. Appl. Physics*, Vol. 38, 1967, pp. 391-408.

Li, Y., Bushby, A.J., Dunstan, D.J., "The Hall-Petch effect as a manifestation of the general grain size effect," *Proc. R. Soc. A*, Vol. 472, No. 2190, 2016, p. 20150890.

Lindholm, U.S., Yeakley, L.M., "A Dynamic Biaxial Testing Machine," *Experimental Mechanics*, Vol. 7, No. 1, 1967, pp. 1-7. DOI: <https://doi.org/10.1007/BF02326833>

Lindley, T.C., Oates, G., Richards, C.E., "A critical of carbide cracking mechanisms in ferrite/carbide aggregates," *Acta metallurgica*, Vol. 18, No. 11, 1970, pp. 1127-1136.

Livermore Software Technology Corporation, LS-Dyna Keyword User's Manual: Volume 1, Livermore, CA, 2007.

Littlefield, D.L., Anderson, C.E., Partom, Y., Bless, S.J., "The penetration of steel targets finite in radial extent," *International Journal of Impact Engineering*, Vol. 19, No. 1, 1997, pp. 49-62.

Lopes, A.B., Barlat, F., Gracio, J.J., Ferreira Duarte, J.F., Rauch, E.F., "Effect of Texture and Microstructure on Strain Hardening Anisotropy for Aluminum Deformed in Uniaxial Tension and Simple Shear," *International Journal of Plasticity*, Vol. 19, No. 1, 2003, pp. 1-22. DOI: [https://doi.org/10.1016/S0749-6419\(01\)00016-X](https://doi.org/10.1016/S0749-6419(01)00016-X)

Lugo, M., Tschopp, M.A., Jordon, J.B., Horstemeyer, M.F., "Microstructure and damage evolution during tensile loading in a wrought magnesium alloy," *Scripta Materialia*, v 64, n 9, p 912-915, 2011. DOI: <https://doi.org/10.1016/j.scriptamat.2011.01.029>

Lugo, M., Whittington, W., Hammi, Y., Bouvard, C., Li, B., Francis, D.K., Wang, P.T. and Horstemeyer, M.F., "Using an Internal State Variable (ISV)–Multistage Fatigue (MSF) Sequential Analysis for the Design of a Cast AZ91 Magnesium Alloy Front-End Automotive Component," *Integrated Computational Materials Engineering (ICME) for Metals: Concepts and Case Studies*, 2018, p.377.

Luong, H., Hill, M.R., "The Effects of Laser Peening on High-Cycle Fatigue in 7085-T7651 Aluminum Alloy," *Materials Science and Engineering: A*, Vol. 477, No. 1, 2008, pp. 208-216.

Magness, L.S., "High Strain Rate Deformation Behaviors of Kinetic Energy Penetrator Materials During Ballistic Impact," *Mechanics of Materials*, Vol. 17, No. 2-3, 1994, pp. 147-154.

Manganello, S.J., Carter, G.C., *Development of Heat-Treated Composite Steel Armor*, United States Steel Corp, Monroeville, PA, Applied Research Lab, 1967.

- Marchand, A., Duffy, J., "An experimental study of the formation process of adiabatic shear bands in a structural steel," *Journal of the Mechanics and Physics of Solids*, Vol. 36, No. 3, 1988, pp. 251-283.
- Marin, E.B., McDowell, D.L., "Associative Versus Non-Associative Porous Viscoplasticity Based on Internal State Variable Concepts," *International Journal of Plasticity*, Vol. 12, No. 5, 1996, pp. 629-669.
- McClintock, F.A., "A Criterion for Ductile Fracture by the Growth of Holes," *Journal of Applied Mechanics*, 1968, pp. 363-371.
- McMeeking, R.M., "Finite deformation analysis of crack-tip opening in elastic-plastic materials and implications for fracture," *Journal of the Mechanics and Physics of Solids*, Vol. 25, No. 5, 1977, pp. 357-381.
- Mead, D.J., "Wave Propagation in Continuous Periodic Structures: Research Contributions from Southampton, 1964-1995," *Journal of Sound and Vibration*, Vol. 190, No. 3, 1996, pp. 495-524.
- Meakin, J.D., Petch, N.J., "Strain-hardening of polycrystals: The α -brasses," *Philosophical Magazine*, Vol. 29, No. 5, 1974, pp. 1149-1156.
- Mear, M.E., Hutchinson, J.W., "Influence of Yield Surface Curvature on Flow Localization in Dilatant Plasticity," *Mechanics of Materials 4*, 1985, pp. 395-407.
- Mescall, J.F., Rogers, H., *Role of Shear Instability in Ballistic Penetration*, No. MTL-TR-89-104. Army Lab Command Watertown MA Material Technology Lab, 1989.
- Meyers, M.A., Aimone, C.T., "Dynamic Fracture (Spalling) of Metals," *Progress in Materials Science*, 28.1, 1983, pp. 1-96.
- Meyers, M.A., Subhash, G., Kad, B.K., Prasad, L., "Evolution of Microstructure and Shear-Band Formation in α -hcp Titanium," *Mechanics of Materials*, Vol. 17, 1994, pp. 175-193
- Meyers, M.A., Andrade, U.R., Chokshi, A.H., "The effect of grain size on the high-strain, high-strain-rate behavior of copper," *Metallurgical and Materials Transactions A*, Vol. 26, No. 11, 1995, pp. 2881-2893.
- Mises, R. V., "Mechanik der festen Körper im plastisch-deformablen Zustand," *Nachrichten von der Gesellschaft der Wissenschaften zu Göttingen, Mathematisch-Physikalische Klasse*, 1913, pp. 582-592.
- Mises, R. V., "Mechanik der Plastischen Formänderung von Kristallen," *ZAMM-Zeitschrift für Angewandte Mathematik und Mechanik*, Vol. 8, No. 3, 1928, pp. 161-185.

- Moss, G.L., Seaman, L., *Fracture of Rolled Homogeneous Steel Armor (Nucleation Threshold Stress)*, No. ARBRL-MR-02984, Army Ballistic Research Lab Aberdeen Proving Ground MD, 1980.
- Mukai, S., Takada, T., Sakane, M., Ohnami, M., Tsurui, T., “Development of Multiaxial Creep Testing Machine Using Cruciform Specimen,” *Journal of the Society of Materials Science, Japan (Japan)*, Vol. 45, No. 5, 1996, pp. 559-565.
- Narutani, T., Takamura, J., “Grain-size strengthening in terms of dislocation density measured by resistivity,” *Acta metallurgica et materialia*, Vol. 39, No. 8, 1991, pp. 2037-2049.
- Nashon, K., Hutchinson, J.W., “Modification of the Gurson Model for Shear Failure,” *European Journal of Mechanics A/Solids*, vol. 27, 2008, pp. 1-17.
- Needleman, A., Rice, J.R., “Limits to Ductility Set By Plastic Flow Localization,” *Mechanics of Sheet Metal Forming*, Plenum Publishing Corporation, 1978, pp. 237 – 267.
- Needleman, A., Tvergaard, V., “An Analysis of Ductile Rupture in Notched Bars,” *Journal of the Mechanics and Physics of Solids*, Vol. 32, No. 6, 1984A, pp. 461-490.
- Needleman, A., “A Continuum Model for Void Nucleation by Inclusion Debonding,” *Journal of Applied Mechanics*, Vol. 54, No. 3, 1987, pp. 525-531.
- Nemat-Nasser, S., Chung, D.T., “Phenomenological Modelling of Rate-Dependent Plasticity for High Strain Rate Problems,” *Mechanics of Materials*, Vol. 7, 1989, 319-344.
- Newman, J.C., Jr. “An Elastic-Plastic Finite Element Analysis of Crack Initiation, Stable Crack Growth, and Instability,” *Fracture Mechanics: Fifteenth Symposium*. ASTM International, 1984.
- Park, K., Paulino, G.H., Roesler, J.R., “A unified potential-based cohesive model of mixed-mode fracture,” *Journal of the Mechanics of Physics and Solids*, Vol. 57, No. 6, 2009, pp. 891-908.
- Petch, N.J., “The Cleavage Strength of Polycrystals,” *J. of the Iron and Steel Institute*, Vol. 147, 1953, pp. 25-28.
- Peterson, L.A., Horstemeyer, M.F., Lacy, T.E., Moser, R.M., “An Experimentally Calibrated and Validated Internal State Variable Plasticity-Damage Model of An Aluminum 7085-T711 Alloy Under Large Deformations at Varying Strain Rates, Stress States, and Temperatures,” manuscript submitted for publication, 2019.

Phaal, R., Andrews, R.M., Garwood, S.J., "TWI Biaxial Test Program: 1984-1994." *International Journal of Pressure Vessels and Piping*, Vol. 64, No. 3, 1995, pp. 177-190.

Pijaudier-Cabot, G., Bazant, Z.P., "Nonlocal Damage Theory," *Journal of Engineering Mechanics*, Vol. 113, No. 10, 1987, pp. 1512-1533.

Prager, W., "Strain Hardening Under Combined Stresses," *Journal of Applied Physics*, Vol. 16, 1945, pp. 837.

Pifti, J., Castro, M., Squillacoti, R., Celletti, R., *Improved Rolled Homogeneous Armor (IRHA) Steel Through Higher Hardness*, No. ARL-TR-1347, Army Research Lab Aberdeen Proving Ground MD, 1997.

Puttick, K.E., "Ductile fracture in metals," *Philosophical magazine*, Vol. 4, No. 44, 1959, pp. 964-969.

Rabotnov, Y.N., "Paper 68: On the Equation of State of Creep," *Proceedings of the Institution of Mechanical Engineers, Conference Proceedings*, Vol. 178, No. 1, Sage UK: London, England: SAGE Publications, 1963.

Raman, C.V., "On Some Applications of Hertz's Theory of Impact," *Physical Review*, Vol. 15, No. 4, 1920, pp. 277-284.

Rice, J.R., "A path independent integral and the approximate analysis of strain concentration by notches and cracks," *Journal of applied mechanics*, Vol. 35, No. 2, 1968, pp. 379-386.

Rice, J.R., Tracey, D.M., "On the Ductile Enlargement of Voids in Triaxial Stress Fields," *Journal of the Mechanics and Physics of Solids*, Vol. 17, 1969, pp. 201-217

Rice, J.R., "Inelastic Constitutive Relations for Solids: an Internal-Variable Theory and its Application to Metal Plasticity," *Journal of the Mechanics and Physics of Solids*, Vol. 19, No. 6, 1971, pp. 433-455.

Rice, J.R., Paris, P., Merkle, J., "Some further results of J-integral analysis and estimates," *Progress in flaw growth and fracture toughness testing*, ASTM International, 1973.

Rice, J.R., "The Localization of Plastic Deformation," *Theoretical and Applied Mechanics*, W.T. Koiter, ed., North-Holland Publishing Company, 1976, pp. 207-220.

Rice, J.R., Sorenson, E.P., "Continuing crack-tip deformation and fracture for plane-strain crack growth in elastic-plastic solids," *Journal of the Mechanics and Physics of Solids*, Vol. 26, No. 3, 1978, pp. 163-186.

Rice, J.R., Rudnicki, J.W., "A Note on Some Features Of The Theory Of Localization Of Deformation," *Int. J. Solids Structures*, Vol. 16, No. 7, 1980, pp. 597-605.

Rittel, D., Lee, S., Ravichandran, G., "A shear-compression specimen for large strain testing," *Experimental Mechanics*, Vol. 42, No. 1, 2002, pp. 58-64.

Rudnicki, J.W., Rice, J.R., "Conditions for The Localization Of Deformation In Pressure-Sensitive Dilatant Materials," *J. Mech. Phys. Solids*, Vol. 23, No. 6, 1975, pp. 371-394.

Saint-Venant, B., "Memoire sur l'établissement des equations differentielles des mouvements intérieurs opérés dans les corps solides ductiles au dela des limites l'élasticité pourrait les ramener à leur premier état," *Comptes Rendus* 70, 1870, pp. 473-480.

Schumacher, S.C., Key, C.T., *CTH Reference Manual: Composite Capability and Technologies*, Sandia National Laboratories, Albuquerque, NM, 2009.

Semiatin, S.L., Lahoti, G.D, Jonas, J.J., "Application of Torsion Test to Determine Workability," *Mechanical Testing*, Vol. 8, *Metals Handbook*, 9th ed., ASM International, 1985, p. 154-184.

Shewchuk, J., Zamrik, S.Y., Marin, J., "Low-cycle Fatigue of 7075-T651 Aluminum Alloy in Biaxial Bending," *Experimental Mechanics*, Vol. 8, No. 11, 1968, pp. 504-512.

Shih, C.F., deLorenzi, H.G., Andrews, W.R., "Studies on crack initiation and stable crack growth," *Elastic-plastic fracture, ASTM STP 668*, J.D. Landes, J.A. Begley, and G.A. Clarke, Eds., American Society for Testing and Materials, 1979, pp. 65-120.

Shuey, R.T., Barlat, F., Karabin, M.E., Chakrabarti, D.J., "Experimental and Analytical Investigations on Plane Strain Toughness for 7085 Aluminum Alloy," *Metallurgical and Materials Transactions A*, Vol. 40, No 2, 2009, pp. 365-376.

Simulia, D.S., "Abaqus/standard theory manual, version 6.14," *Dassault Systemes Simulia Corporation, Providence, RI*, 2010.

Specification, US Military, "MIL-A-12560H (MR)-Armor Plate, Steel, Wrought, Homogeneous (For Use in Combat-Vehicles and for Ammunition Testing)," 1990.

Speich, G.R., Hu, H., Miller, R.L., *Effect of Preferred Orientation and Related Metallurgical Parameters on Mechanical Properties and Ballistic Performamce of High Hardness Steel Armor*, No. 76-H-008, United States Steel Corp Monroeville PA Research Lab, 1974.

Sreenivasan, P.R., Ray, S.K., Mannan, S.L., Rodriguez, P., "Determination of K_{Ic} At or Below NDTT Using Instrumented Drop-Weight Testing," *International Journal of Fracture*, Vol. 55, No. 3, 1992, pp. 273-283.

Stören, S., Rice, J.R., "Localized Necking In Thin Sheets," *J. Mech. Phys. Solids*, Vol. 23, No. 6, 1975, pp. 421-441.

Taguchi, G., *System of experimental design; engineering methods to optimize quality and minimize cost*, No. 04; QA279, T3. 1987.

Takaki, S., Kawasaki, K., Kimura, Y., "Mechanical properties of ultra-fine grained steels," *Journal of Materials Processing Technology*, Vol. 117, No. 3, 2001, pp. 359-363.

Taylor, B., "Formability Testing of Sheet Metals," *Forming and Forging*, Vol. 14, *Metals Handbook*, 9th ed., ASM International, 1988, p. 878-899.

Teng, X., Wierzbicki, T., "Evaluation of six fracture models in high velocity perforation," *Engineering Fracture Mechanics*, Vol. 73, 2006, pp. 1653-1678.

Teng, X., Wierzbicki, T., Couque, H., "On the transition from adiabatic shear banding to fracture," *Mechanics of Materials*, Vol. 39, 2007, pp. 107-125.

Thomson, W.T., "An Approximate Theory of Armor Penetration," *Journal of Applied Physics*, Vol 26, No. 1, 1955, pp. 80-82.

Thompson, A.W., Baskes, M.I., Flanagan, W.F., "The dependence of polycrystal work hardening on grain size," *Acta Metallurgica*, Vol. 21, No. 7, 1973, pp. 1017-1028.

Thompson, A.W., "Effect of grain size on work hardening in nickel," *Acta Metallurgica*, Vol. 25, No. 1, 1977, pp. 83-86.

Tresca, H., "Sur l'écoulement des corps solides soumis a de fortes pression," *Comptes Rendus* 59, 1864, pp. 754.

Tsai, Y.M., Kolsky, H., "A Study of the Fractures Produced in Glass Blocks by Impact," *Journal of the Mechanics and Physics of Solids*, Vol. 15, No. 4, 1967, pp. 263-278.

Tucker, M.T., Horstemeyer, M.F., Whittington, W.R., Solanki, K.N., Gullet, P.M., "The Effect of Varying Strain Rates and the Stress States on the Plasticity, Damage, and Fracture of Aluminum Alloys," *Mechanics of Materials*, Vol. 42, No. 10, pp. 895-907.

Tvergaard, V., "Ductile fracture by cavity nucleation between larger voids," *Journal of the Mechanics and Physics of Solids*, Vol. 30, No. 4, 1982A, pp. 265-286.

Tvergaard, V., "Influence of void nucleation on ductile shear fracture at a free surface," *Journal of the Mechanics and Physics of Solids*, Vol. 30, No. 6, 1982B, pp. 399-425.

Tvergaard, V., Needleman, A., "Analysis Of The Cup-Cone Fracture In A Round Tensile Bar," *Acta metall*, Vol. 32, No. 1, 1984, pp. 157-169.

U.S. Department of Defense, "Military Specification: Armor Plate, Steel, Wrought Homogeneous (for use in Comat-vehicles and for Ammunition Testing)," MIL-A-12560G(MR), U.S. Army Materials Testing Technology Laboratory, Watertown, MA, 1984.

Von Karman, T., Duwez, P., "The Propagation of Plastic Deformation in Solids," *Journal of Applied Physics*, Vol. 21, No. 10, 1950, pp. 987-994.

Walton, C.A., Horstmeyer, M.F., Martin, H.J., Francis, D.K., "Formulation of a Macroscale Corrosion Damage Internal State Variable Model," *International Journal of Solids and Structures*, Vol. 51, No. 6, 2014, pp. 1235-1245.

Waters, A.M., Martz, H.E., Dolan, K.W., Horstmeyer, M.F., and Green, R.E., "Three-Dimensional Statistical Void Analysis of AM60B Magnesium using CT Imagery," *Journal for American Society for Nondestructive Testing: Materials Evaluation*, Vol. 58, No. 10, p. 1221, 2000.

Weck, E., Leistner, E., "Metallographische Anleitung zum Farbatzen nach dem Tauchverfahren," Part III, DVS, Dusseldorf, 1986.

Weerasooriya, T., Moy, P., "Effect of Strain-Rate on the Deformation Behavior of Rolled-Homogeneous-Armor (RHA) Steel at Different Hardnesses," *Carbon*, Vol. 257, No. 284, 2004, pp. 262.

Wells, A.A., "Unstable crack propagation in metals: cleavage and fast fracture," *Proceedings of the crack propagation symposium*, Vol. 1, No. 84, 1961.

Westlake, D.G., *Generalized Model for Hydrogen Embrittlement*, Argonne National Lab, III, 1969.

Whittington, W.R., Oppedal, A.L., Turnage, S., Hammi, Y., Rhee, H., Allison, P.G., Crane, C.K., Horstmeyer, M.F., "Capturing the Effect of Temperature, Strain Rate, and Stress State on the Plasticity and Fracture of Rolled Homogeneous Armor (RHA) steel," *Materials Science and Engineering: A*, Vol. 594, 2014, pp. 82-88.

Winkel J.D., Adams, D.F., "Instrumental Drop Weight Impact Testing of Cross-ply and Fabric Composites," *Composites*, Vol. 16, No. 4, 1985, pp. 268-278.

Wood, E.R., Phillips, A., "On The Theory of Plastic Wave Propagation In A Bar," *Journal of the Mechanics and Physics of Solids*, Vol. 15, 1967, pp. 241-254.

Xia, W., Thorpe, M.F., "Percolation Properties of Random Ellipses," *Physical Review A*, Vol. 38, No. 5, 1988, pp. 2650. DOI: <https://doi.org/10.1103/PhysRevA.38.2650>

Xue, Q., Meyers, M.A., Nesterenko, V.F., "Self-organization of Shear Bands in Titanium and Ti-6Al-4V Alloy," *Acta Materialia*, Vol. 50, No. 3, 2002, pp. 575-596.

Xue, L., "Damage accumulation and fracture initiation in uncracked ductile solids subject to triaxial loading," *International Journal of Solids and Structures*, Vol. 44, 2007, pp. 5163 – 5181.

Xue, L., Wierzbicki, T., "Ductile fracture initiation and propagation modeling using damage plasticity theory," *Engineering Fracture Mechanics*, Vol. 75, 2008, pp. 3276-3293.

Xue, L., "Constitutive modeling of void shear effect in ductile fracture of porous materials," *Engineering Fracture Mechanics*, Vol. 75, 2008, pp. 3343-3366.

Yang, P.C., Norris, C.H., Stavsky, Y., "Elastic Wave Propagation in Heterogeneous Plates," *International Journal of Solids and Structures*, Vol. 2, No. 4, 1966, pp. 665-684.

Yew, C.H., Richardson Jr., H.A., "An Experimental Study of the Propagation of Torsional Plastic Waves in a Stress-Free and a Prestressed Tube," NSF Grant GK-779, National Science Foundation, 1966.

Zener, C., "The Intrinsic Inelasticity of Large Plates," *Physical Review*, Vol. 59, No. 8, 1941, pp. 669-673.

Zener, C., Hollomon, J.H., "Effect of Strain Rate upon Plastic Flow of Steel," *Journal of Applied Physics*, Vol. 15, No. 1, 1944, pp. 22-32.

Ziebs, J., Meersmann, J., Kuhn, H.J., Ledworuski, S., (1996). "Testing Materials Under Multi-Axial Loading," *International Journal of Fatigue*, Vol. 5, No. 18, 1996, pp 346.

Zbib, H.M., Aifantis, E.C., "On the Gradient-Dependent Theory of Plasticity and Shear Banding," *Acta Mechanica*, Vol. 92, No. 1-4, pp. 209-225.

Zwieg, T., "A Universal Method for the Mechanical Preparation of Alluminum Alloy Specimens with High Edge Retention and their Subsequent Colour Etching," *Danish Institute of Technology*, 2001.

APPENDIX A
ISV MODEL COEFFICIENTS FOR ALUMINUM 7085-T711 ALLOY

Table A.1 Internal State Variable (ISV) model coefficients for Aluminum 7085-T711 alloy.

Aluminum 7085-T711		Value
Elastic Constants	Shear Modulus, G (MPa)	26920
	Bulk Modulus, K (MPa)	58330
	a	0
	b	0
	Inelastic Heat Fraction	0.3336
	Melt Temperature (K)	900
ISV Plasticity Model Coefficients	C01 (MPa)	47.216
	C02 (K)	0
	C03 (MPa)	398.06
	C04 (K)	62.7368
	C05 (MPa ⁻¹)	1305.46
	C06 (K)	0
	C07 (MPa ⁻¹)	0.0145
	C08 (K)	0
	C09 (MPa)	995.87
	C10 (K)	1.256
	C11 (s·MPa ⁻¹)	0
	C12 (K)	0
	C13 (MPa ⁻¹)	4.61
	C14 (K)	564.436
	C15 (MPa)	4911.82
	C16 (K)	0
	C17 (s·MPa ⁻¹)	0
	C18 (K)	0
	C19	0.00999718
	C20 (K ⁻¹)	526.755
	C21	0
Ca	-2.0	
Cb	0.12	
ISV Model Coefficients for Void Nucleation	a	5800
	b	0
	c	285
	η_0 (#/mm ²)	1300
	KIC (MPa·mm ^{1/2})	790
	d (mm)	0.0013
	f	0.0022
	CTN (K)	-1050
	K_{void}	8.0
ISV Model Coefficients for Void Growth	McClintock Growth, n	-0.12
	R_0 (mm)	0.00055
	CTv (K ⁻¹)	-0.0013
	Initial Porosity	0.00033
ISV Model Coefficients for Pore Growth	K_{pore}	0
	Cocks-Ashby Growth, m	20
ISV Model Coefficients for Void Coalescence	NND (mm)	0.01
	d0 (mm)	0.001
	CD2	1.5
	GS0 (mm)	0.01
	GS (mm)	0.01
	Z	1.0
	ζ	3.26
	CTC (K ⁻¹)	0.0025

APPENDIX B.

INTERNAL STATE VARIABLE (ISV) MODEL COEFFICIENTS USED IN FINITE
ELEMENT SIMULATIONS OF BALLISTIC IMPACT OF STEEL ALLOYS IN
CHAPTER IV.

Table B.1 ISV Model Coefficients for 250 BHN RHA steel alloy used in *Part I*.

RHA Steel (250 BHN)	Value
Density (tonne/mm ³)	7.83E-09
Elastic Modulus (MPa)	205000
Poisson's Ratio	0.29
Thermal Conductivity (W·m·K ⁻¹)	42.5
Specific Heat (J·kg ⁻¹ ·K ⁻¹)	480
Thermal Expansion (K ⁻¹)	1.15E-05
Inelastic Heat Fraction	0.3336
Melt Temperature (K)	1803.15
ISV Model Coefficients	-
C01 (MPa)	5
C02 (K)	0
C03 (MPa)	690
C04 (K)	22
C05 (MPa ⁻¹)	0.3
C06 (K)	0
C07 (MPa ⁻¹)	0.3
C08 (K)	150
C09 (MPa)	4416
C10 (K)	2
C11 (s·MPa ⁻¹)	0
C12 (K)	0
C13 (MPa ⁻¹)	0.07
C14 (K)	121.5
C15 (MPa)	700
C16 (K)	0
C17 (s*MPa ⁻¹)	0
C18 (K)	0
C19	0.006
C20 (K ⁻¹)	1100
C21	0
Ca	-0.3
Cb	0
A _{void}	0
B _{void}	0
a	32000
b	10800
c	36000
η ₀ (#/mm ²)	200
KIC (MPa·mm ^{1/2})	2751
d (mm)	0.0035
f	0.00065
NND (mm)	0.16
d0 (mm)	0.002
CD2	1.5
GS0 (mm)	0.01
GS (mm)	0.01
ζ	1
Initial Porosity	0.00065
CTN (K)	300
CTC (K ⁻¹)	0.002
McClintock Growth, n	0.3
R0 (mm)	0.001
Cocks-Ashby Growth, m	20

Table B.2 ISV Model coefficients for varying hardness RHA steel alloys used in *Part III* of Chapter IV.

RHA Steel	Hardness (BHN)						
	250	300	350	400	450	500	550
Density (tonne/mm ³)	7.83E-09	7.83E-09	7.83E-09	7.83E-09	7.83E-09	7.83E-09	7.83E-09
Elastic Modulus (MPa)	205000	205000	205000	205000	205000	205000	205000
Poisson's Ratio	0.29	0.29	0.29	0.29	0.29	0.29	0.29
Conductivity (W·m·K ⁻¹)	42.5	42.5	42.5	42.5	42.5	42.5	42.5
Specific Heat (J·kg ⁻¹ ·K ⁻¹)	480	480	480	480	480	480	480
Thermal Expansion (K ⁻¹)	1.15E-05	1.15E-05	1.15E-05	1.15E-05	1.15E-05	1.15E-05	1.15E-05
Inelastic Heat Fraction	0.3336	0.3336	0.3336	0.3336	0.3336	0.3336	0.3336
Melt Temperature (K)	1803.15	1803.15	1803.15	1803.15	1803.15	1803.15	1803.15
C01 (MPa)	5	5	5	5	5	5	5
C02 (K)	0	0	0	0	0	0	0
C03 (MPa)	690	803	1003	1113	1203	1300	1400
C04 (K)	22	22	22	22	22	22	22
C05 (MPa ⁻¹)	0.3	0.3	0.3	0.3	0.3	0.3	0.3
C06 (K)	0	0	0	0	0	0	0
C07 (MPa ⁻¹)	0.3	0.3	0.3	0.3	0.3	0.3	0.3
C08 (K)	150	150	150	150	150	150	150
C09 (MPa)	4416	4416	4416	4416	4416	5216	6016
C10 (K)	2	2	2	2	2	2	2
C11 (s·MPa ⁻¹)	0	0	0	0	0	0	0
C12 (K)	0	0	0	0	0	0	0
C13 (MPa ⁻¹)	0.07	0.07	0.07	0.07	0.07	0.07	0.07
C14 (K)	121.5	121.5	121.5	121.5	121.5	121.5	121.5
C15 (MPa)	700	700	700	700	700	1000	1300
C16 (K)	0	0	0	0	0	0	0
C17 (s·MPa ⁻¹)	0	0	0	0	0	0	0
C18 (K)	0	0	0	0	0	0	0
C19	0.006	0.006	0.006	0.006	0.006	0.006	0.006
C20 (K ⁻¹)	1100	1100	1100	1100	1100	1100	1100
C21	0	0	0	0	0	0	0
Ca	-0.3	-0.3	-0.3	-0.3	-0.3	-0.3	-0.3
Cb	0	0	0	0	0	0	0
A _{void}	0	0	0	0	0	0	0
B _{void}	0	0	0	0	0	0	0
a	32000	32000	32000	32000	32000	32000	32000
b	10800	10800	10800	10800	10800	10800	10800
c	360	360	360	360	360	360	360
η ₀ (#/mm ²)	200	200	200	200	250	2000	4000
K _{IC} (MPa·mm ^{3/2})	2846	2800	2751	2625	2530	1802	1500
d (mm)	0.007	0.00525	0.0035	0.002625	0.0015	0.000035	0.0000035
f	0.00245	0.001378	0.00065	0.000517	0.000375	6.13e-07	1.23e-08
NND (mm)	0.08	0.08	0.08	0.08	0.08	0.08	0.08
d ₀ (mm)	0.002	0.002	0.002	0.002	0.002	0.002	0.002
CD2	1.5	1.5	1.5	1.5	1.5	1.5	1.5
GS0 (mm)	0.01	0.01	0.01	0.01	0.01	0.01	0.01
GS (mm)	0.015	0.0125	0.01	0.0075	0.005	0.0025	0.001
ζ	1.3	1.3	1.3	1.3	1.3	1.3	1.3
Initial Porosity	0.00065	0.00065	0.00065	0.00065	0.00065	0.00065	0.00065
CTN (K)	300	300	300	300	300	300	300
CTC (K ⁻¹)	0.002	0.002	0.002	0.002	0.002	0.002	0.002
McClintock Growth, n	0.3	0.3	0.3	0.3	0.3	0.3	0.3
R ₀ (mm)	0.001	0.001	0.001	0.001	0.001	0.001	0.001
Cocks-Ashby Growth, m	20	20	20	20	20	20	20